

December 2012

Investigation of the Quaternary Structure of an ABC Transporter in Living Cells Using Spectrally Resolved Resonance Energy Transfer

Deo R. Singh

University of Wisconsin-Milwaukee

Follow this and additional works at: <https://dc.uwm.edu/etd>

 Part of the [Biophysics Commons](#), and the [Physics Commons](#)

Recommended Citation

Singh, Deo R., "Investigation of the Quaternary Structure of an ABC Transporter in Living Cells Using Spectrally Resolved Resonance Energy Transfer" (2012). *Theses and Dissertations*. 67.
<https://dc.uwm.edu/etd/67>

This Dissertation is brought to you for free and open access by UWM Digital Commons. It has been accepted for inclusion in Theses and Dissertations by an authorized administrator of UWM Digital Commons. For more information, please contact open-access@uwm.edu.

**INVESTIGATION OF THE QUATERNARY
STRUCTURE OF AN ABC TRANSPORTER IN
LIVING CELLS USING SPECTRALLY
RESOLVED RESONANCE ENERGY TRANSFER**

by

Deo Raj Singh

A Dissertation Submitted in
Partial Fulfillment of the
Requirements for the Degree of

Doctor of Philosophy
in Physics

at

The University of Wisconsin-Milwaukee

December 2012

ABSTRACT

INVESTIGATION OF THE QUATERNARY STRUCTURE OF AN ABC TRANSPORTER IN LIVING CELLS USING SPECTRALLY RESOLVED RESONANCE ENERGY TRANSFER

by

Deo Raj Singh

The University of Wisconsin-Milwaukee, 2012
Under the Supervision of Professor Valerică Raicu

Förster resonance energy transfer (FRET) has become an important tool to study proteins inside living cells. It has been used to explore membrane protein folding and dynamics, determine stoichiometry and geometry of protein complexes, and measure the distance between two molecules. In this dissertation, we use a method based on FRET and optical micro-spectroscopy (OptiMiS) technology, developed in our lab, to probe the structure of dynamic (as opposed to static) protein complexes in living cells. We use this method to determine the association stoichiometry and quaternary structure of an ABC transporter in living cells. Specifically, the transporter we investigate originates from the pathogen *Pseudomonas aeruginosa*, which is a Gram-negative bacterium with several virulence factors, lipopolysaccharides being one of them. This pathogen coexpresses two unique forms of lipopolysaccharides on its surface, the A- and B-bands. The A-band polysaccharides, synthesized in the cytoplasm, are translocated into the periplasm

through an ATP-binding-cassette (ABC) transporter consisting of a transmembranar protein, Wzm, and a nucleotide-binding protein, Wzt. In *P. aeruginosa*, all of the biochemical studies of A-band LPS are concentrated on the stages of the synthesis and ligation of polysaccharides (PSs), leaving the export stage involving ABC transporter unexplored. The mode of PS export through ABC transporters is still unknown. This difficulty is due to the lack of information about sub-unit composition and structure of this bi-component ABC transporter.

Using the FRET-OptiMiS combination method developed by our lab, we found that Wzt forms a rhombus-shaped homo-tetramer which becomes a square upon co-expression with Wzm, and that Wzm forms a square-shaped homo-tetramer both in the presence and absence of Wzt. Based on these results, we propose a structural model for the double-tetramer complex formed by the bi-component ABC transporter in living cells. An understanding of the structure and behavior of this ABC transporter will help develop antibiotics targeting the biosynthesis of the A-band LPS endotoxin.

© Copyright by Deo Raj Singh, 2012

All Rights Reserved

Dedicated, with sincerity,
to my teachers.

Table of contents

<i>Abstract</i>	<i>ii</i>
<i>List of figures</i>	<i>ix</i>
<i>Acknowledgements</i>	<i>xi</i>
<i>Overview</i>	<i>I</i>
<i>Chapter 1. Introduction</i>	<i>7</i>
1.1 Fluorescence	8
1.2 Green fluorescent proteins (GFPs).....	11
1.3 Fluorescence resonance energy transfer	13
1.3.1 Dependence on distance	14
1.3.2 Orientation dependence	16
1.3.3 FRET – An excellent tool to study protein-protein interaction.....	18
1.3.4 Förster radius for different FRET pairs	21
1.4 Challenges in FRET measurements	22
1.5 Techniques of FRET imaging.....	25
1.5.1 Sensitized emission.....	25
1.5.2 Acceptor photo-bleaching.....	26
1.5.3 Fluorescence lifetime imaging microscopy	28
1.5.4 Spectral imaging	30
1.5.5 Polarization anisotropy imaging	30
1.6 Application of FRET in biology	32
1.6.1 Detection of heteromerization of more than two proteins	33
1.6.2 Tracking SNARE complex formation in live endocrine cells	34
1.6.3 Probing calcium ion concentration changes in living cells.....	35
1.6.4 Measuring energetics of membrane protein dimerization.....	36
1.6.5 Stoichiometry determination of protein complexes	37
1.7 Other applications of FRET in biology.....	38
<i>Chapter 2. Förster rate of energy transfer</i>	<i>44</i>
2.1 Historical background of resonance energy transfer.....	44
2.2 Review of physical quantities needed for Förster’s theory	48
2.2.1 Absorption and emission of radiation	48
2.2.2 Einstein’s A and B coefficients	51
2.2.3 Dipole moment	53
2.2.4 Born-Oppenheimer approximation	53
2.2.5 Transition dipole moment.....	54
2.2.6 Frank-Condon principle.....	54
2.2.7 Relation between the Einstein coefficients and the transition dipole moment.....	57

2.2.8	Fluorescence emission spectrum of the molecules	58
2.2.9	Beer-Lambert law and the extinction coefficient	59
2.2.10	Absorption spectrum of molecules	60
2.3	Classical derivation of energy transfer rate	61
2.3.1	Perrin's theory of energy transfer rate	61
2.3.2	Förster's correction in Perrin's theory of energy transfer rate	64
2.4	Quantum mechanical treatment of excitation transfer	67
2.4.1	Strong coupling	69
2.4.2	Weak coupling	70
2.4.3	Very weak coupling	71
2.5	Quantum mechanical derivation of Förster energy transfer rate	73
2.6	Determination of stoichiometry and quaternary structure of interacting molecules using spectral FRET	76
2.6.1	Elementary theory of fluorescence resonance energy transfer	76
2.6.2	Determination of FRET efficiency in terms of intensity-based measurable parameters	80
2.6.3	Prediction of E_{app} values for different oligomer geometries	82
<i>Chapter 3. Pixel versus average FRET: Numerical simulations</i>		<i>88</i>
3.1	Theoretical background	92
3.2	Methods	96
3.3	Results and discussion	99
3.4	Conclusion	109
<i>Chapter 4. Linear and non-linear optical microscopy</i>		<i>114</i>
4.1	One-photon vs. two-photon absorption	116
4.2	Laser scanning confocal microscope	120
4.3	Spectrally resolved two-photon microscope	123
4.4	Image Reconstruction	127
4.5	Spectral calibration of the microscope	130
4.6	Multicolor imaging	131
4.6.1	FRET basics	131
4.6.2	Spectral deconvolution	133
<i>Chapter 5. Biological system of interest</i>		<i>137</i>
5.1	<i>Pseudomonas aeruginosa</i>	137
5.2	ATP-binding cassette (ABC) transporters	141
<i>Chapter 6. Quaternary structure of the Wzm-Wzt ABC transporter</i>		<i>146</i>
6.1	Experimental procedure	148
6.1.1	Gene cloning and plasmid constructs	148

6.1.2	Expression of fluorescently-tagged Wzm and Wzt in mammalian cells.....	150
6.1.3	Optical micro-spectroscopy	150
6.1.4	Selection of FRET pairs.....	151
6.1.5	Emission spectra	152
6.1.6	Image analysis and FRET efficiency determination	153
6.1.7	Distributions of FRET efficiencies	153
6.1.8	Estimation of the protein expression level.....	154
6.1.9	Analysis of E_{app} histograms	155
6.2.1	Cytoplasmic Wzt and membrane-bound Wzm interact at the plasma membrane.....	157
6.2.2	The quaternary structure of Wzt in the absence of Wzm	160
6.2.3	The quaternary structure of Wzt in the presence of untagged Wzm	162
6.2.4	The quaternary structure of Wzm in the absence or in the presence of untagged Wzt	164
6.2.5	Confirmation of the quaternary structure from analysis of cells presenting broad E_{app} distributions	166
6.2.6	Reliability of the pixel-level FRET method.....	168
6.2.7	Order-of-magnitude estimate of the two hetero-tetramers concentration	170
6.3	Discussion	171
6.3.1	Why the individual histogram peaks are broader than those of meta-histograms.....	171
6.3.2	Proposed structural model for the ABC transporter.....	172
6.3.3	Considerations regarding the stability of the complexes	173
6.3.4	Comparison of the present results to other studies	174
6.3.5	Significance of the present results	175
	<i>Chapter 7. Conclusion and directions for future research</i>	<i>179</i>
	<i>Curriculum vitae</i>	<i>182</i>

List of figures

<i>Figure 1.1: Energy diagram of a fluorophore undergoing fluorescence and phosphorescence</i>	<i>10</i>
<i>Figure 1.2: Energy diagram depicting Förster Resonance Energy Transfer (FRET) between a donor (D) and acceptor (A) molecule.....</i>	<i>14</i>
<i>Figure 1.3: Relative orientation of a donor and an acceptor dipoles</i>	<i>17</i>
<i>Figure 1.4: Visual illustration of FRET between a donor and an acceptor</i>	<i>20</i>
<i>Figure 1.5: Illustration of FRET as a magnifying glass.....</i>	<i>21</i>
<i>Figure 1.6: Excitation and emission spectrum of SCFP3A (donor) and SYFP2 (acceptors).</i>	<i>24</i>
<i>Figure 1.7: Illustration of effect of polarized excitation and rotational diffusion on the fluorescence</i>	<i>32</i>
<i>Figure 1.8: Distributions of FRET efficiencies in CHO cells expressing the rat M1 muscarinic receptor and the Premo Cameleon FRET Biosensor.....</i>	<i>36</i>
<i>Figure 2.1: Energy level diagram of a two-state system illustrating absorption</i>	<i>49</i>
<i>Figure 2.2: Energy level diagram of a two-state system illustrating spontaneous emission.....</i>	<i>50</i>
<i>Figure 2.3: Energy level diagram of a two-state system illustrating stimulated emission</i>	<i>51</i>
<i>Figure 2.4: Transition of an electron from electronic ground state to electronic excited state</i>	<i>56</i>
<i>Figure 2.5: Illustration of absorption of light by a slab of solution of fluorescent molecules of thickness d</i>	<i>59</i>
<i>Figure 2.6: The emission spectrum of the donor (solid line) and the absorption spectrum of the acceptor (dashed line)</i>	<i>65</i>
<i>Figure 2.7: The emission spectrum of the donor and the absorption spectrum of the acceptor are shown as the rectangle of width Ω.....</i>	<i>66</i>
<i>Figure 2.8: Configuration of a circular octamer representing seven donors (turquoise color) and one acceptor (yellow)</i>	<i>83</i>
<i>Figure 2.9: The apparent FRET efficiency expressions for different configurations of an octamer.</i>	<i>85</i>
<i>Figure 3.1: Different stages in the generation of a fractal distribution of molecules embedded in an Euclidian square.....</i>	<i>98</i>
<i>Figure 3.2: Histograms showing the distribution of FRET efficiencies for donors and acceptors randomly scattered on lattices of the type shown in Fig. 3.1</i>	<i>101</i>
<i>Figure 3.3: Dependence of the average FRET efficiency for distributions of monomeric donors and acceptors on (A) the ratio of acceptor to donor concentrations, $[A]/[D]$ (for $[A]+[D]=$ constant), and (B) the concentration of acceptors, $[A]$ (for $[A]/[D] =$ constant), for Euclidian and fractal distributions of molecules</i>	<i>102</i>
<i>Figure 3.4: Histograms showing the distribution of FRET efficiencies for dimers distributed at random on lattices of the type shown in Fig. 3.1</i>	<i>104</i>
<i>Figure 3.5: Dependence of the average FRET efficiency for distributions of dimers on the concentration of acceptors, $[A]$ (for $[A]/[D]=1$), for Euclidian and fractal surfaces.....</i>	<i>105</i>

<i>Figure 3.6: Histograms showing the distribution of FRET efficiencies for mixtures of dimers, donors, and acceptors distributed at random on lattices of the type shown in Fig. 3.1</i>	107
<i>Figure 3.7: Dependence of the average FRET efficiency for distributions of dimers on the ratio of total acceptor to total donor concentrations, $[A]/[D]$ (for $[A]+[D]=\text{constant}$) for the three molecular distributions shown in Fig. 3.1</i>	108
<i>Figure 4.1: Energy level diagrams for one- photon absorption (OPA) and two- photon absorption (TPA)</i>	118
<i>Figure 4.2: Schematic representation of laser scanning confocal microscope</i>	121
<i>Figure 4.3: Schematic of spectrally resolved two-photon microscope</i>	125
<i>Figure 4.4: Images corresponding to different y positions within the sample</i>	128
<i>Figure 4.5: Illustration of the image reconstruction procedure corresponding to the wavelength</i>	129
<i>Figure 5.1: Outline of the Gram-negative bacterium</i>	138
<i>Figure 5.2: Cell membrane of the Gram-negative bacterium</i>	139
<i>Figure 5.3: Cartoon depicting the bio-synthesis of A-band PS</i>	141
<i>Figure 5.4: Schematic of an ABC transporter</i>	143
<i>Figure 6.1: Localization of Wzm and Wzt proteins in optical sections of Chinese hamster ovary (CHO) cells as detected by a two-photon microscope with spectral resolution</i>	159
<i>Figure 6.2: Mapping the spatial distribution of complexes of Wzm and Wzt proteins in thin ($3\mu\text{m}$) optical sections through a CHO cell</i>	160
<i>Figure 6.3: Homo-oligomerization of Wzt expressed in CHO cells in the absence of Wzm</i>	162
<i>Figure 6.4: Homo-oligomerization of Wzt expressed in CHO cells in the presence of untagged Wzm</i>	163
<i>Figure 6.5: Homo-oligomerization of Wzm expressed in CHO cells in the absence of Wzt</i>	165
<i>Figure 6.6: Homo-oligomerization of Wzm expressed in CHO cells in the presence of untagged Wzt</i>	166
<i>Figure 6.7: Determination of the quaternary structure of Wzt and Wzm expressed in CHO cells showing multiple peaks in their E_{app} histograms</i>	168
<i>Figure 6.8: Meta-histogram obtained from peak positions of individual E_{app} histograms for CHO cells expressing an artificial tetramer</i>	170
<i>Figure 6.9: Two versions of the hetero-octameric model proposed for the quaternary structure of the Wzm-Wzt ABC transporter</i>	173

Acknowledgements

First and foremost, I wish to thank my major advisor, Professor Valerică Raicu -- notably for his encouragement, patience and involvement in my work, all of which have played a direct role in helping me become the experimentalist I am today. I joined his research group in the summer of 2008, primarily because of the particular research he was involved in, and because of what I had heard about him personally; in either regard, I have not been disappointed. The first project he assigned to me dealt with numerical simulations. As I started getting results, he persuaded me to also learn experimental techniques in biophysics. Having little background in experimental biophysics, I started doing experiments to address important problems of protein-protein interaction under his supervision. Prof. Raicu always showed confidence in me and taught me to tackle complex problems by starting with the simple ones that I understand, then building up, step by step, to form a firm foundation.

Professor Julie A. Oliver (Department of Biological Sciences at the University of Wisconsin-Milwaukee), taught me the experimental techniques required for cell culture and gene expression in mammalian cells, which I needed to study protein-protein interaction. I would like to thank her for her time and patience to teach me these techniques. Additionally, I thank Julie and her lab assistant, Linda Westrick, for advising me on cell culture and gene expression and for letting me use her tissue culture facility.

I am thankful to all members of the Raicu research group, current and former, particularly Dr. Michel R. Stoneman, who helped me troubleshoot the codes for data analysis, mode-locking the laser, and aligning the laser for two-photon microscopy; Ashish Mishra for helping me in data collection and data analysis; Suparna Patowary for giving me data for artificial tetramers; and Praveen Ghosh for helping me in data analysis. I also wish to thank Joan Baumgart, the Business Specialist in our group, who was most helpful in efficiently placing orders for the materials required for the experiments.

I want to thank our collaborators, Prof. Liviu Movilianu and Dr. Mohammad M. Mohammad (both from Syracuse University) for providing us with plasmids for our experiments and for discussions related to my PhD project.

The faculty members in Physics department at UW-Milwaukee with whom I took courses also deserve much credit. The concepts I learned in these courses were very useful in my research and were thought provoking and enjoyable and contributed to my academic development.

Of course, the members of my defense committee (Professor Raicu, along with Professor Dilano Saldin, Professor Prasenjit Guptasarma, Professor Julie Oliver and Professor Marius Schmidt) deserve special recognition. They made many suggestions that added value to this dissertation and were very cooperative during my defense.

I appreciate the help and cooperativeness of the following staff members in the UW-Milwaukee Physics department: Steve Kennedy, Reba Sinha, Pamela Urban and Greg Baran. Further, in particular, Kate Valerius, Graduate Program Assistant, was quite helpful both in offering her time and expertise in reviewing and proofing this dissertation, and for all that was required as it related to the administrative tasks associated with the various steps in my time here.

My fellow graduate students at UW-Milwaukee were all helpful, in their own ways, as well, and I enjoyed their camaraderie. As a graduate student, my research was funded by the National Science Foundation (NSF). I want to thank the NSF for funding my research. I also want to thank the UW-Milwaukee Graduate School for further financial support in their selection of me as a Graduate School Fellow (in my 4th year) and as a Dissertator Fellow (in my 5th year).

Finally, I want to thank my parents and my family, who were instrumental in providing me with a very strong educational background, and who always supported me and believed in my abilities and encouraged me to push my boundaries. My wife, Sweta Singh, deserves special credit for being very supportive during my graduate study and making many figures included in this dissertation.

Overview

In 1946, T. Förster (1) gave the correct quantum mechanical explanation of energy transfer between an optically excited molecule (donor) and an unexcited one (acceptor) in a solution. His breakthrough discovery was based on the earlier works of J. and F. Perrin (2, 3), who unfortunately failed to predict the correct dependence of the transfer efficiency on the distance between the two molecules. Förster was originally motivated by the lack of understanding of the mechanism through which energy is transferred in photosynthesis, a process through which plants and other organisms convert light energy into chemical energy to accomplish biological activities. One known fact was that the number of photons that strike the surface of plant leaves is much larger than the number of reaction centers in the leaf where the photosynthetic electron transfer reactions take place. A reaction center is a complex formed by many proteins, and light-absorbing pigments to execute the primary energy conversion reactions of photosynthesis. It was long thought that the energy of photons randomly diffused on the whole surface area of leaves, which is large compared to the reaction centers. This diffused energy is captured by the reaction centers. However, the exact mechanism of energy transfer in photosynthesis was not understood until the theory of energy transfer due to Förster was developed. In leaves, light harvesting complexes surround the reaction centers. When the photons are absorbed by these complexes, the electron goes into an excited state and energy is transferred non-radiatively to the molecule present in reaction center through dipole-dipole coupling. The theory Förster developed – known as *Förster Resonance*

Energy Transfer – in terms of parameters that can be derived experimentally, quantitatively explained the energy transfer phenomenon including photosynthesis.

Förster resonance energy transfer (FRET) was subsequently used in research in biophysics and in biochemistry to determine the distances and conformational changes, and it has now become an important tool in biological research. When used in conjunction with fluorescent tags attached to macromolecules of interest, FRET effectively increases the resolution of optical microscopes from $\sim 0.3\mu\text{m}$ to less than 5 nm. In this way, FRET enables one to visualize the interactions within a nanometer range which makes it an excellent tool to study molecular interaction in living cells.

In this dissertation, I describe my research on an important problem of protein-protein interactions in living cells, using experimental measurements based on FRET imaging, as well as numerical simulations and theoretical modeling of the experimental results. The dissertation is divided into seven chapters, each of which is briefly summarized below.

Chapter 1 begins with introduction of the physical processes of fluorescence and fluorescence resonance energy transfer (FRET). Then, the dependence of FRET on distance between two fluorescent molecules, also called fluorophores, and on the orientation of the dipoles associated with two fluorophores is discussed. Further, the naturally occurring fluorescent proteins and their variants that are used to tag the protein

of interest to study many biological processes in living cells are discussed briefly. Different combinations of these proteins are used as FRET pairs in FRET microscopy. Moreover, the challenges in FRET microscopy and different techniques for measuring FRET are discussed. In addition, an overview of the literature on the applications of FRET to biophysical and biological studies is presented.

In chapter 2, a historical overview of energy transfer between the two dipoles is presented. The classical derivation of energy transfer due to Perrin is given. The modifications by Förster of Perrin's theories that led him to predict the correct rate of energy transfer is discussed, which is also known as the classical derivation of Förster theory of energy transfer. Then, the quantum mechanical description of excitation transfer between two molecules due to Förster is presented. Moreover, the expressions for apparent FRET efficiency in terms of measurable fluorescence intensities are derived. For an oligomeric complex of size larger than two, different configurations of the complexes are expected to have different FRET efficiencies depending upon the number of donors and acceptors and their positions within the complex. For oligomers having simple geometries such as linear and triangular trimers, linear tetramer, rhombus, square tetramer, and circular octamer, the expressions for apparent FRET efficiencies for different configurations are presented in terms of the pairwise FRET efficiency, i.e., FRET efficiency between a donor and an acceptor. In chapter 6, these models are used to determine the stoichiometry and quaternary structures of a bacterial ABC transporter in living cells.

In chapter 3, the results of numerical simulations, obtained when the molecules are distributed on two dimensional homogeneous and inhomogeneous lattices, are presented. The distribution of FRET efficiencies obtained for molecules distributed on homogeneous and inhomogeneous surfaces are compared with average FRET efficiencies. Three situations are considered: (i) when free donors and acceptors are randomly distributed on the surfaces. (ii) only dimers are distributed on the surfaces randomly, and (iii) the dimers are distributed with free donors and acceptors randomly. The contributions of random molecular collisions to FRET (known as stochastic FRET) are discussed. The advantage of distribution of FRET over average FRET is described.

Chapter 4 starts with the introduction of one-photon excitation and two-photon excitation process. Then, the schematic and working principle of laser scanning confocal microscopy is presented. Next, the schematic and the working principle of a spectrally resolved two-photon microscopy are described. Since this microscope is a spectrally resolved two-photon scanning microscope, corresponding to one line scan one gets one image in wavelength and direction of scan plane. The reconstruction of spectral images from the images corresponding to each line scan is described in this chapter. In FRET microscopy, two fluorophores are used; therefore, each pixel of an image consists of donor fluorescence and acceptor fluorescence. The concept of spectral unmixing to get the donor fluorescence in the presence of acceptors and acceptor fluorescence in the

presence of donors is given. Since direct excitation may cause acceptor bleed-through (ABT), some FRET pairs are where ABT is almost negligible.

In chapter 5, a brief overview of the structure of the biological system of our interest, the Gram-negative bacterium *Pseudomonas aeruginosa*, is given. This bacterium is an opportunistic pathogen with several virulence factors, lipopolysaccharides (LPSs) being one of them. LPSs are the main components of the outer leaflet of the outer membrane of this pathogen. In addition, the general architecture and the mechanism underlying the transport of substance through an ABC transporter is presented. The transmembrane protein Wzm and the cytoplasmic protein Wzt together form an ABC transporter in this bacterium and translocate the polysaccharides, synthesized in the cytoplasm, across the inner membrane.

In chapter 6 a new FRET-based method, which we developed (that allows one to probe the stoichiometry and structure of dynamic protein complexes in living cells), is described. This method is used to determine the quaternary structure of the transmembrane subunit Wzm and the cytoplasmic nucleotide binding domain (NBD) subunit Wzt of an ABC transporter, Wzm-Wzt, found in *Pseudomonas aeruginosa*. The Wzm-Wzt transporter plays an important role in the synthesis of LPS, an endotoxin. The localization of Wzm and Wzt in the living cells is also presented. In addition, the interaction between the Wzm and Wzt subunits is determined. Based on these results, the structural model for this ABC transporter is proposed.

Finally, conclusions and future studies are discussed in chapter 7.

References

1. Förster, T. (1946) Energiewanderung und fluoreszenz. *Naturwissenschaften* **6**:166-175.
2. Perrin, J. (1927) Fluorescence et induction moleculaire par resonance. *C. R. Hebd. Seances Acad. Sci.* **184**:1097-1100.
3. Perrin, F. (1933) Interaction enter atomes normal et activite. Transferts d'activation. Formation d'une molecule activee. *Ann. Institut Poincare* **3**:279-318.

Chapter 1. Introduction

Many cellular processes are based on dynamic interactions between proteins. Although these interactions are commonly studied *in vitro* using biochemical methods, the weak and transient interactions in proteins that occur in the natural milieu of the cell can't be studied *in vitro* by biochemical methods. Co-localization by immunofluorescence microscopy is historically the popular method to study protein-protein interaction *in situ*. Since the proteins are a few nanometers wide and the resolution of the fluorescence microscopy is a few hundred nanometers, such a crude measurement may be misleading (1). The knowledge that two molecules are adjacent, and not just in the same neighborhood, provides much more reliable information about the interaction. One could, of course, obtain information about protein quaternary structure with electron microscopes, but its application is currently limited to non-living objects.

In contrast, microscopy based on FRET measurements overcomes all these limitations. Since FRET occurs between the fluorophores separated by less than 10 nm, it is well suited to study protein-protein interaction. In this chapter, we give the overview of fluorescence and fluorescence resonance energy transfer (FRET). In addition, we describe the dependence of FRET on distance between two fluorescent molecules, also called fluorophores, and on the orientation of the dipoles associated with two fluorophores. Next, we discuss about the fluorescent proteins and their variants that are used to tag the protein of interest to study many biological processes in living cells using

FRET. Moreover, we discuss many challenges in FRET microscopy and different techniques for FRET measurements. Finally, we give an overview of the literature on the applications of FRET to biophysical and biological studies.

1.1 Fluorescence

When the incident photon falls on the fluorophore, the electron jumps to an excited singlet state, S_1 , from the singlet ground state, S_0 . The electron loses its energy partially through vibrational relaxation, which takes place within $\sim 10^{-12}$ s. This process brings the electron to the lowest level in S_1 . The electron then jumps to the ground state, S_0 , of the fluorophore either emitting a red-shifted photon, with a rate constant, Γ^r , where superscript r stands for radiative, or without emitting a photon, with a rate constant, Γ^{nr} , where superscript nr stands for non-radiative. The light emitted due to the quantum transition from S_1 to S_0 is called *fluorescence*. The process is illustrated as shown in Fig. 1.1. The emission rates of fluorescence are of the order of 10^8 sec^{-1} , hence the fluorescence lifetimes are typically of the order of 10 ns. Since fluorescence lifetimes are much longer than that of vibrational relaxation, emission occurs after the completion of vibrational relaxation. The average lifetime of the fluorophore is different from the fluorescence lifetime. The average lifetime of the fluorophore is the time between its excitation and return to the ground state. In contrast to fluorescence lifetime, which only depends on the radiative de-excitation rate of the fluorophore from singlet excited state to the singlet ground state, the average lifetime of the fluorophore depends on both radiative and non-radiative de-excitation rates. Since the fluorescence lifetime of the fluorophore

is very short, measurements of time-resolved emission requires sophisticated optics and electronics. During such transitions, the electronic spin remains conserved.

Another process closely related to fluorescence is phosphorescence. Both fluorescence and phosphorescence are forms of luminescence. The fluorophore in the state S_1 can undergo spin conversion to reach the first triplet state T_1 through intersystem crossing. The emission from triplet state T_1 to singlet ground state S_0 is called *phosphorescence*. The phosphorescence is generally Stokes red-shifted relative to the fluorescence. In excited triplet states, the electron in excited state has the same spin orientation as the electron in the ground state. On the other hand, in excited singlet state the electron in the excited orbital is paired with second electron having opposite spin. In phosphorescence, transition from excited state to ground state is forbidden and the emission rates are slow (10^3 to 10^0 sec^{-1}) (2). Hence, the phosphorescence life-times are typically from milliseconds to seconds. Usually, phosphorescence is not observed in solutions because of the existence of many de-excitation pathways such as non-radiative decay and quenching processes that compete with emission. The distinction between fluorescence and phosphorescence is not always clear. There are materials that contain a metal and organic ligands, called transition metal-ligand complexes (MLCs), show mixed singlet-triplet states with their intermediate lifetimes from a few hundreds of nanoseconds to several microseconds.

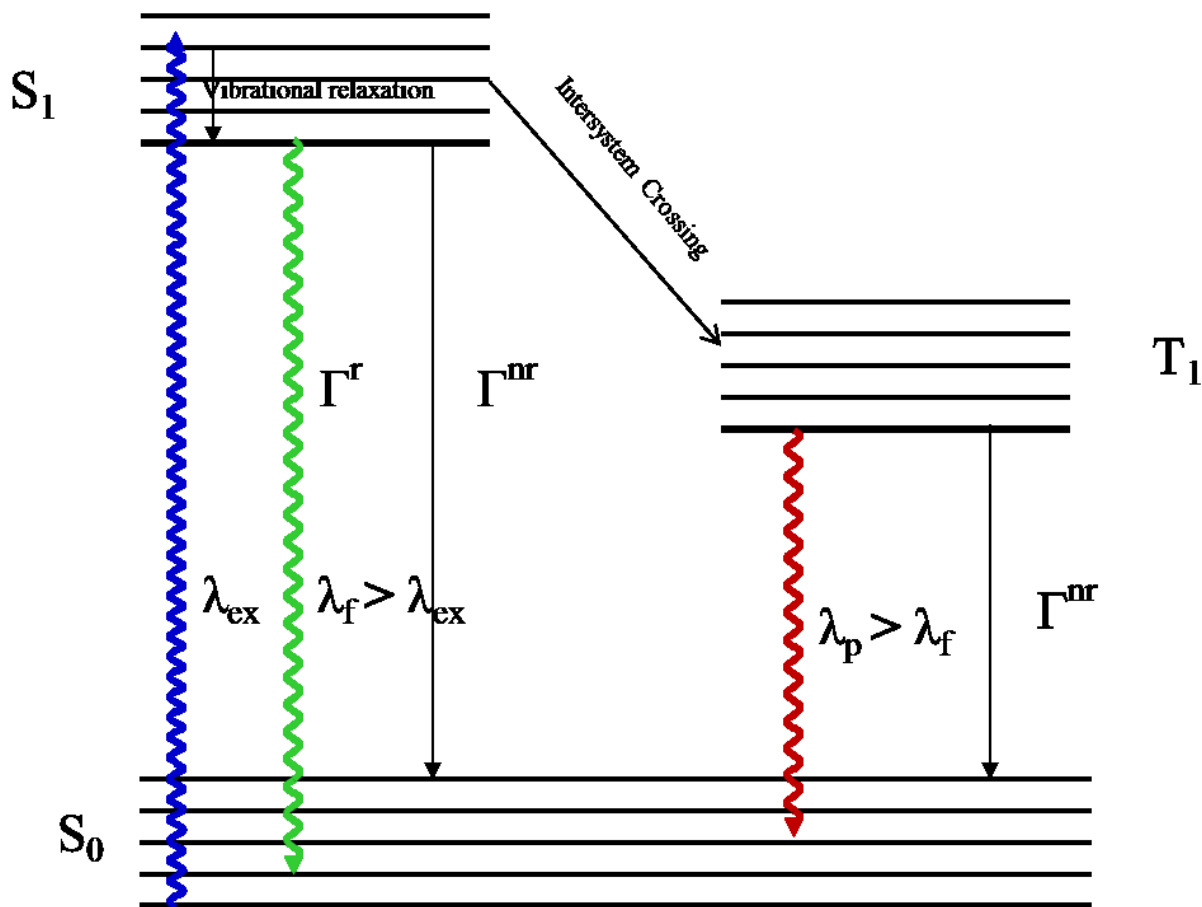


Figure 1.1: Energy diagram of a fluorophore undergoing fluorescence and phosphorescence. S_0 and S_1 represent the singlet ground state and the singlet excited state of the molecule, while T_1 is the excited triplet state. λ_{ex} is the wavelength of the light absorbed by the fluorescent molecule, λ_f is the wavelength of fluorescence of the molecule, Γ^r is the radiative energy transfer rate from S_1 to S_0 , and Γ^{nr} is non-radiative energy transfer rate from S_1 to S_0 . The excitations get transferred to the triplet state T_1 through intersystem crossing. The phosphorescence wavelength is λ_p . The radiative transitions are depicted by wavy lines, while non-radiative transitions are depicted by straight lines.

Recent years have seen a dramatic growth in cellular and molecular imaging (studies, technologies, etc.) using fluorescence. It can be used to localize the molecules in the cell, study conformational changes in macromolecules and study interaction between molecules. Typically, the molecules that are used as fluorescent markers in live

cell imaging are naturally occurring green fluorescent proteins (GFPs), or its variants, and are described below.

1.2 Green fluorescent proteins (GFPs)

The first light-producing protein was purified and characterized by Shimomura et al. (3) from a green-bioluminescing coelenterate, aequorin, from the jellyfish *Aequorea victoria*. However, they found that the aequorin, when activated, generated blue rather than green light. The green light was produced in *Aequorea victoria* by the excitation of another inherent fluorescent protein (3, 4). This protein, which was initially described as green protein, is now called *green fluorescent protein* (GFP). The unusual chemistry of GFP required one or two enzymes for chromophore formation. However, the fluorescent GFP can be made in many cell types and cellular compartments without enzymes. Since GFP does not require additional gene from *Aequorea victoria*, the chromophore formation is not species-specific (5). The chromophore formation occurs either by autocatalysis or through the use of ubiquitous cellular components (5). The first heterologous expression of GFP was in *E. coli* and in the nematode *C. elegans* (5, 6). The spectral properties of GFP were same in the *E. coli* as in the purified protein from *Aequorea victoria*. The initial experiments demonstrated that GFP can be used as a noninvasive way to monitor gene expression *in vivo*.

In principle, green fluorescent proteins can also be fused to the protein of interest to study its localization and targeting. The first fusion protein was obtained with the

expression of gene *exuperantia* (*exu*) tagged with a GFP gene at the N or C terminus. This gene is needed for the localization of mRNA in the developing oocyte of *Drosophila* (7). The GFP tag did not affect the function of EXU protein. Both parts of the protein functioned as separate domain. The fusion protein GFP-EXU was localized within developing oocyte as it could have been localized without GFP tag. The results obtained from protein tagging with GFP were better than that obtained from the previous analysis of EXU distribution based on immunocytochemistry. The advantage of GFP tag over antibodies is specificity, cross-reactivity does not occur with GFP (6). Additionally, the movement of protein-tagged with GFP in living cells can be monitored.

Since GFP can be expressed in *E. coli*, several investigators modified the properties of this fluorescent protein (6). Many mutations of this fluorescent protein with altered excitation and emission spectra and fluorescent intensity have been discovered. These mutated fluorescent proteins are aimed at providing better fluorescent markers, to allow energy transfer experiments with multicolor tagging and to understand the molecular basis of fluorescence. Many variants of GFP such as green fluorescent protein 2 (GFP₂), yellow fluorescent protein (YFP), cyan fluorescent protein (CFP), Venus etc., are available and are used in combination in FRET studies. GFP₂-YFP, GFP-YFP, CFP-YFP are a few examples of FRET pairs.

1.3 Fluorescence resonance energy transfer

Förster resonance energy transfer (FRET) is a process through which energy from an excited donor molecule (D) is transferred to a nearby unexcited acceptor molecule (A) non-radiatively through dipole-dipole coupling (2, 8, 9). The process of energy transfer is depicted in Fig. 1.2. The acceptor molecule (A) gets excited through this process. If the acceptor molecule is also a fluorescent molecule, it will emit photon of wavelength that is further red-shifted from the donor emission wavelength. In this case, FRET is also called Fluorescence Resonance Energy Transfer.

The application of FRET microscopy as a tool to study assembly and stoichiometry of biological complexes, conformational changes and protein-protein interaction, has seen rapid growth in recent years. The development of different fluorescent markers with different fluorescent properties in conjunction with FRET microscopy has opened the door to explore the biological reactions inside living cells which were previously only possible through biochemical means. The parameters that affect the energy transfer rate from the excited donor to an unexcited acceptor are described below.

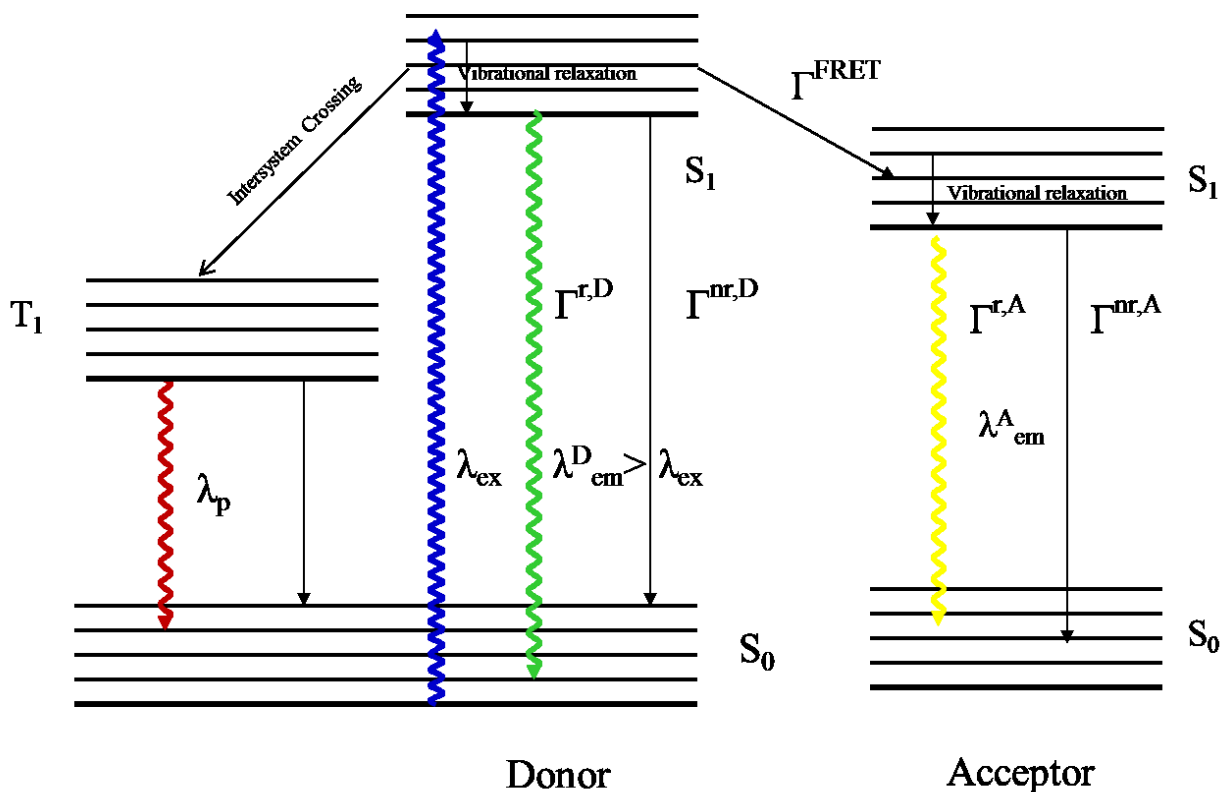


Figure 1.2: Energy diagram depicting Förster Resonance Energy Transfer (FRET) between a donor (D) and acceptor (A) molecule. S_0 and S_1 represent the singlet ground state and the singlet excited state of the donor and acceptor molecules, respectively. T_1 represents the triplet state of the donor molecule. The excited donor can reach to the triplet state through intersystem crossing. λ_{ex} is the wavelength of the light absorbed by the donor molecule, λ_{em} is the wavelength of fluorescent emitted light by the molecule, Γ^r is the radiative energy transfer rate from S_1 to S_0 , Γ^{nr} is non-radiative energy transfer rate from S_1 to S_0 and Γ^{FRET} is the rate of Förster resonance energy transfer from excited donor to unexcited acceptor. The radiative transitions are depicted by wavy lines, while non-radiative transitions are depicted by straight lines. This figure is adapted from (10).

1.3.1 Dependence on distance

Here, we will present the qualitative description of the rate of energy transfer rate and its dependence on distance. The detailed quantum mechanical derivation of energy transfer rate is presented in the next chapter. The rate of energy transfer from an excited donor (D) to unexcited acceptor (A) is given by (2, 8, 11) (also, see chapter 2):

$$\Gamma_{D \rightarrow A} = \frac{1}{\tau_D} \left(\frac{R_0}{R} \right)^6 \quad (1.1)$$

where R is the distance between the donor and an acceptor and R_0 is the Förster radius. It is defined as the distance R when the rate of energy transfer between the donor and an acceptor is equal to the decay rate of excited donor in the absence of the acceptor. τ_D is called the lifetime of donor in the absence of the acceptor. The inverse of τ_D is the rate of deactivation of the donor from excited state to the ground state that includes all the de-excitation pathways other than energy transfer (radiative transfer rate $\Gamma^{r,D}$ and non-radiative transfer rate $\Gamma^{nr,D}$ which includes internal conversion rates, intersystem crossing rates) (Fig. 1.2). FRET opens an additional de-excitation pathway for the excited donor and competes with all other de-excitation pathways kinetically. τ_D is not, in general, the same as the intrinsic lifetime τ_f of the donor. τ_f is the inverse of the radiative de-excitation rate of an excited donor and can be calculated from Einstein's A coefficient. The expression for R_0 in terms of experimentally measurable parameters for a donor and an acceptor pair is derived in chapter 2 and is given by:

$$R_0^6 = \frac{9000 \kappa^2 Q^D (\ln 10) c^4}{128 \pi^5 \mu^4 N_A} \int f_D(\nu) \epsilon_A(\nu) \frac{d\nu}{\nu^4} \quad (1.2)$$

where, ν is the frequency (in sec^{-1} units), Q^D is the quantum yield of the donor that is defined as the number of photons emitted by the donor over the number of photons absorbed by it (see chapter 2 for detail), N_A is the Avogadro's number, μ is the refractive index pertaining to energy transfer, $f_D(\nu)$ is the normalized measured fluorescent spectrum of the donor, $\epsilon_A(\nu)$ is the molar absorption spectrum of the acceptor (in the units of $\text{cm}^{-1} \text{mole}^{-1}$) and κ is related to orientations of dipoles in space. The expression (1.2) can also be written as (8):

$$R_0^6 = 8.79 \times 10^{-25} \mu^{-4} Q_D \kappa^2 J(\nu) \text{ cm}^6. \quad (1.3)$$

The quantity $J(\nu)$ in above expression is called *overlap integral* and represents the integral in (1.2)

1.3.2 Orientation dependence

As it is clear from (1.2) and (1.3), the Förster distance R_0 depends on the orientation factor of interacting dipoles, κ^2 . Since, the rate of energy transfer depends on R_0 the orientation factor also affects the rate of energy transfer. The electric field due to the donor dipole at an acceptor dipole is given by:

$$\vec{E}_D = \frac{|m_D|}{R^3} \{2 \cos \theta_D \hat{R} + \sin \theta_D \hat{\theta}_D\} \quad (1.4)$$

where, the meanings of symbols are explained in Fig. 1.3.

The rate of energy transfer in (1.1) is proportional to the square of interaction energy between the donor and acceptor dipoles,

$$\Gamma_{D \rightarrow A} \propto (U_{D \rightarrow A})^2 = (\vec{E}_D \cdot \vec{m}_A)^2, \quad (1.5)$$

or

$$\Gamma_{D \rightarrow A} \propto \frac{|m_D|^2 |m_A|^2}{R^6} \{2 \cos \theta_D \hat{R} \cdot \vec{m}_A + \sin \theta_D \hat{\theta}_D \cdot \vec{m}_A\}^2 = \frac{|m_D|^2 |m_A|^2}{R^6} \kappa^2, \quad (1.6)$$

where

$$\kappa^2 = \{2 \cos \theta_D \hat{R} \cdot \hat{m}_A + \sin \theta_D \hat{\theta}_D \cdot \hat{m}_A\}^2. \quad (1.7)$$

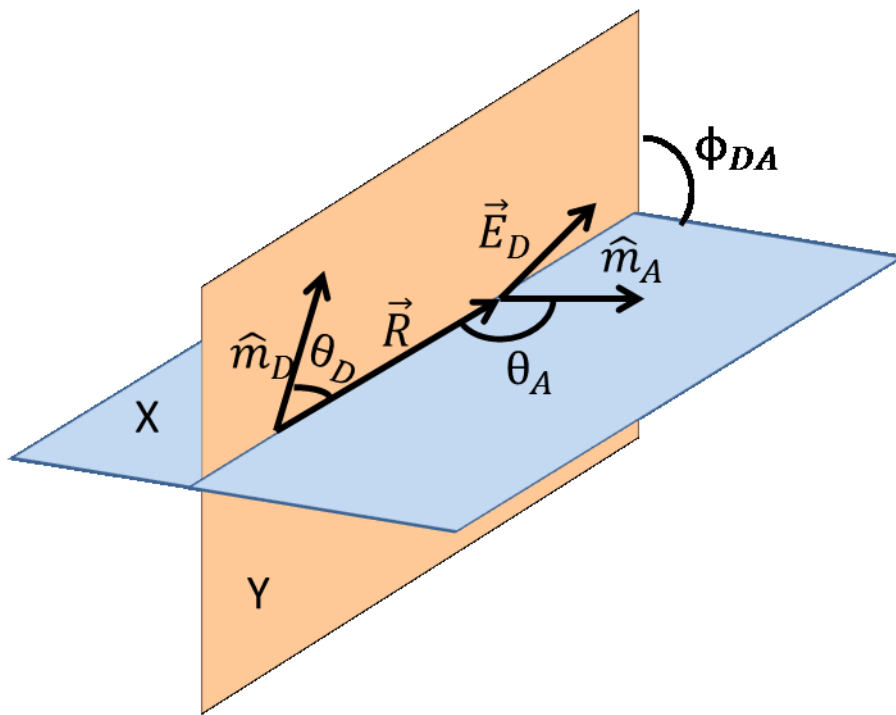


Figure 1.3: Relative orientation of a donor and an acceptor dipoles. The donor dipole lies on Y plane while the acceptor dipole lies on X plane. \vec{R} is the distance between two dipoles, ϕ_{DA} is the angle between the two planes, θ_D and θ_A are angles the dipoles make from vector joining two dipoles and \hat{m}_D and \hat{m}_A are unit vectors of donor and acceptor dipoles. This figure is adapted from (8).

In the expression (1.7), κ^2 is called the *orientation factor* of the dipoles. It can take values between 0 and 4. Let us consider a few situations to make this point more clear. If the two dipoles are perpendicular to each other and acceptor dipole is close to the donor dipole, but in the direction perpendicular to the donor dipole, then $\kappa^2 = 0$ (i.e., because, $\theta_D = \frac{\pi}{2}$, so $\cos \theta_D = 0$, and $\hat{\theta}_D \cdot \vec{m}_A = 0$). In this situation, even if the donor spectrum and acceptor spectrum overlap significantly, the transfer rate will be zero. In other situations $\kappa^2 \neq 0$ even if the dipoles are perpendicular to each other. Another trivial

example when dipoles are parallel to each other and $\hat{r}_{DA} \cdot \vec{m}_A = 1$. If $\theta_D = 0$ and the dipoles stack on each other then, $\kappa^2 = 4$. But when $\theta_D = \frac{\pi}{2}$ then $\kappa^2 = 1$. Since there are always fluctuations in the positions and angles of donor and acceptor molecules, the actual values are the ensemble average or time average. In this situation the average value of $\kappa^2 = 2/3$ is quite satisfactory. When interpreting the conformational changes of macromolecules, κ^2 is assumed to be constant. However, it should be kept in mind that the assumption $\kappa^2 = 2/3$ and that κ^2 remains constant is not a rigorous assumption by any means. In FRET experiments when fluorescent proteins are used as markers, κ^2 becomes important variable and averages are not applicable.

1.3.3 FRET - An excellent tool to study protein-protein interaction

FRET is a measure of interaction between interacting molecules. To begin with, let us consider the ensemble of donor and acceptor molecules as shown in Fig. 1.4. The donor and acceptor molecules are fluorescent and are excited at different wavelengths. Let us consider that the ensemble of molecules is exposed to the excitation wavelength at which the donors get excited and at that wavelength either the acceptors gets excited very little or not at all. This situation is depicted in Fig. 1.4. When the donors and the acceptors are far apart, i.e., non-interacting, the donors are brighter and fluorescing, as can be seen from many rays coming out of them. On the other hand, the acceptor molecules are depicted as dim fluorescing molecules and a few rays are coming out of them. However, when the molecules are very close to each other, i.e., the molecules are interacting, the donor molecule loses its energy to the acceptor molecule through dipole-dipole coupling non-radiatively. Therefore, the acceptor molecule gets brighter and the donor molecule becomes dimmer.

By tagging the proteins of interest with donor and acceptor fluorescent markers, FRET can be used to study the interaction between the interacting proteins in living cells. The resolution of the images obtained from the optical microscopes is limited by their diffraction limit which is of the order of $\sim 0.3\mu\text{m}$ and the interaction within nm cannot be observed using these microscopes. Since the energy transfer between the donors and acceptors occurs over the distances 1-10nm, a FRET signal obtained corresponding to a particular location within the microscope gives addition information surpassing the optical resolution of the microscope. Thus, within the voxel of microscopic resolution, FRET resolves the distance between the donor and acceptors down to molecular scale which is beyond the microscopic limit. Thus, FRET is an artificial lens through which the distances between the donor and acceptors can be resolved. This situation is illustrated in Fig. 1.5.

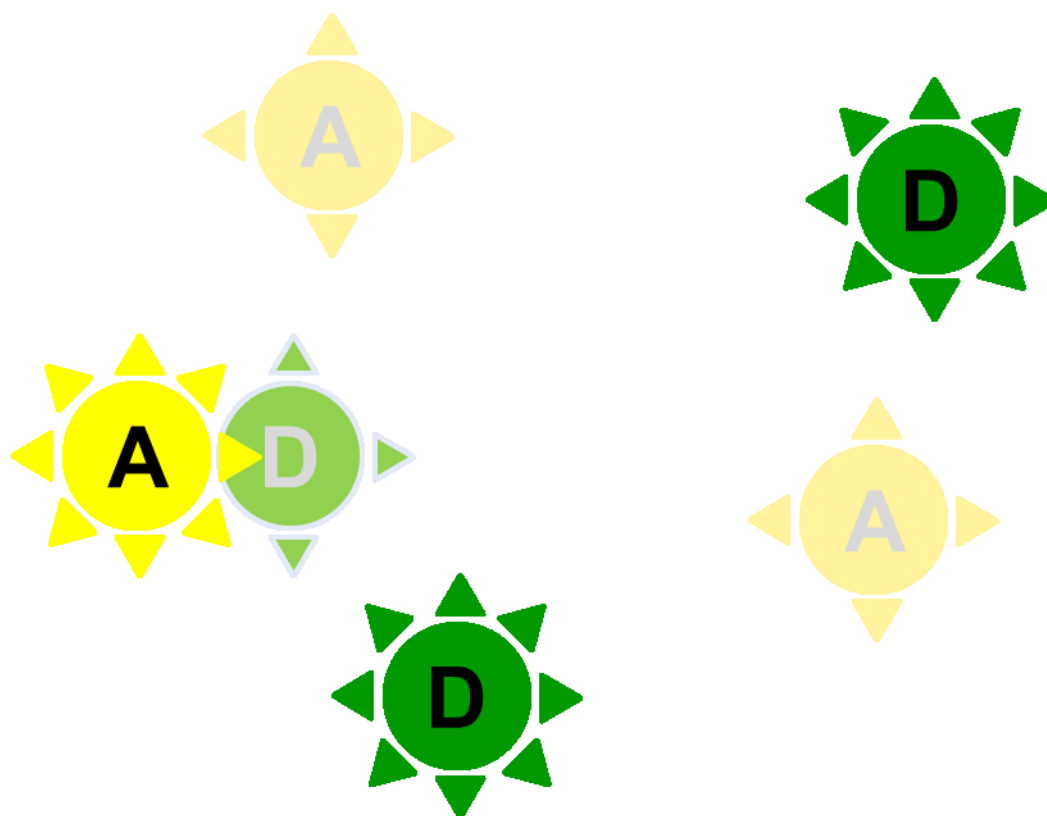


Figure 1.4: Visual illustration of FRET between a donor and an acceptor. When the donor (D) and the acceptor (A) molecules are not interacting, donors are brighter and the acceptors are dimmer. When the donor (D) is interacting with an acceptor (A), FRET occurs between D and A. Because of FRET non-radiative transfer of energy occurs between D and A, and that makes the acceptor brighter and the donor dimmer.

The unique feature of FRET microscopy is its ability to demonstrate the intimate interactions of molecules labeled with donor and acceptor fluorophores apart from visualizing the colocalization of donor and acceptor labeled probes within $\sim 0.09 \mu\text{m}^2$. FRET measurements can provide a wealth of information regarding structure and molecular interactions. It is easy to perform fluorescent measurements. However, because of the heterogeneous, highly structured and complex environment of the samples, it is difficult to quantify FRET. The successful analysis of FRET data depends

on the correct controls and corrects choice of the method to carry out the FRET measurements on the particular sample.

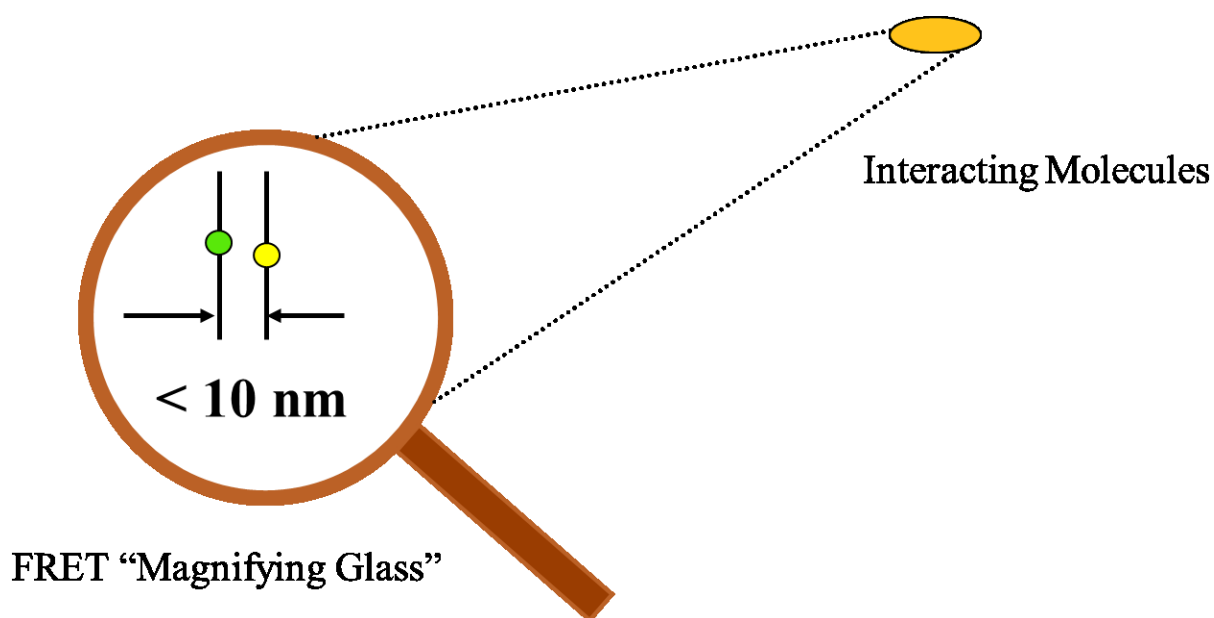


Figure 1.5: Illustration of FRET as a magnifying glass. The distances between the donor and the acceptor molecules that cannot be resolved by light microscope, can be resolved by FRET, hence FRET can be thought of imaginary lens to resolve the distances less than 10nm.

1.3.4 Förster radius for different FRET pairs

The interactions between the interacting molecules are quantified by measuring the FRET efficiency. It is defined as the fraction of excitations that transferred from an excited donor molecule to nearby unexcited molecule through dipole-dipole coupling over all possible de-excitation pathways of the excited donor. As you will see in chapter 2, the FRET efficiency of energy transfer between a donor and an acceptor is given by:

$$E = \frac{R_0^6}{R_0^6 + R^6} \quad (1.8)$$

where R is the distance between the donor and the acceptor, and R_0 is the Förster radius which is defined by (1.3). Alternatively, it can also be defined as the distance between a donor and an acceptor for which the energy transfer between them is 50%. Different types of FRET pairs are used in FRET spectroscopy depending upon its application in the problem of interest. The Förster radius for different pairs can be calculated using (1.3). In many FRET experiments, one needed to determine the distance between the fluorophores. For example, to determine the conformational changes in macromolecules based on FRET measurements, one needs to determine the distance between the donor and acceptor. The distance can be determined using (1.9) provided the Förster radius for that FRET pair is known. Förster radius can be determined experimentally using (1.3). The Förster radius for some FRET pairs such as: GFP-YFP pair is determined 5.6 nm (12), for CFP-YFP is 4.9 nm (12), for Cy3-Cy5 is 6.1 nm (13) and for GFP2-YFP is 5.5nm (14).

1.4 Challenges in FRET measurements

Many issues complicate the FRET measurements and sometimes give meaningless or misleading results (1, 15, 16). The problems encountered include autofluorescence, detector, relative brightness of donor and acceptor fluorophores, optical noise, photo-bleaching, and spectral bleed-through of signals. But, the major issues are due to relative brightness of donor and acceptor fluorophores and spectral bleed-through, sometimes also called crosstalk. In theory, the relative brightness of donor and acceptor fluorophores should not be a problem, but due to the limited dynamic range of most of the instruments, it is possible that the signal emanating from the brighter fluorophore

saturates the detector channel. On the other hand the signal from the dimer fluorophore is lost or more affected by the systematic noise. However, it has been observed that the fluorophores having comparable brightness yield satisfactory results. Another factor that limits the detection of FRET is the donor-to-acceptor ratio outside the range of 10:1 to 1:10 (17). The main problem is then measuring a small amount of FRET signal in the background of fluorophores not involved in FRET. Many protein-protein interaction experiments that fall outside this category are not suitable for examination by FRET.

Another pitfall in FRET experiments is due to bleed-through or cross talk between the two fluorophore colors. The light used to excite the donor can also directly excite the acceptor that leads to the excess acceptor emission that does not result from FRET. This artifact is called acceptor *spectral bleed-through* (ASBT). Again, the fluorescence from the donor can leak into the acceptor detection channel. This artifact is called donor spectral bleed-through (DSBT). The DSBT and ASBT are shown in Fig. 1.6 for SCFP3A-SYFP2 FRET pair. Since the bleed-through arises from the photo physics of the fluorophores and hence is present in all FRET pairs, this should be addressed before FRET measurements are made. Choosing fluorophores that are spectrally separated from each other reduces the cross-talk which also reduces the overlap of donor emission spectrum and acceptor excitation spectrum and hence the overlap integral J . This reduces the FRET detectability but helps eliminating cross-talk problem. In our experiments, we addressed this problem using spectral FRET and choosing FRET pairs for which ASBT is negligible and is discussed in chapter 4.

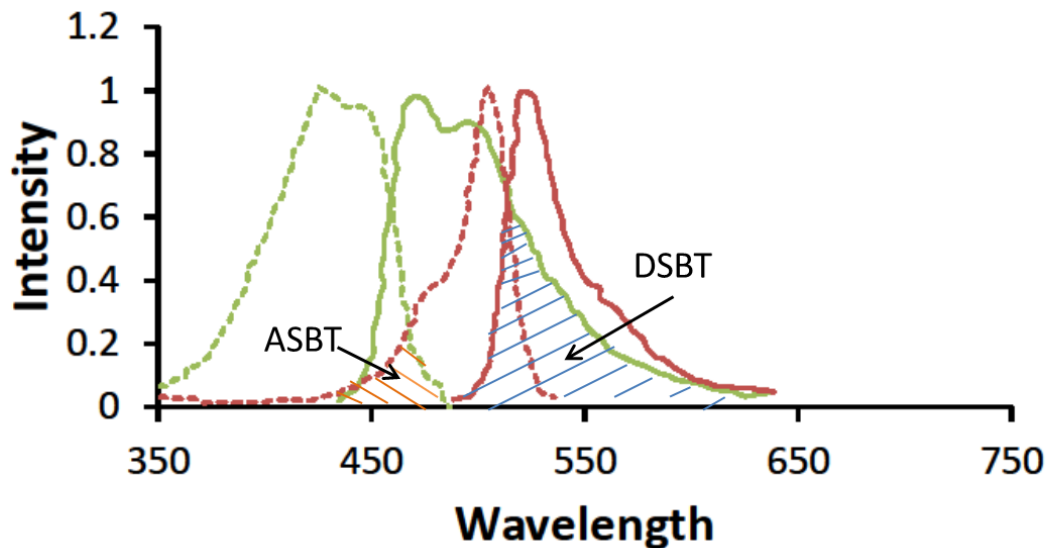


Figure 1.6: Excitation and emission spectrum of SCFP3A (donor) and SYFP2 (acceptors). The excitation spectrum of SCFP3A (dashed green line), emission spectrum of SCFP3A (solid green line), excitation spectrum of SYFP2 (dashed red line), and the emission spectrum of SYFP2 (solid red line) with different overlapping areas are shown. The region shaded with blue lines is called donor spectral bleed-through (DSBT) and the region shaded in orange is called acceptor bleed-through (ASBT). The emission spectra are measured in our lab and absorption spectra are adopted from (6).

1.5 Techniques of FRET imaging

1.5.1 Sensitized emission

Sensitized emission, also known as ratiometric imaging, is the simplest technique for measuring FRET. This imaging can be done on a standard wide field microscope equipped with proper fluorescent filter sets. The sample that contains both donors and acceptors is excited by donor excitation wavelength. The donor fluorescence and acceptor fluorescence is collected by using filter sets tuned for either donor or acceptor fluorescence. If there would have been no crosstalk in the excitation and emission spectrums of the fluorophores, it would have been very easy to calculate FRET from the gathered acceptor fluorescence and donor fluorescence. But, in reality, the collected donor and acceptor signals are contaminated due to bleed-through signals. Therefore, many control experiments are needed to clean the data from bleed-through and it is difficult to quantify FRET using this method (18).

To this goal, the images from cells expressing donor-only, acceptor-only and cells expressing both donor and acceptors are collected using different filter sets. This permits the determination of expected cross-talk in both excitation and emission channels. This cross-talk is subtracted from the FRET signal. Many algorithms for sensitized FRET imaging have been developed (19, 20). Despite all these difficulties, when the FRET efficiency is large, sensitized emission is a quite useful technique. It can be a very useful method for detecting dynamic interactions, because acquisition of the two images is simultaneous. Sensitized emission can also be used for any intensity-

based imaging system that includes total internal reflection (TIRF), spinning disk, or laser scanning confocal microscopy. When the interactions between the donors and the acceptors are weak, the amount of noise in the final FRET image exceed the level of sensitized emission because of all the necessary correction factors and does not give good results. Furthermore, these controls must be subjected to considerable image processing in order to subtract bleed-through, a limitation that slows acquisition times, increases the noise level, and introduces a relatively high degree of uncertainty into the measurements.

1.5.2 Acceptor photo-bleaching

When donors and acceptors are sufficiently close to each other, the fluorescence of the donor is reduced because of the presence of an additional de-excitation pathway of energy transfer from donor to acceptor through dipole-dipole coupling. This reduction in the fluorescence of donor in the presence of acceptor is called *donor quenching* and the increase in the fluorescence of acceptor due to FRET is called *acceptor sensitization*. In acceptor photo-bleaching, also commonly known as donor de-quenching, the fluorescence of donor is measured in the presence of acceptor. Since some of the donor energy is transferred to acceptor this donor fluorescence is quenched. Again, the acceptors are photo bleached by exposing them to light for a longer time without affecting donors. The photo bleached acceptors release the quenched energy and increase the donor fluorescence. If there was a FRET between the donor and the acceptor, photo-bleaching of acceptor must increase the fluorescence of donor. The fluorescence of de-quenched donors is measured. It is important in these experiments to ensure that the photo-bleaching of acceptors does not degrade the donors and the acceptors are photo-

bleached to 10% of their initial value. These constraints can be easily met with the use of laser scanning confocal microscope.

This method avoids the spectral bleed-through problem. Moreover, this method is straightforward, quantitative and requires only one sample. The apparent efficiency, which is a measure of interaction, is calculated by subtracting the fluorescence intensity of donors in the presence of acceptors from de-quenched donors, and by dividing this with the fluorescence of de-quenched donors. If $I^{D, pb}$ is the fluorescent intensity of donor after de-bleaching, I is the fluorescence intensity of donor in the presence of acceptor, the apparent FRET efficiency, E_{app} , in acceptor photo-bleaching method is calculated using the following equation:

$$E_{app} = \frac{I^{D, pb} - I}{I^{D, pb}}. \quad (1.9)$$

To perform the FRET measurements based on acceptor photo-bleaching, the acceptors should be photo-destructive enough so that it takes less time to be bleached while the donor should take longer time to be destroyed by photons. The example of such FRET pair is Cy3-Cy5. In a positive note, the FRET measurements based on acceptor photo-bleaching require no control experiment, which renders this technique among the most accurate techniques for measuring FRET.

The disadvantage of this method is that it is destructive. As a result, it can be used only once and is not suitable for dynamic measurements. This approach can also be slow depending on how long it takes to photo-bleach the acceptor.

1.5.3 Fluorescence lifetime imaging microscopy

Fluorescence lifetime imaging microscopy (FLIM) is a method that measures the time taken by the fluorophore to reach the ground state from excited state while releasing the photon. This method to measure FRET is less prone to cross-talk artifacts and is the most rigorous method (21). The concept of FLIM is related to acceptor photo-bleaching. The fluorescence intensity decay that all fluorescent molecules show on a nanosecond timescale is sensitive to environmental factors that quench the fluorescence. Because of FRET between a donor and acceptors, the donor fluorescence is quenched and this can be measured by the decrease in the fluorescence lifetime of the donor in the presence of acceptors. Thus, FLIM gives the accurate value of FRET efficiency. On a positive note, FLIM is not affected by the direct excitation of acceptors unlike other methods and even the acceptors which are not fluorescent can also be used (12). This expands the number of fluorescently tagged protein-FRET pairs that can be used in this method.

There are two techniques for measuring the fluorescence lifetimes, time domain FLIM and frequency domain FLIM. In frequency domain, the fluorescence lifetime is measured from the phase shift and the demodulation of the fluorescent light with respect to the phase and the modulation depth of the modulated excitation source. On the other hand, the fluorescence lifetime in the time domain FLIM is measured by measuring the

fluorescence time decay of the sample by exciting it with suitable light. Lifetime measurements can be performed both in wide field and in scanning microscopes such as confocal microscopes and two-photon microscopes. FLIM allows us to understand the environment of a protein at atomic resolution, down to 8nm, far greater than what is possible with even electron microscopy.

However, there are many challenges associated with this method, which limit its applicability in FRET imaging. The fluorescent lifetimes are of the order of nanoseconds and the detection systems of high time resolution are expensive to obtain and to maintain and are not yet widely available. Moreover, FLIM is very slow. It requires several minutes to acquire a single image. Hence, this method cannot be used to study interactions which are dynamic and occur in less time than required to collect the image. In addition, the fluorescent proteins in living cells have more than one lifetimes which require the acquisition of more comprehensive data for FRET analysis. This further slows the FLIM-FRET measurements. The environmental factors such as the pH change, autofluorescence can shorten the fluorescence lifetime and sometimes may give misleading results, hence, while interpreting the FLIM-FRET data in living cells care must be taken. Also, this system cannot be used for the determination of stoichiometry of proteins larger than the order of dimers, because in that case, many combinations of oligomers depending upon the number of donors and acceptors and their position within each oligomer is possible and each configuration will give different fluorescence lifetime. Due to large number of lifetimes in each pixel, it is impossible to fit the experimental data with exponential functions corresponding to lifetimes of different configurations.

1.5.4 Spectral imaging

Spectral imaging is a form of imaging where the total spectral fluorescence emanating from each voxel of the sample that contains both donor and acceptor fluorescence is collected by the detector at once on the excitation wavelength of the donor. Unlike sensitized emission, filters are not used to collect donor fluorescence and acceptor fluorescence. The sample expressing donors only and acceptors only are used to get the spectrum of the donor and the acceptor. The spectrum containing both donor and acceptor components are spectrally unmixed using the donor only and acceptor only spectrum to get the donor fluorescence and acceptor fluorescence (22, 23). This method requires special spectral imaging equipment and is readily available with confocal microscopes or can be added to conventional fluorescence microscopes at modest cost. The use of two excitation wavelengths or the previous determination of the cross talk due to the direction excitation of acceptor permits the determination of FRET (17). With the development of more commercial systems, the use of spectral imaging is increasing. In the future, it is expected that the spectral imaging will be one of the main methods for performing FRET imaging.

1.5.5 Polarization anisotropy imaging

This method can provide information about size and shape of protein or the rigidity of the molecular environments. It is based on the measurement of fluorescence polarization (24). When the polarized light falls on the fluorophores, the fluorophores whose transition dipole moments are in the direction of electric field of the polarized light will absorb the photon. Thus, one excites the molecules selectively (see Figure 1.7). This selective excitation results in partially polarized emission. The relative angles between

the excitation moment and emission moment determine the maximum measured anisotropy of the fluorescent molecules. When the sample is excited by the vertically polarized light, the fluorescence anisotropy, r , and polarization, P , are defined as:

$$r = \frac{I_{\parallel} - I_{\perp}}{I_{\parallel} + 2I_{\perp}}, \quad (1.10)$$

and

$$P = \frac{I_{\parallel} - I_{\perp}}{I_{\parallel} + I_{\perp}}, \quad (1.11)$$

where I_{\parallel} and I_{\perp} are the fluorescence intensities of the vertically and horizontally polarized emission. The rotational diffusion of the molecules can decrease the anisotropy of the fluorophores (Fig. 1.7). Such diffusions displace the transition dipoles and occur during the lifetime of the fluorophore. In fluorescent proteins, because of their large size, the rotational diffusions are slow; hence the depolarization rate of fluorescence is little. If the FRET occurs between the two FPs that are slightly misaligned then the measured fluorescence will be coming out of different angle which is the same as the rotation of FP.

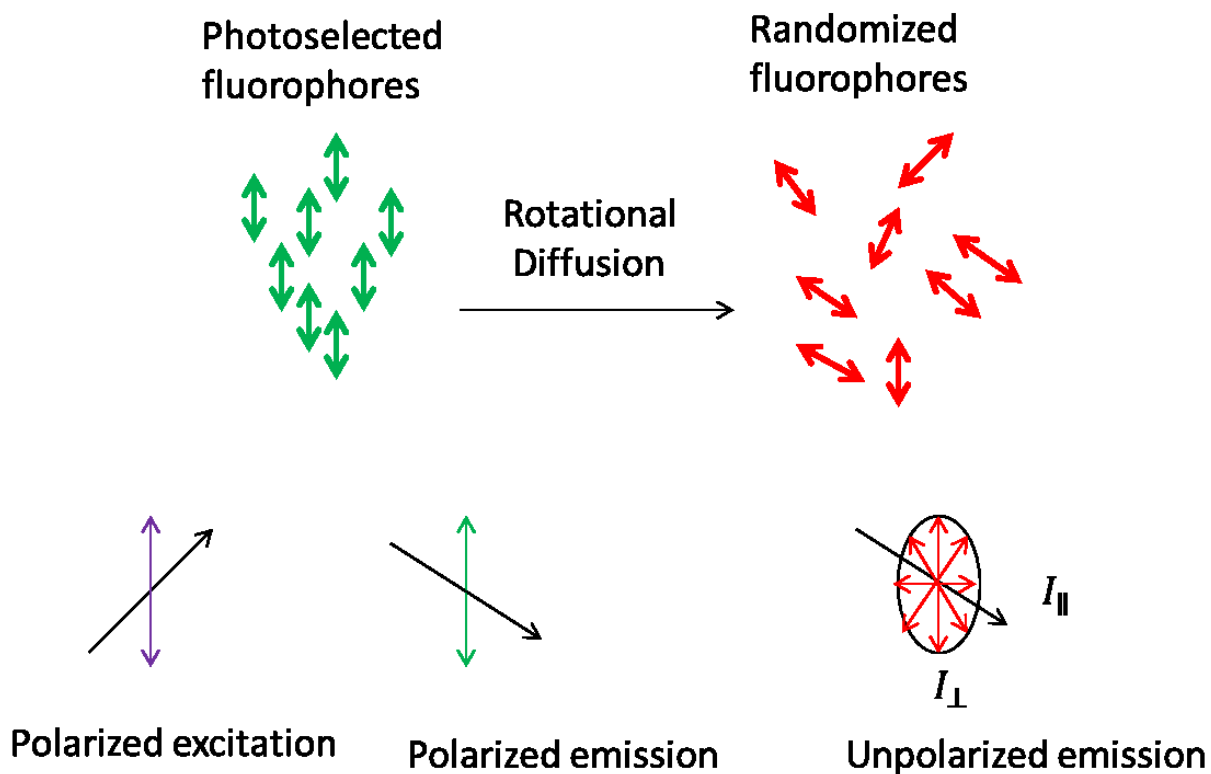


Figure 1.7: Illustration of effect of polarized excitation and rotational diffusion on the fluorescence. This figure is adapted from (2).

The polarization FRET technique is most useful for investigating the presence or absence of FRET; however, it is not good at differentiating the weak and strong FRET.

1.6 Application of FRET in biology

FRET has been used in many biological problems. A few important applications of FRET are discussed below.

1.6.1 Detection of heteromerization of more than two proteins

To decode the properties of molecular networks that control intercellular communication, it is important to identify the formation of higher order oligomers in the plasma membrane. G-protein coupled receptors (GPCRs), seven transmembrane spanning receptors, play a significant role in communication systems throughout the animal kingdom. However, their function is specific for a given cell and/or condition and depends on the occurrence of oligomeric complexes formed by them. The ligands induce conformational changes within the oligomer and modify the proteins' signaling, pharmacology and trafficking (25-27). Therefore, it is necessary to understand the proteins interacting within the oligomers to understand the mechanism underlying endocrine communication and cell transmission.

To study the protein-protein interaction, co-immunoprecipitation followed by Western blotting, is primarily used. However, co-immunoprecipitation requires the solubilization of membranes to extract membrane proteins. Thus, the complexes observed by this method may be the artifacts of the solubilization. The method proposed by Carriba et al. (28) is based on bioluminescence resonance energy transfer (BRET) and fluorescence resonance energy transfer (FRET) and demonstrates the heteromeric protein-protein interaction in living cells and overcomes the technical limitations involved in the coimmunoprecipitation. Carriba and co-workers combined BRET and FRET in a technique called sequential BRET-FRET (SRET) to identify the heterotrimers formed by three different proteins. They fused one protein to Renilla luciferase (Rluc), the second protein to BRET acceptor (GFP or YFP) and the third protein to the FRET

acceptor (YFP or DsRed). The oxidation of Rluc by the Rluc fusion protein triggers the acceptor excitation through BRET and subsequently the energy from excited BRET acceptor is transferred to FRET acceptor. Using SRET they identified the interaction of cannabinoid CB₁, dopamine D₂ and adenosine A_{2A} receptors in living cells. The method developed by them is a suitable tool to understand the nature of protein assemblies and their interface in living cells.

1.6.2 Tracking SNARE complex formation in live endocrine cells

Syntaxin (Syx), synaptosome-associated protein of 25kD (SNAP25), and vesicle-associated membrane proteins/ synaptobrevin (Syb) are collectively called SNARE proteins. These proteins are responsible for catalyzing neuronal exocytosis by forming a core complex. An et al. (29) used FRET to track SNARE complex formation in live endocrine PC12 cells. To understand the complex formation in living cells, An and co-workers made a fluorescent SNAP25. The cyan fluorescent protein (CFP) was FRET donor while the fluorescent protein, Venus was FRET acceptor in their experiment. When this fluorescent protein enters in SNARE complex, the intermolecular Fluorescence Resonance Energy Transfer occurs. SNAP25 is SN1 connected to SN2 separated by 50 amino acid long linker. SN1 and SN2 are called SNARE motif regions. When SNAP25 is alone, SN1 and SN2 are unstructured. However, when SNAP25 forms a complex with Syx and Syb, SN1 and SN2 fold as parallel helices within a four –helix bundle, and the N-terminals of SN1 and SN2 reach close to each other.

1.6.3 Probing calcium ion concentration changes in living cells

CHO cells expressing M1 muscarinic acetylcholine receptors were used to probe the concentration changes of calcium ions. Premo Cameleon FRET biosensors (Life Technologies) were used to probe the calcium ion concentration changes within the cell. This sensor consists of fluorophores eCFP and cpVenus that are connected by a calmodulin-M13 moiety. When four calcium ions bind to calmodulin, a conformational change occurs in the biosensor that brings the fluorophores together and causes increase in FRET efficiency. By monitoring the changes in FRET efficiency in the cell or in an organelle of the cell the concentration changes in the cell or in the organelle can be probed.

Stoneman and co-workers (30) transduced CHO cells expressing M1 receptors (CHO M1WT3, ATCC; Manassas, VA) using BacMAM transduction protocol to express the Premo Cameleon biosensors (Life Technologies). Cells expressing the Cameleon sensor were imaged using optical micro-spectroscopy (OptiMis). The cells were treated with 500 μ M carbachol, a muscarinic receptor agonist, and imaged over an extended period of time at intervals of 15 seconds. The change in FRET efficiency distribution of a cell before and after treatment of carbachol is shown in Fig. 1.8 (A). The effect of carbachol addition on FRET efficiency with time, is shown in Fig. 1.8 (B).

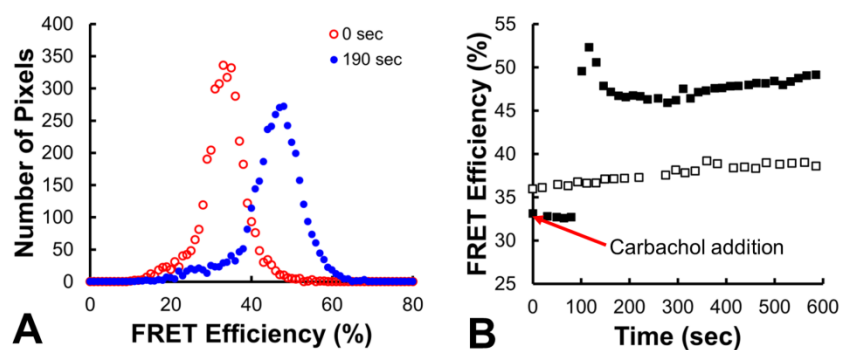


Figure 1.8: Distributions of FRET efficiencies in CHO cells expressing the rat M1 muscarinic receptor and the Premo Cameleon FRET Biosensor. (A) FRET efficiency histograms obtained for a single cell before and 190 s after addition of agonist (carbachol). (B) Average value of FRET efficiency histograms obtained at several time points before (open squares) and after addition of carbachol (solid black squares). The open squares are the average of the FRET efficiency histogram for a cell scanned in a similar manner as the carbachol-treated cell, but never exposed to carbachol.

1.6.4 Measuring energetics of membrane protein dimerization

Due to many experimental challenges, the interactions between the membrane proteins are the least well-characterized (31, 32) of protein interactions. This difficulty is because most of the mammalian transmembrane proteins are alpha helical, though there are some studies of interaction energetics of transmembrane (TM) helices in TM bilayers (33-35) carried out in detergent micelles. To better understand biological processes, it is necessary to measure the strength of TM helix association in the natural cell environment. Glycophorin A (GpA), the primary sialoglycoprotein of the human erythrocyte membrane, is a widely studied protein in terms of dimerization energetics. It has been shown by some investigators that GpA has propensity for sequence specific dimerization in detergents and in bacterial membranes (36, 37). Chen and co-workers measured the energetics of GpA TM domain dimerization in vesicles derived from mammalian

membrane. To study plasma membrane lipids and proteins, vesicles are used as model system (38). The authors used quantitative imaging Förster resonance energy transfer (QI-FRET) to determine the equilibrium constant of dimerization K_D (39) and using the equation:

$$\Delta G = -RT \ln K_D, \quad (1.12)$$

where, ΔG is the change in the Gibbs free energy, R is the ideal gas constant and T is the equilibrium temperature, calculated the change in free energy of dimerization which was -3.9 ± 0.2 kcal/mol. This is the first quantitative measure of the dimerization energetics of a membrane protein in mammalian membranes. The free energy of GpA dimerization can be used as a standard for other interaction energies for comparison.

1.6.5 Stoichiometry determination of protein complexes

Raicu and co-workers (23) used spectrally resolved FRET to determine the stoichiometry of the alpha-factor receptor protein Ste2 (Ste2p), a yeast mating protein (40). Their method relies on both sensitized acceptor emission and on donor-dequenching (also called acceptor photo-bleaching). They tagged Ste2p with CFP, GFP and YFP to obtain Ste2p-CFP, Ste2p-GFP, and Ste2p-YFP, respectively. CFP and GFP tagged proteins were donor of energies while YFP tagged protein acted as acceptor of energy in FRET processes. The authors calculated the apparent FRET efficiencies for Ste2p-CFP/Ste2p-YFP and Ste2p-GFP/Ste2p-YFP FRET pairs and based on the theoretical model presented by them, determined that the Ste2p protein is dimeric.

1.7 Other applications of FRET in biology

We have already discussed some important applications of FRET in biology. Here, we briefly describe other biophysical and biological applications of FRET. Parson and co-workers (41) used FRET to analyze the molecular interactions and conformational changes in various proteins involved in the regulation of cell adhesion and motility. Pearce et al. (42) used FRET to study the role of metallothionein (MT) in nitric oxide signaling. MT is a 6- to 7-kDa cysteine –rich metal binding protein and is an important component of intracellular redox signaling, including a target for nitric oxide. Hink et al. studied the dynamic complexes formed by proteins in plant cells using FRET (43). Heyduk et al. (44) highlighted the application of FRET in the measurement of the distances between macromolecules and conformational changes in proteins at single molecule level in the native *in vivo* context of a living cell. Coarsi et al. (45) presented a fuzzy nanostructured system called a *nano-capsule* as a nanometric device to allow distance modulation that preserved the photo physical properties of the fluorescent dyes and exhibits good potential features for improving quantitative FRET analysis. These authors used three steady-state fluorescence methods and one fluorescence life-time based method to evaluate the behavior of such a sample. These nano-devices developed by the authors can be used as a benchmark system for characterizing new FRET couples and for the development of quantitative FRET analysis. Lleres and co-workers (46) used FRET in conjunction with multi-photon fluorescence lifetime microscopy (FLIM) to study chromatin compaction in living cells at the scale of nucleosomal arrays. They tagged histone H2B either with enhanced green fluorescent protein (FP) or with m-Cherry FPs to express them in human cell lines. FRET can take place between the

nucleosomes tagged with separate FPs and increases when the chromatin compacts. Their results were consistent with the higher order chromatin compaction during anaphase. Raicu and co-workers (47) used spectral FRET to determine the quaternary structure of yeast mating protein Ste2p. For that they tagged Ste2p with GFP2 and Ste2p with YFP and coexpressed these proteins in yeast cells. The cells expressing both proteins were imaged and distribution of FRET efficiencies was obtained. This distribution of FRET efficiencies was simulated against theoretical models developed by Raicu and his team to get the quaternary structure and stoichiometry of Ste2p protein. In contrast to their previous study (Raicu, 2005) this time they showed using spectral FRET that Ste2p is tetrameric. Demarco et al. (48) developed an imaging method based on the photoactivated green fluorescent protein (PA-GFP) and FRET microscopy. They used this method also known as photoquenching FRET (PQ-FRET) to monitor dynamic interactions of the heterochromatin protein-1 alpha ($HP1\alpha$) and the transcription factor CCAAT/enhancer binding protein alpha ($C/EBP\alpha$) in region of centromeric heterochromatin in mouse pituitary cells. More quantitatively, FRET has been used for determining the average size of the oligomers from average FRET efficiency values of populations of interacting molecules (49, 50) as well as the average fraction of associated versus unassociated monomers in a population of homo-oligomerizing proteins (39). Using spectral FRET Pisterzi et al. determined that M2 muscarinic receptors form tetramers in the living cells. Maurel and co-workers (50) developed a method based on FRET in conjunction with Snap-tag technology to quantify the protein-protein interaction at the surface of living cells. Using this technology they concluded that class A and class C, G proteins-coupled receptors (GPCRs) form oligomers. Chen et al. (39) used FRET to

determine the contribution of the extracellular domain of fibroblast growth factor receptor 3 (FGFR3) to the dimerization of the receptor. Albizu et al. (51) used time-resolved FRET to report the oligomerization of GPCRs in their native tissues. Chapman et al. (52) used FRET to study the interactions between calmodulin and the tryptophan residues of synthetic peptides. Those as well as other applications are discussed more extensively in review articles and books (see, e.g., (2, 10, 53)).

References

1. Piston, D. W. and Kremers, G. J. (2007) Fluorescent protein FRET: the good, the bad and the ugly. *Trends in Biochemical Sciences* **32**:407-414.
2. Lakowicz, J. R. (2006) *Principles of Fluorescence Spectroscopy* (Springer, New York, NY, USA).
3. Shimomura, O., Johnson, F. H., and Saiga, Y. (1962) Extraction, purification, and properties of aequorin, a bioluminescent protein from the luminous hydromedusan, *Aequorea*. *J. Cell. Comp. Physiol.* **59**:223-239.
4. Johnson, F. H., et al. (1962) Quantum efficiency of *Cypridina* luminescence, with a note on that of *Aequorea*. *J. Cell. Comp. Physiol.* **60**:85-103.
5. Chalfie, M., Tu, Y., Euskirchen, G., Ward, W. W., and Prasher, D. C. (1994) Green Fluorescent Protein as a Marker for Gene-Expression. *Science* **263**:802-805.
6. Chalfie, M. (1995) Green fluorescent protein. *Photochem Photobiol* **62**:651-656.
7. Wang, S. X. and Hazelrigg, T. (1994) Implications for Bcd Messenger-Rna Localization from Spatial-Distribution of Exu Protein in *Drosophila* Oogenesis. *Nature* **369**:400-403.
8. Clegg, R. M. (1996) Fluorescence resonance energy transfer. *Fluorescence Imaging Spectroscopy and Microscopy*, Chemical Analysis, eds Wang X. F. and Herman B. (John Wiley & Sons, Inc), Vol 137.
9. Selvin, P. R. (1995) Fluorescence resonance energy transfer. *Methods Enzymol.* **246**:300-334.
10. Raicu, V. and Popescu, A. I. (2008) *Integrated Molecular and Cellular Biophysics* (Springer, London, United Kingdom).
11. Forster, T. (1965) Delocalized excitation and excitation transfer. *Modern quantum chemistry*, ed Sinanoglu O. (Academic press inc., New York), Vol III.
12. Ganesan, S., Ameer-beg, S. M., Ng, T. T. C., Vojnovic, B., and Wouters, F. S. (2006) A dark yellow fluorescent protein (YFP)-based Resonance Energy-

- Accepting Chromoprotein (REACH) for Forster resonance energy transfer with GFP. *Proc. Natl. Acad. Sci. USA* **103**:4089-4094.
13. Iqbal, A., *et al.* (2008) Orientation dependence in fluorescent energy transfer between Cy3 and Cy5 terminally attached to double-stranded nucleic acids. *Proc. Natl. Acad. Sci. USA* **105**:11176-11181.
 14. Zimmermann, T., Rietdorf, J., Girod, A., Georget, V., and Pepperkok, R. (2002) Spectral imaging and linear un-mixing enables improved FRET efficiency with a novel GFP₂-YFP FRET pair. *FEBS Lett.* **531**:245-249.
 15. Periasamy, A. and Diaspro, A. (2003) Multiphoton microscopy. *J Biomed Opt* **8**:327-328.
 16. Vogel, S. S., Thaler, C., and Koushik, S. V. (2006) Fanciful FRET. *Sci STKE* **2006**:re2.
 17. Chen, H., Puhl, H. R., Koushik, S., Vogel, S., and Ikeda, S. (2006) Measurement of FRET efficiency and ratio of donor to acceptor concentration in living cells. *Biophys. J.* **91**:L39-41.
 18. van Rheenen, J., Langeslag, M., and Jalink, K. (2004) Correcting confocal acquisition to optimize imaging of fluorescence resonance energy transfer by sensitized emission. *Biophys J* **86**:2517-2529.
 19. Hoppe, A., Christensen, K., and Swanson, J. A. (2002) Fluorescence resonance energy transfer-based stoichiometry in living cells. *Biophys. J.* **83**:3652-3664.
 20. Periasamy, A. and Day, R. N. (1999) Visualizing protein interactions in living cells using digitized GFP imaging and FRET microscopy. *Methods Cell Biol* **58**:293-314.
 21. Day, R. N. and Piston, D. W. (1999) Spying on the hidden lives of proteins. *Nat. Biotechnol.* **17**:425-426.
 22. Wu, P. G. and Brand, L. (1994) Resonance Energy-Transfer - Methods and Applications. *Anal Biochem* **218**:1-13.
 23. Raicu, V., Jansma, D. B., Miller, R. J., and Friesen, J. D. (2005) Protein interaction quantified in vivo by spectrally resolved fluorescence resonance energy transfer. *Biochem. J.* **385**:265-277.
 24. Mattheyses, A. L., Hoppe, A. D., and Axelrod, D. (2004) Polarized fluorescence resonance energy transfer microscopy. *Biophys J* **87**:2787-2797.
 25. Franco, R., *et al.* (2003) Regulation of heptaspanning-membrane-receptor function by dimerization and clustering. *Trends in Biochemical Sciences* **28**:238-243.
 26. Terrillon, S. and Bouvier, M. (2004) Roles of G-protein-coupled receptor dimerization - From ontogeny to signalling regulation. *EMBO Rep* **5**:30-34.
 27. Agnati, L. F., Ferre, S., Lluís, C., Franco, R., and Fuxe, K. (2003) Molecular mechanisms and therapeutical implications of intramembrane receptor/receptor interactions among heptahelical receptors with examples from the striatopallidal GABA neurons. *Pharmacol. Rev.* **55**:509-550.
 28. Carriba, P., *et al.* (2008) Detection of heteromerization of more than two proteins by sequential BRET-FRET. *Nat. Methods* **5**:727-733.
 29. An, S. J. and Almers, W. (2004) Tracking SNARE complex formation in live endocrine cells. *Science* **306**:1042-1046.

30. Stoneman, M. R., *et al.* (2012) Quantifying the efficiency of various FRET constructs using OptiMiS (TM). *Biotechniques* **52**:191-+.
31. MacKenzie, K. R. (2006) Folding and stability of alpha-helical integral membrane proteins. *Chemical Reviews* **106**:1931-1977.
32. Hong, H., Joh, N. H., Bowie, J. U., and Tamm, L. K. (2009) Methods for measuring the thermodynamic stability of membrane proteins. *Methods Enzymol* **455**:213-236.
33. Artemenko, E. O., Egorova, N. S., Arseniev, A. S., and Feofanov, A. V. (2008) Transmembrane domain of EphA1 receptor forms dimers in membrane-like environment. *Biochim. Biophys. Acta.* **1778**:2361-2367.
34. Merzlyakov, M., Chen, L., and Hristova, K. (2007) Studies of receptor tyrosine kinase transmembrane domain interactions: the EmEx-FRET method. *J Membr Biol* **215**:93-103.
35. Cristian, L., Lear, J. D., and DeGrado, W. F. (2003) Use of thiol-disulfide equilibria to measure the energetics of assembly of transmembrane helices in phospholipid bilayers. *Proc. Natl. Acad. Sci. USA* **100**:14772-14777.
36. Fisher, L. E., Engelman, D. M., and Sturgis, J. N. (1999) Detergents modulate dimerization, but not helicity, of the glycophorin A transmembrane domain. *J Mol Biol* **293**:639-651.
37. Finger, C., *et al.* (2006) The stability of transmembrane helix interactions measured in a biological membrane. *J Mol Biol* **358**:1221-1228.
38. Baumgart, T., *et al.* (2007) Large-scale fluid/fluid phase separation of proteins and lipids in giant plasma membrane vesicles. *Proc. Natl. Acad. Sci. USA* **104**:3165-3170.
39. Chen, L., Placone, J., Novicky, L., and Hristova, K. (2010) The extracellular domain of fibroblast growth factor receptor 3 inhibits ligand-independent dimerization. *Sci. Signal.* **3**:ra86.
40. Kurjan, J. (1992) Pheromone response in yeast. *Annu. Rev. Biochem.* **61**:1097-1129.
41. Parsons, M., Vojnovic, B., and Ameer-Beg, S. (2004) Imaging protein-protein interactions in cell motility using fluorescence resonance energy transfer (FRET). *Biochem. Soc. Trans.* **32**:431-433.
42. Pearce, L. L., *et al.* (2000) Role of metallothionein in nitric oxide signaling as revealed by a green fluorescent fusion protein. *Proc. Natl. Acad. Sci. USA* **97**:477-482.
43. Hink, M. A., Bisselin, T., and Visser, A. J. (2002) Imaging protein-protein interaction in living cells. *Plant Mol. Biol.* **50**:871-883.
44. Heyduk, T. (2002) Measuring protein conformational changes by FRET/LRET. *Curr. Opin. Biotechnol.* **13**:292-296.
45. Caorsi, V., *et al.* (2007) FRET measurements on fuzzy fluorescent nanostructures. *Microsc. Res. Tech.* **70**:452-458.
46. Lleres, D., James, J., Swift, S., Norman, D. G., and Lamond, A. I. (2009) Quantitative analysis of chromatin compaction in living cells using FLIM-FRET. *J. Cell Biol.* **187**:481-496.
47. Raicu, V., *et al.* (2009) Determination of supramolecular structure and spatial distribution of protein complexes in living cells. *Nat. Photonics* **3**:107-113.

48. Demarco, I. A., Periasamy, A., Booker, C. F., and Day, R. N. (2006) Monitoring dynamic protein interactions with photoquenching FRET. *Nat. Methods* **3**:519-524.
49. Pisterzi, L. F., *et al.* (2010) Oligomeric size of the M₂ muscarinic receptor in live cells as determined by quantitative fluorescence resonance energy transfer. *J. Biol. Chem.* **285**:16723-16738.
50. Maurel, D., *et al.* (2008) Cell-surface protein-protein interaction analysis with time-resolved FRET and snap-tag technologies: application to GPCR oligomerization. *Nat. Methods* **5**:561-567.
51. Albizu, L., *et al.* (2010) Time-resolved FRET between GPCR ligands reveals oligomers in native tissues. *Nat Chem Biol* **6**:587-594.
52. Chapman, E. R., Alexander, K., Vorherr, T., Carafiol, E., and Storm, D. R. (1992) Fluorescence energy transfer analysis of calmodulinpeptide complexes. *Biochemistry* **31**:12819-12825.
53. Selvin, P. R. (2000) The renaissance of fluorescence resonance energy transfer. *Nat. Struct. Biol.* **7**:730-734.

Chapter 2. Förster rate of energy transfer

In this chapter, we present a historical background of energy transfer, the classical derivation of energy transfer as described by Perrin, and the classical and quantum mechanical derivations of energy transfer by Förster. In addition, we derive the expressions for FRET efficiencies for different configurations of oligomers arranged in different geometries in terms of pair-wise FRET efficiency (i.e., the FRET efficiency between a donor and an acceptor), which will be used to determine the quaternary structure of proteins in chapter 6.

2.1 Historical background of resonance energy transfer

J. Perrin developed the early dipole-dipole interaction model of energy transfer in solutions (1, 2). He hypothesized that excitation energy could be transferred from one molecule to another through interactions between oscillating dipoles. Classically, the electric field due to an oscillating dipole, \vec{E} , decreases as the distance between the dipoles, R , increases. The electric field due to oscillating dipoles can be divided into three zones: the near field zone ($\vec{E} \propto R^{-3}$), the far-field zone ($\vec{E} \propto R^{-1}$), and the intermediate between the near-field and far-field. Dipole-dipole interaction had already been used to describe the molecular interactions in the bulk matter. Here, we are only interested in the dipole-dipole interaction energy in the near field. In this regime, the interaction energy is large compared to the energy in the other two zones. The non-radiative mechanism based on dipole-dipole interaction successfully accounted for the energy transfer in a gas mixture arising from the collision between atoms (1, 3, 4).

Perrin reasoned that the observed depolarization in a solution of fluorophore of high concentration is due to the excitation energy transfer between molecules of different orientations, before a photon is emitted. In his model, the interaction energy, E_{int} , between two oscillating dipoles of molecules, donor (D) and acceptor (A), was $E_{int} \propto \vec{E} \cdot \vec{m}_A$, where, \vec{m}_A is the dipole moment of the acceptors and \vec{E} the electric field due to donor dipole at acceptor dipole. This interaction energy is identical to the perturbation energy in the quantum mechanical description of FRET as described later in this chapter. Moreover, Perrin assumed that the molecules are identical (2, 5). Initially he presented the classical view of his model involving point dipoles; later his son, F. Perrin, also presented the quantum mechanical description of the model proposed by J. Perrin, where the point dipoles become the transition dipoles (6). The Perrins' (J. and F.) assumption that the energy transfer between the molecules involves dipole perturbations was correct as it was also realized by earlier researchers studying molecular interactions. However, their theory was unable to explain the energy transfer in solutions of identical molecules. It was known that at the concentrations of fluorophore solution when the molecules are separated by $\sim 2\text{-}5\text{nm}$ (7), the fluorescence becomes depolarized. However, their model to explain this depolarization predicted much longer distances between the molecules in order for energy transfer take place and hence the depolarization. Because of this discrepancy, the Perrins' theory of energy transfer lay dormant for about 20 years.

Förster appreciated that the assumption of dipole-dipole interaction proposed by Perrins to explain energy transfer in solutions was correct (1). According to Perrins the two oscillators can exchange energy only if the both oscillators have the exact same fundamental frequencies, i.e., the both oscillators are in resonance. However, Förster realized that the resonance condition as assumed by Perrins is not limited to single frequencies. Molecules in both ground and excited states have a distribution of energies, and particularly in solutions these distributions are even wider because of their vibrations and interactions with surrounding molecules. When the chromophore is excited to its Frank-Condon state (see below), the excited molecule rapidly relaxes to the equilibrium Boltzmann distribution of its vibrational and rotational states in less than a picosecond. These distributions are responsible for the shape and the width of the absorption and emission spectrum of the chromophores. Specifically, the absorption and emission spectra of isolated molecules are narrow, and broaden when the molecules are immersed in a liquid solution. Such distributions of energies affect significantly the probability per unit time of spectroscopic transitions and the rate of energy transfer.

During energy transfer, of course, energy must be conserved. Therefore, energy can be exchanged between donor and acceptor molecules only if the difference between their instantaneous final energy states and the initial energy states are equal. However, this resonance condition is distributed over all frequency values where the emission spectrum of donor and excitation spectrum of acceptor overlap. This drastically reduces the probability of meeting the resonance condition. Because of the spectral width, only a fraction of molecules are exactly in resonance at a time. Another condition for Förster

energy transfer is that the coupling between the two molecules is very weak, such that the absorption and emission spectrum of molecules are not influenced by the coupling, that is, the molecules interact with each other but still can be regarded as separate molecular species.

The probability that the vibrational frequency of the donor exactly matches the frequency of the acceptor is calculated by integrating the product between the donor's emission spectrum and the acceptor's absorption spectrum over the overlapping frequencies. This integral is also known as the *overlap integral*. Förster published a series of papers on this topic. In his first paper, he presented the simple probabilistic calculations, and soon thereafter he presented a thorough quantum mechanical account of energy transfer (8).

Förster's theory was in agreement with the experimental observations. The distance over which the molecules can effectively exchange energy without emitting or absorbing photons, predicted by Förster's theory, was much less than that predicted by Perrin's theory. The rate of energy transfer varies as $1/R^6$ in Förster's theory and as $1/R^3$ in Perrin's theory, where R is the distance between donor and acceptor. Förster's theory also takes into account the relative orientations of interacting dipoles and since then has been rigorously checked (1, 9).

2.2 Review of physical quantities needed for Förster's theory

2.2.1 Absorption and emission of radiation

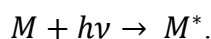
When an atom or molecule in the ground state characterized by the wave function $|i\rangle$ and energy E_i is subjected to electromagnetic radiation of frequency ν , it enters an excited state characterized by wave function $|f\rangle$ and energy E_f . The frequency ν , energy E_i , and energy E_f are related as:

$$\Delta E = E_f - E_i = h\nu. \quad (2.1)$$

Three absorption/emission processes may occur, as illustrated in Fig. 2.1-Fig 2.3 and are discussed below.

Absorption

In absorption, the molecule or atom M absorbs a quantum of energy and is excited from $|i\rangle$ to $|f\rangle$ to become M^* . This process is illustrated in Fig. 2.1 and can be represented as follows:



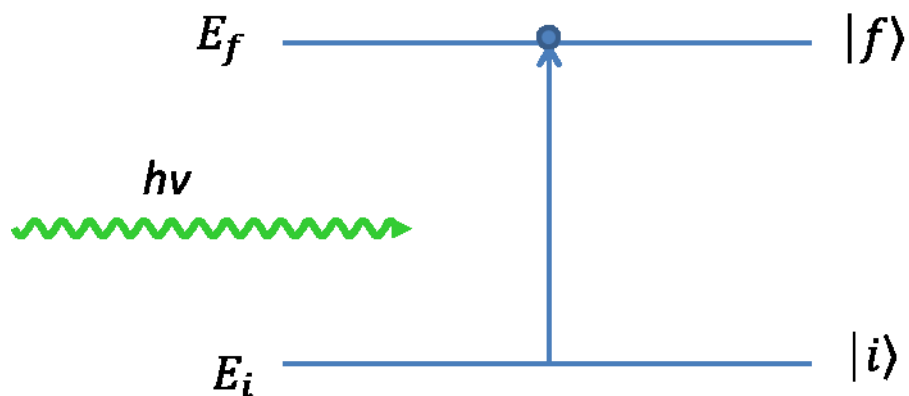


Figure 2.1: Energy level diagram of a two-state system illustrating absorption. E_i is the energy of the system in the state $|i\rangle$ and E_f is the energy of the system in state $|f\rangle$.

Spontaneous Emission

Almost all emissions that we usually encounter are of spontaneous type. Examples are emissions from sodium vapors or tungsten filament. This process is illustrated in Fig. 2.2. In this process, the excited molecule or atom M^* in state $|f\rangle$ spontaneously emits a quantum of energy to reach the ground state $|i\rangle$:



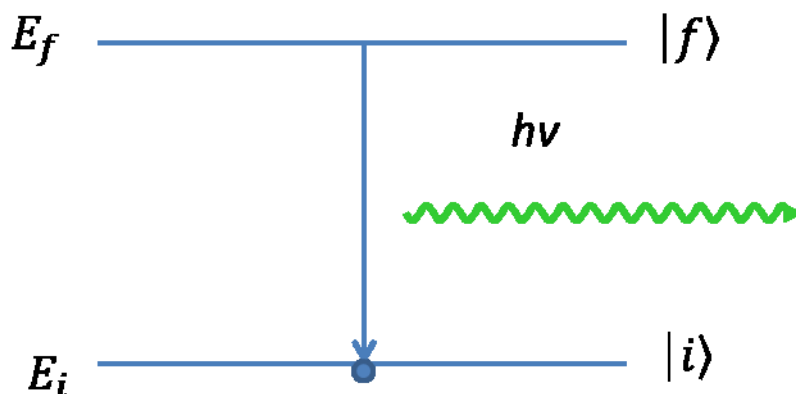
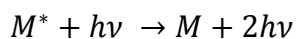


Figure 2.2: Energy level diagram of a two-state system illustrating spontaneous emission. E_i is the energy of the system in the state $|i\rangle$ and E_f is the energy of the system in state $|f\rangle$.

Stimulated Emission

Stimulated emission is a process in which an incident radiation of appropriate frequency triggers an atom in an excited state to emit radiation of the same frequency. The rate of stimulated emission depends on the intensity of external field and also the number of atoms or molecules in the excited state. This process is illustrated in Fig. 2.3. If ν is the frequency of incident radiation required to induce or stimulate M^* to go from excited state $|f\rangle$ to the ground state $|i\rangle$, then this process is represented by:



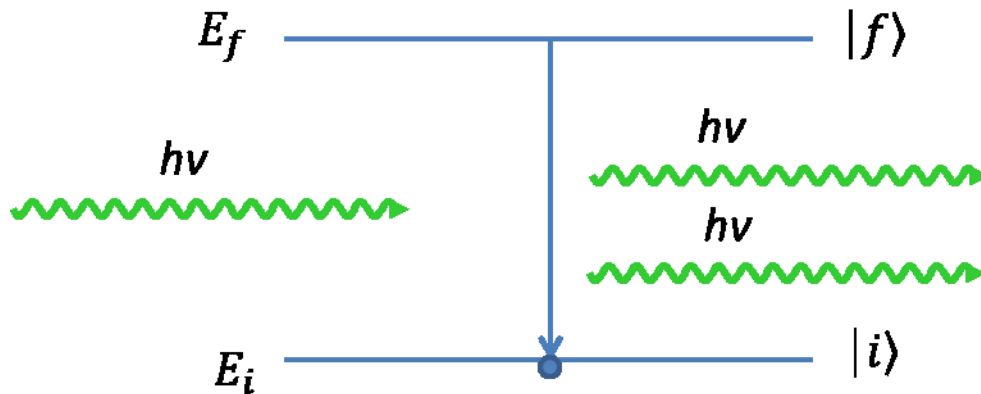


Figure 2.3: Energy level diagram of a two-state system illustrating stimulated emission. E_i is the energy of the system in the state $|i\rangle$ and E_f is the energy of the system in state $|f\rangle$.

2.2.2 Einstein's A and B coefficients

Let us consider an atom or molecule having two states, as shown in Fig. 2.1. The rate of change of population N_f of the excited state $|f\rangle$ due to the absorption is given by:

$$\frac{dN_f}{dt} = N_i B_{if} \rho(\nu), \quad (2.2)$$

where B_{if} is the Einstein coefficient for absorption and $\rho(\nu)$ is the spectral radiation density given by Planck's formula:

$$\rho(\nu) = \frac{8\pi h \mu^2 \nu^3 / c^3}{\exp\left(\frac{h\nu}{k_B T}\right) - 1}. \quad (2.3)$$

In the above expression h is Planck's constant, μ is the refractive index of the medium, c is the speed of light, T is the equilibrium temperature and k_B is the Boltzmann constant.

Similarly, the rate of change of population N_f due to stimulated emission (see Fig. 2.3) is given by:

$$\frac{dN_f}{dt} = -N_f B_{fi} \rho(\nu), \quad (2.4)$$

where B_{fi} is the Einstein coefficient for this process and is equal to B_{if} . For spontaneous emission (see Fig. 2.2), we have:

$$\frac{dN_f}{dt} = -N_f A_{fi}, \quad (2.5)$$

where A_{fi} is Einstein's coefficient for spontaneous emission. If the system is in thermal equilibrium in the presence of radiation of frequency ν , then we have:

$$\frac{dN_f}{dt} = (N_i - N_f) B_{fi} \rho(\nu) - N_f A_{fi} = 0, \quad (2.6)$$

which gives:

$$\left(\frac{N_i}{N_f} - 1 \right)^{-1} = \frac{\rho(\nu) B_{fi}}{A_{fi}}. \quad (2.7)$$

In thermal equilibrium, the number of molecules, N_f , in energy state $|f\rangle$ and the number of molecules, N_i , in energy state $|i\rangle$ are related as:

$$\frac{N_i}{N_f} = \frac{g_i}{g_f} \exp\left(\frac{h\nu}{kT}\right), \quad (2.8)$$

where g_i and g_f are the degeneracies of the states $|i\rangle$ and $|f\rangle$, respectively. If the degeneracies of both the states are equal, then inserting (2.8) in (2.7) and then comparing with (2.3) we get:

$$A_{fi} = \frac{8\pi\mu^2 h\nu^3 B_{fi}}{c^3}. \quad (2.9)$$

This is the relationship between Einstein's A and B coefficients. According to this equation, the spontaneous emission varies as the cube of the frequency relative to the stimulated emission.

2.2.3 Dipole moment

The electric dipole moment of a molecule, denoted by \vec{m} , is defined as:

$$\vec{m} = -e \sum_i \vec{r}_i + e \sum_j Z_j \vec{R}_j, \quad (2.10)$$

where \vec{r}_i 's are the position vectors of electrons, \vec{R}_j 's are the position vectors of nuclei, $-e$ is the charge on each the electron and $+eZ_j$ is the charge on the j^{th} nucleus.

2.2.4 Born-Oppenheimer approximation

Let us consider that the total wave function of the molecule is ψ_{tot} and its electronic and vibrational component wave functions are ψ_{el} and ψ_{vib} . By assuming that (i) the electrons move much faster than the nucleus that the nucleus can be considered to be fixed during electronic motion, and that (ii) the nucleus senses a constant potential because of the speedy motion of the electrons, one can separate the wave function of the molecule into its electronic and nuclear components, i.e.,

$$\psi_{tot} = \psi_{el}\psi_{vib}. \quad (2.11)$$

This is called the *Born-Oppenheimer approximation*.

2.2.5 Transition dipole moment

The transition dipole moment is the electric dipole moment associated to the transition from ground state to the excited state. If $|i\rangle$ denotes the ground state of the molecule and $|f\rangle$ the excited state of the molecule then the transition dipole moment, usually denoted by \vec{m}_{fi} , is defined as:

$$\vec{m}_{fi} = \langle i | \vec{m} | f \rangle. \quad (2.12)$$

Within the Born-Oppenheimer approximation the ground state $|i\rangle$ and the excited state $|f\rangle$ can be written as $|i\rangle = |\phi_i\rangle |v_i\rangle$ and $|f\rangle = |\phi_f\rangle |v_f\rangle$, where $|\phi_i\rangle$ and $|v_i\rangle$ are electronic and vibrational wave functions of the ground states and $|\phi_f\rangle$ and $|v_f\rangle$ are the electronic and vibrational wave functions of the excited state. Thus, from (2.12) we have:

$$\vec{m}_{fi} = \left\langle \phi_i v_i \left| -e \sum_k \vec{r}_k + e \sum_l Z_l \vec{R}_l \right| \phi_f v_f \right\rangle, \quad (2.13)$$

or

$$\vec{m}_{fi} = -e \sum_k \langle \phi_f | \vec{r}_k | \phi_i \rangle \langle v_f | v_i \rangle + e \sum_l Z_l \langle v_i | \vec{R}_l | v_f \rangle \langle \phi_i | \phi_f \rangle. \quad (2.14)$$

Since $\langle \phi_i | \phi_f \rangle = 0$, (2.14) can be written as:

$$\vec{m}_{fi} = -e \sum_k \langle \phi_f | \vec{r}_k | \phi_i \rangle \langle v_f | v_i \rangle. \quad (2.15)$$

2.2.6 Frank-Condon principle

The Frank-Condon principle is a rule that explains the vibronic transitions in spectroscopy and quantum chemistry. Vibronic transitions are transitions that occur

following the absorption or emission of a photon by the molecule and involve simultaneous changes in electronic and vibrational energy levels. The principle states that the time scale for electronic transitions between two states is so fast compared to the nuclear motion that the nucleus can be considered static, and the vibrational transition from one state to another state is more likely to happen if these states have a large overlap. The resulting state is called *Frank-Condon state*. This principle explains why certain peaks are stronger than others in the absorption spectrum of molecules. If we define $S(v_f, v_i) = \langle v_f | v_i \rangle$ and $\vec{m} = -e \sum_k \langle \phi_f | \vec{r}_k | \phi_i \rangle$, then (2.15) can be expressed as:

$$\vec{m}_{fi} = \vec{m} S(v_f, v_i), \quad (2.16)$$

where \vec{m} is the electronic transition dipole moment and $|S(v_f, v_i)|^2$ is the Frank-Condon factor. The Frank-Condon factor is the measure of the degree of overlap between the excited state vibrational wave function and the ground state wave function and varies between 0 and 1. It governs the vibrational transition contribution to the transition probability and has large contribution if the vibrational ground state and excited state have a large overlap (Fig. 2.4).

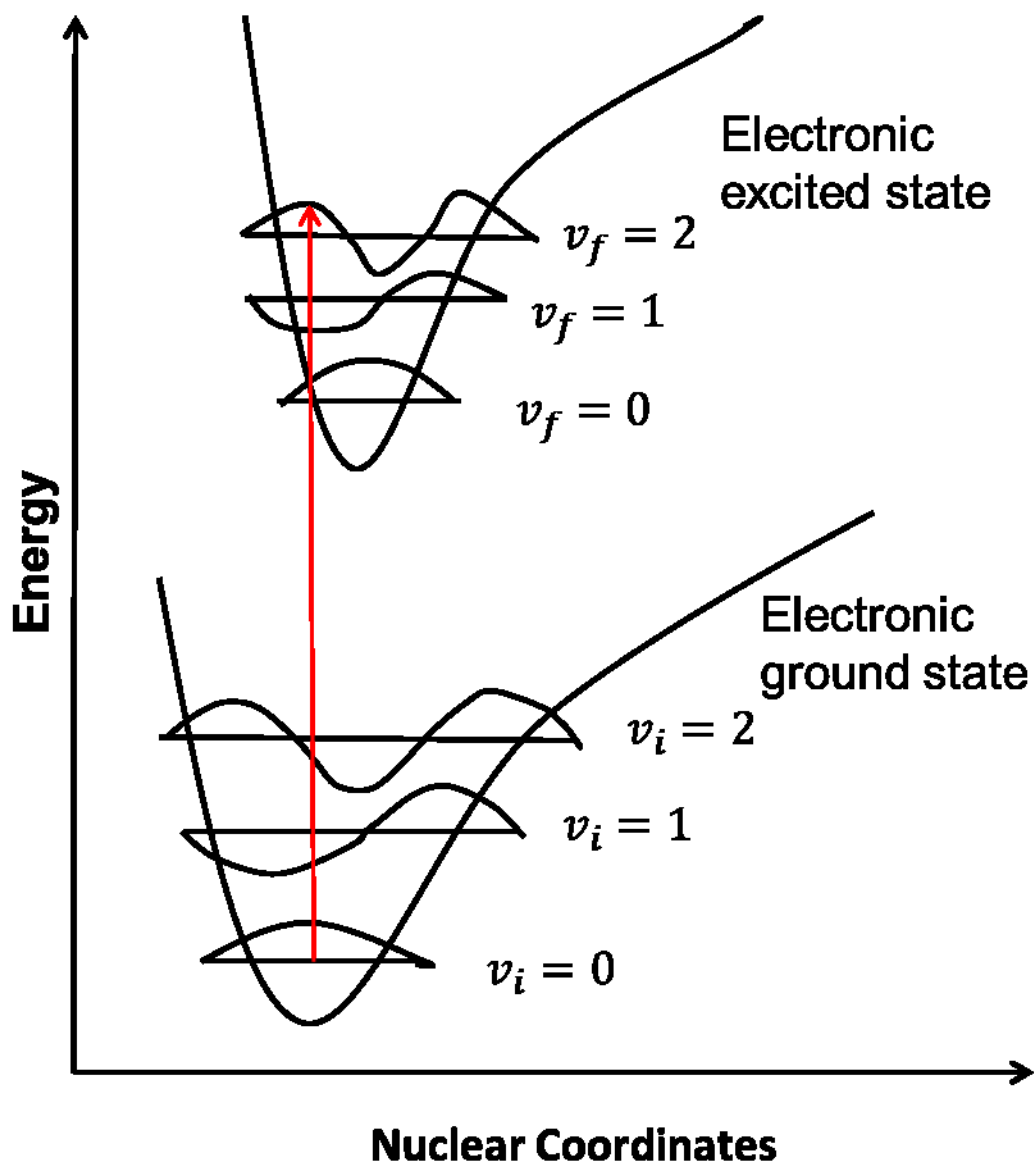


Figure 2.4: Transition of an electron from electronic ground state to electronic excited state. The electronic transitions are fast compared to the nuclear motion and hence the nucleus can be regarded as at rest during transition. The transition between vibrational levels $v_i = 0$ and $v_f = 2$ is favored because of large overlap of vibrational wave functions.

2.2.7 Relation between the Einstein coefficients and the transition dipole moment

The average power radiated by a classical oscillating dipole is given by (10):

$$P_r = \frac{\omega^4 \mu m_{cl}^2}{3 c^3}, \quad (2.17)$$

where ω is the angular frequency of the oscillating dipole, μ is the refractive index of the medium, m_{cl} is the classical dipole moment and is equal to the product of charge q and the distance between two charges r making the dipole, and c is the speed of light.

From (2.17), it is clear that the power radiated by the classical oscillator is same for $\pm\omega$, which reflects the time-reversal symmetry between absorption and emission. For a quantum mechanical oscillator, there are separate matrix elements for emission and absorption. Hence, the quantum mechanical (transition) dipole moment can be written as:

$$m_{qm} = |qr| = \langle f|qr|i\rangle + \langle i|qr|f\rangle, \quad (2.18)$$

where $|i\rangle$ and $|f\rangle$ represent the initial and excited states of the oscillators. Denoting $m_{fi} = \langle f|qr|i\rangle$ and $m_{if} = \langle i|qr|f\rangle$, (2.18) can also be expressed as:

$$\begin{aligned} m_{qm} &= m_{fi} + m_{if} = m_{fi} + m_{fi}^* \\ &= 2 \operatorname{Re}[m_{fi}], \end{aligned} \quad (2.19)$$

where m_{fi}^* is the complex conjugate of m_{fi} . Again writing $m_{fi} = |m_{fi}| \exp(i\phi)$, where

$$\phi = \tan^{-1} \frac{\operatorname{Im}[m_{fi}]}{\operatorname{Re}[m_{fi}]}, \quad (2.19) \text{ becomes:}$$

$$m_{qm} = 2|m_{fi}|. \quad (2.20)$$

By replacing m_{cl} in (2.17) with m_{qm} given by (2.20), we obtain:

$$P_r = \frac{4\omega^4 \mu |m_{fi}|^2}{3 c^3}. \quad (2.21)$$

The power radiated by an oscillator is the rate of energy it emits during spontaneous transition, and it can be written in terms of Einstein's A coefficient as:

$$P_r = \hbar\omega A_{fi} = 2\pi\hbar\nu A_{fi}, \quad (2.22)$$

where ν is the frequency of the oscillator. Substitution of (2.22) into (2.21) gives

$$A_{fi} = \frac{2^5\mu\pi^3\nu^3|m_{fi}|^2}{3c^3\hbar}. \quad (2.23)$$

Further, substitution of (2.23) into (2.9) yields:

$$B_{fi} = \frac{2\pi|m_{fi}|^2}{3\hbar^2\mu}. \quad (2.24)$$

2.2.8 Fluorescence emission spectrum of the molecules

If $f(\nu)$ is the fluorescence spectrum such that $\int f(\nu)d\nu = 1$ and $g(E_f)$ is the Boltzmann factor for the excited state $|f\rangle$ of the molecule in thermal equilibrium, then (2.23), in conjunction with (2.16), can be generalized as:

$$A_{fi} = \frac{1}{\tau_f} = \frac{\int f(\nu)d\nu}{\tau_f} = \int d\nu \frac{2^5\mu\pi^3\nu^3m^2}{3c^3\hbar} \int g(E_f) S_f^2(E_f, E_f - h\nu) dE_f, \quad (2.25)$$

where S_f^2 is the Franck-Condon factor associated with the fluorescence of the molecule and τ_f is the fluorescence lifetime of the donor, which is equal to the inverse of radiative de-excitation (spontaneous emission) rate, as described in chapter 1. From (2.25), the fluorescence spectrum $f(\nu)$ can be written as:

$$f(\nu) = \frac{2^5\mu\tau_f\pi^3\nu^3m^2}{3c^3\hbar} \int g(E_f) S_f^2(E_f, E_f - h\nu) dE_f. \quad (2.26)$$

2.2.9 Beer-Lambert law and the extinction coefficient

We consider a slab of solution as shown in Fig. 2.5 having thickness d that contains n light absorbing molecules/cm³. Let the absorption cross-section of molecules be σ (in units of cm²). Let I_0 be the intensity of light falling on the sample and I is the intensity of light coming out of the sample. The light intensity absorbed per unit thickness is proportional to the intensity of the incident light, I , absorption cross section, σ , and the number density of light-absorbing molecules (i.e., molecules per cm³), n . Thus, we have:

$$\frac{dI}{dx} = -I\sigma n. \quad (2.27)$$

Integration of (2.27) with boundary condition $I = I_0$ at $x = 0$ yields:

$$\ln\left(\frac{I_0}{I}\right) = \sigma nd, \quad (2.28)$$

where d is the thickness of the sample.

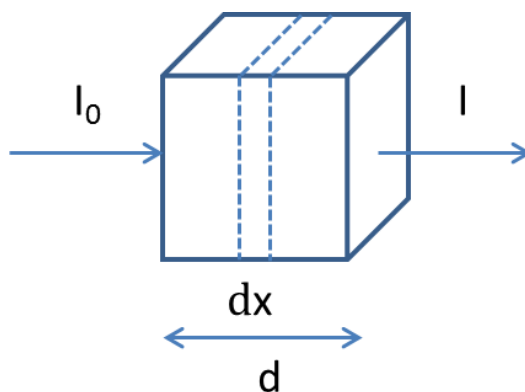


Figure 2.5: Illustration of absorption of light by a slab of solution of fluorescent molecules of thickness d . I_0 is the intensity of incident light on the slab and I is the intensity of light after passing through the slab. This figure is adapted from (11).

Equation (2.28) is called the Beer-Lambert equation. In literature, the following alternative form is often used:

$$\log\left(\frac{I_0}{I}\right) = \varepsilon Cd = \text{optical density}, \quad (2.29)$$

where ε is the decadic molar extinction coefficient (in $\text{M}^{-1}\text{cm}^{-1}$) and C is concentration of solution in moles/liter. From (2.28) and (2.29), we get:

$$\varepsilon = \frac{\sigma n}{\ln(10)C}. \quad (2.30)$$

Since, n is related to Avogadro number, N_A , as $n = N_A C / 10^3$, substitution of n in (2.30) gives:

$$\varepsilon = \frac{\sigma N_A}{1000 \ln(10)}. \quad (2.31)$$

This is the relation between the extinction coefficient and the absorption cross-section.

2.2.10 Absorption spectrum of molecules

The absorption cross-section is related to Einstein's B coefficient through the following relation (12):

$$\sigma = \frac{2\pi\hbar\nu B_{fi}}{c}. \quad (2.32)$$

Combination of (2.31), (2.32) and (2.24) gives:

$$\varepsilon = \frac{2^2\pi^2\nu |m_{fi}|^2 N_A}{3000 \ln(10) \mu \hbar c}. \quad (2.33)$$

If $\varepsilon(\nu)$ is the absorption spectrum and $g(E_i)$ is the Boltzmann factor associated with the ground state of the molecule in thermal equilibrium, then (2.33), in conjunction with (2.16), can be written as:

$$\int \varepsilon(\nu) d\nu = \int d\nu \frac{2^2 \pi^2 \nu m^2 N_A}{3000 \ln(10) \hbar \mu c} \int g(E_i) S_i^2(E_i, E_i + h\nu) dE_i, \quad (2.34)$$

where S_i^2 is the Franck-Condon factor associated with excitation of the molecule. From (2.34), the absorption spectrum $\varepsilon(\nu)$ can be written as:

$$\varepsilon(\nu) = \frac{2^2 \pi^2 \nu m^2 N_A}{3000 \ln(10) \hbar \mu c} \int g(E_i) S_i^2(E_i, E_i + h\nu) dE_i. \quad (2.35)$$

2.3 Classical derivation of energy transfer rate

2.3.1 Perrin's theory of energy transfer rate

A first simple classical model to explain the energy transfer between the molecules in solutions was developed by J. Perrin. He considered two classical electrically charged oscillators interacting with each other through columbic electrostatic force. If the two oscillators have the same resonance frequency they will exchange energy as two resonating pendulums do. He assumed that initially only one of the oscillators, the “donor,” is vibrating and another oscillator, the “acceptor” is at rest. If R is the distance between the two oscillators, \vec{m}_D is the classical dipole moment of the donor, \vec{m}_A is the classical dipole moment of the acceptor, and μ is the refractive index of the medium where the oscillators are placed, then the interaction energy of the oscillators is given by:

$$E_{int} = \frac{[(\vec{m}_D \cdot \vec{m}_A) - \frac{3}{R^2} (\vec{m}_D \cdot \vec{R})(\vec{m}_A \cdot \vec{R})]}{\mu^2 R^3}. \quad (2.36)$$

J. Perrin assumed that the donor and acceptor dipoles are identical, hence one can write (2.36) as:

$$E_{int} = \frac{\kappa m^2}{\mu^2 R^3}, \quad (2.37)$$

where κ is the orientation factor arising due to dipoles and given by:

$$\kappa = [\hat{m}_D \cdot \hat{m}_A - 3(\hat{m}_D \cdot \hat{R})(\hat{m}_A \cdot \hat{R})]. \quad (2.38)$$

The hats on dipole moments and the distance between the donor and acceptor represent their directions in space with unit magnitude. In his original calculations, Perrin did not include κ and μ^2 , because these were approximate calculations. However, these factors are included here for completeness (1). Using Planck's old quantum theory, (2.37) can be written as:

$$E_{int} = \frac{\kappa m^2}{\mu^2 R^3} = \hbar \omega \sim \frac{\hbar}{\tau_{int}}, \quad (2.39)$$

where \hbar is the Planck's constant, h , divided by 2π , ω is the angular frequency of the donor oscillator, τ_{int} is the time period of the oscillating donor. The simplification of (2.39) yields:

$$\tau_{int} = \frac{\hbar \mu^2 R^3}{\kappa m^2}. \quad (2.40)$$

In other words, the rate of energy transfer, Γ^{D-A} , is given by:

$$\Gamma^{D-A} = \frac{\kappa m^2}{\hbar \mu^2 R^3}. \quad (2.41)$$

This expression is called the *Perrin's formula* of energy transfer from oscillating donor to acceptor at rest.

Also, from the average power radiated by an oscillating dipole, P_r , as given by (2.17), the time of radiation can be calculated as:

$$\tau_{rad} = \frac{\hbar\omega}{P_r}. \quad (2.42)$$

Substitution of (2.17) in (2.42) yields:

$$\tau_{rad} = \frac{3\hbar c^3}{m^2 \mu \omega^3}. \quad (2.43)$$

Now we find the distance R_0 where the natural decay time of the oscillator is equal to the time of energy transfer, $\tau_{rad} = \tau_{int}$ (1, 13). This gives:

$$R_0^3 = \frac{3\kappa c^3}{\mu \omega^3} = \frac{3\kappa}{(2\pi)^3 \mu} \lambda^3 \approx 0.01 \lambda^3, \quad (2.44)$$

or $R_0 \approx 0.2\lambda$, where $\lambda = c/\nu$ is the wavelength of the donor oscillations. Thus, according to this model, the energy transfer would take place over a distance approximately 1/5 of the wavelength of light radiating from the dipole. For a molecule that absorbs in the visible spectrum at around 6000 Å, a $R_0 = 1200$ Å is thus obtained, when the concentration of solution of the molecule was 10^{-6} mole/liter.

Experimentally the observed value of the distance over which energy transfer occurred was much smaller than the estimated value. As seen from (2.41), the $1/R^3$

dependence of energy transfer rate that leads to such a large value of R_0 , is *the assumption of exact resonance*.

2.3.2 Förster's correction in Perrin's theory of energy transfer rate

Förster was able to correct the discrepancy of the Perrins' model of energy transfer between the identical molecules in solution by taking into account the Stokes shift of the fluorescence spectrum relative to the absorption spectrum and by considering the broad spectra of donors and acceptors rather than assuming the line spectrum. He pointed out that the large estimate of R_0 is due to the fact that the conditions of the exact resonance are not fulfilled. The spectrum of a dye molecule is not a sharp line, but rather a broad band. The spectra are usually broadened by intermolecular and solvent interactions. Therefore, the resonance is perturbed by the fact that the emission spectrum of the excited molecule is different from the absorption spectrum of the unexcited molecule. The resonance can occur for any frequency distributed over the total overlapping frequency spectra of the donor and acceptor (see Fig. 2.6), and this drastically lowers the probability that the resonance condition will be met. Because of the width of donor and acceptor spectra, the energy that an excited donor donates to a neighboring unexcited acceptor molecule will exactly match with the energy that the acceptor molecule gains only in a small fraction of the time, i.e., only a fraction of molecules are in resonance at any time.

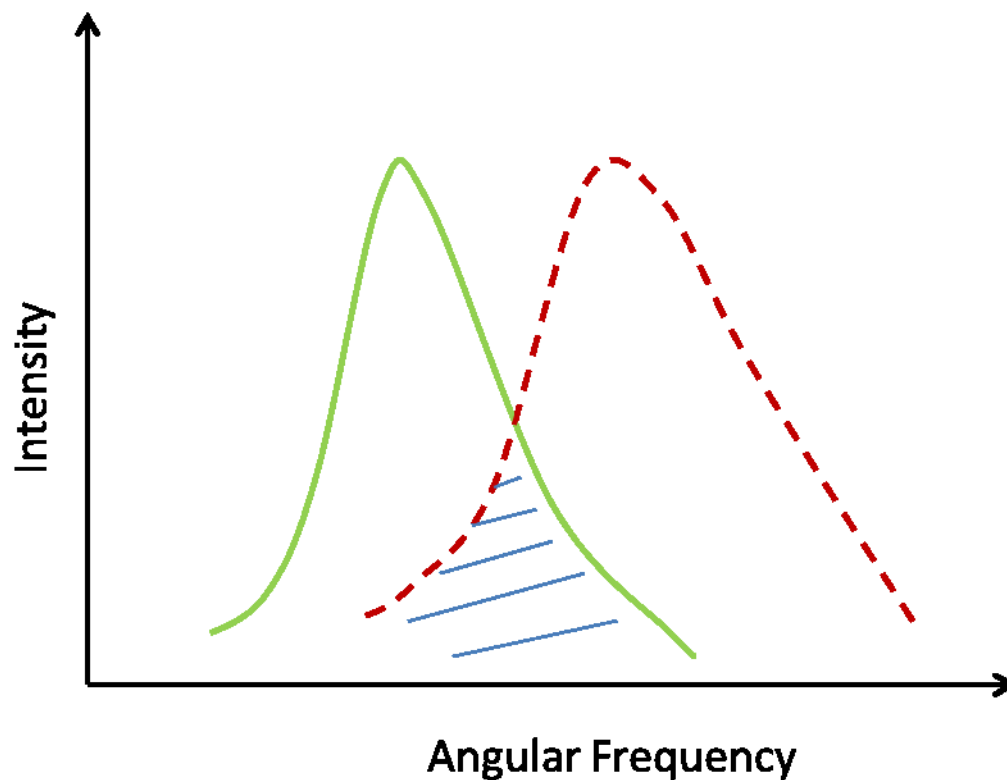


Figure 2.6: The emission spectrum of the donor (solid line) and the absorption spectrum of the acceptor (dashed line). The shaded area shows the overlap between the donor emission and acceptor absorption spectrum where the donor and acceptor oscillators can be in resonance.

The condition of resonance is fulfilled only for the short periods when the frequencies of both molecules agree within the coupling width, i.e. a frequency range with a width of $\frac{E_{int}}{\hbar}$. Let us consider the fluorescence and absorption spectra to be two rectangles with a width Ω and the overlap strip width Ω' as shown in Fig. 2.7.

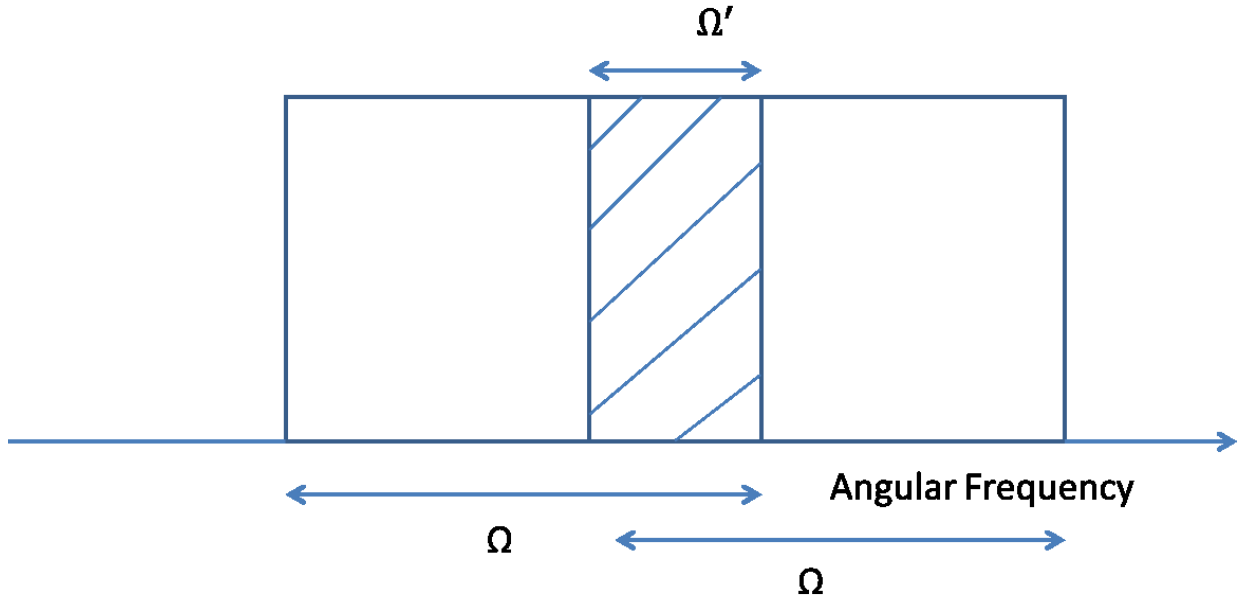


Figure 2.7: The emission spectrum of the donor and the absorption spectrum of the acceptor are shown as the rectangle of width Ω . The shaded area shows the overlap between the donor emission and acceptor absorption spectrum where the donor and acceptor oscillators are in resonance having width Ω' .

For the resonance condition to be met, if the frequency of one oscillator is within Ω' , then at the same time the frequency of another oscillator should coincide with it within $\frac{E_{int}}{\hbar}$. The probability for this is $w = \frac{\Omega'}{\Omega} \frac{1}{\tau_{int}}$. Hence the new rate of energy transfer

becomes:

$$\Gamma_{D \rightarrow A} = \frac{1}{\tau'_{int}} = \frac{w}{\tau_{int}}, \quad (2.45)$$

or

$$\Gamma_{D \rightarrow A} = \frac{m_{cl}^4 k^2 \Omega'}{\hbar^2 \mu^4 R^6 \Omega^2}. \quad (2.46)$$

As seen from (2.46), in contrast to the earlier derivation of Perrin (2) as described in the previous section, the energy transfer rate varies as $1/R^6$, the hallmark of FRET.

Equating $\tau_{rad} = \tau'_{int}$, Förster calculated:

$$R_0^6 = 3 \left(\frac{c^3}{\omega^3} \right) m_{cl}^2 k^2 \left(\frac{\Omega'}{\Omega^2} \right) \left(\frac{1}{\hbar \mu^3} \right). \quad (2.47)$$

Eliminating m_{cl}^2 in (2.43) using (2.36) and replacing c by $\lambda\omega/2\pi$, we get:

$$R_0^6 = 9 \left(\frac{\lambda}{2\pi} \right)^6 \left(\frac{k^2}{\mu^4} \right) \left(\frac{\Omega'}{\Omega^2} \right) \left(\frac{1}{\tau_{rad}} \right). \quad (2.48)$$

For the type of fluorophores considered here, Ω is $\sim 1.5 \times 10^{14} \text{ sec}^{-1}$ for $\lambda = 6000 \text{ \AA}$. The ratio $\frac{\Omega'}{\Omega}$ which represents spectral overlap is 1/10 for normal temperatures. Using these numbers and $\tau_{rad} = 0.5 \times 10^{-8} \text{ sec}$ (14), R_0 can be estimated around 75 \AA , the correct order of magnitude for the critical distance. This is only the rough estimate of Förster distance based on classical physics. The detailed quantum mechanical derivation of energy transfer is given in the next section.

2.4 Quantum mechanical treatment of excitation transfer

We consider two molecules, D and A, of either the same or different type. Molecule D, which we call the “donor,” is in an excited state and molecule A, which we call an “acceptor,” is in an unexcited state at the beginning. The total vibronic energies of the molecules are E'_D and E_A respectively. We follow the time evolution of all situations in which molecule A is in the excited state with its total vibronic energy E'_A , and D is in the unexcited state with its total vibronic energy E_D . Using $\psi(q, Q, E)$ as molecular vibronic

wave functions, which are functions of their respective electronic and nuclear coordinates q and Q and their corresponding energies, such a process can be described as:

$$\psi'_D(E'_D)\psi_A(E_A) \rightarrow \psi_D(E_D)\psi'_A(E'_A),$$

or, in a short notation by the use of dimer vibronic wave functions as:

$$\Psi_{D'A}(E'_D, E_A) \rightarrow \Psi_{DA'}(E_D, E'_A).$$

The Hamiltonian of the system is given by:

$$\mathcal{H} = \mathcal{H}_D + \mathcal{H}_A + E_{int}, \quad (2.49)$$

where \mathcal{H}_D and \mathcal{H}_A are the unperturbed Hamiltonians of donor and acceptor molecules respectively and E_{int} is the interaction energy between the two molecules and is given by equation (2.36). This interaction energy is also called resonance interaction energy.

From time-dependent perturbation theory, the transition probability for the transition from the ground state $|i\rangle$ to the excited state $|f\rangle$ for a constant perturbation turned on at $t=0$:

$$V(t) = \begin{cases} 0, & t < 0 \\ V, & t \geq 0 \end{cases} \quad (2.50)$$

is given by (15):

$$P(i \rightarrow f) \simeq \frac{4|V_{fi}|^2}{|E_f - E_i|^2} \sin^2 \left[\frac{(E_f - E_i)t}{2\hbar} \right]. \quad (2.51)$$

In expression (2.51), E_f is the energy of the excited state $|f\rangle$, E_i is the energy of the ground state $|i\rangle$, and $V_{fi} = \langle f|V|i\rangle$.

Defining the ground state $|i\rangle$ as $\Psi_{D'A}(E'_D, E_A)$, the excited state $|f\rangle$ as $\Psi_{DA'}(E_D, E'_A)$, $E_i = E'_D + E_A$ and $E_f = E_D + E'_A$, the transition probability independent of the excited state vibronic energies can be written as:

$$P(D'A \rightarrow DA') \simeq \iint \frac{4u^2(E_D, E'_A)}{(\Delta E)^2} \sin^2 \left[\frac{\Delta E t}{2\hbar} \right] dE_D dE'_A, \quad (2.52)$$

where

$$\Delta E = E'_a + E_b - E_a - E'_b, \quad (2.53)$$

and

$$V_{fi} = \langle f|V|i\rangle = \langle \Psi_{D'A}(E'_D, E_A) | E_{int} | \Psi_{DA'}(E_D, E'_A) \rangle = u(E_D, E'_A). \quad (2.54)$$

The integral in (2.52) extends over the excited state energies E_D and E'_A .

2.4.1 Strong coupling

Expression (2.52) is valid as long as $P(D'A \rightarrow DA') \ll 1$. For sufficiently short times, such that:

$$\frac{\Delta E t}{2\hbar} \ll 1, \quad (2.55)$$

expression (2.55) becomes:

$$P(D'A \rightarrow DA') \simeq \frac{t^2}{\hbar^2} \iint u^2(E_D, E'_A) dE_D dE'_A. \quad (2.56)$$

If the condition (2.55) is satisfied for all energy values within the total energy ranges Δw and $\Delta w'$ of the electronic transitions, the integration in (2.56) can be performed over these ranges and we get:

$$P(D'A \rightarrow DA') \simeq \frac{t^2 U^2}{\hbar^2}, \quad (2.57)$$

where $U^2 = \iint u^2(E_D, E'_A) dE_D dE'_A$. If we require that transfer occurs under the conditions such that $P(D'A \rightarrow DA')$ reaches unity, we have $|U| \sim \frac{\hbar}{t}$ for times within the limit of (2.55) which are $t \ll \frac{2\hbar}{\Delta E} \sim \frac{2\hbar}{\Delta w}$.

This leads to:

$$2|U| \gg \Delta w, \quad (2.58)$$

as an approximate condition for strong coupling transfer.

2.4.2 Weak coupling

When the molecules have well defined vibronic levels, (2.55) can be used for even longer intervals provided the integration is restricted to $\Delta \epsilon_v$ and $\Delta \epsilon_w$ of E_D and E'_A , which correspond to the vibrational levels v and w , respectively, of the original state of the system. Under these conditions (2.53) becomes:

$$P(D'A \rightarrow DA') \simeq \frac{t^2 u_{vw}^2}{\hbar^2}, \quad (2.59)$$

where u_{vw} is the vibronic matrix element of resonance interaction. As in the case of strong coupling, the condition for weak coupling is:

$$2|u_{vw}| \gg \Delta\epsilon, \quad (2.60)$$

where $\Delta\epsilon$ is the vibronic band width.

2.4.3 Very weak coupling

If condition (2.60) is not met, i.e., the matrix element of resonance interaction matrix is smaller than the vibronic bandwidth, we enter the region of very weak coupling. Now, (2.49) becomes:

$$P(D'A \rightarrow DA') \simeq \lim_{t \rightarrow \infty} \iint \frac{4u^2(E_D, E'_A)}{(\Delta E)^2} \sin^2 \left[\frac{\Delta E t}{2\hbar} \right] dE_D dE'_A, \quad (2.61)$$

or

$$P(D'A \rightarrow DA') = \frac{\pi t}{\hbar^2} \iint u^2(E_D, E'_A) \lim_{t \rightarrow \infty} \frac{\sin^2 \left[\frac{\Delta E t}{2\hbar} \right]^2}{\pi \left(\frac{\Delta E}{2\hbar} \right)^2 t} dE_D dE'_A. \quad (2.62)$$

Using the definition of the delta function,

$$\delta(x) = \lim_{t \rightarrow \infty} \frac{\sin^2 tx}{\pi t x^2}, \quad (2.63)$$

we can write (2.62) as:

$$P(D'A \rightarrow DA') = \frac{\pi t}{\hbar^2} \iint u^2(E_D, E'_A) \delta \left(\frac{\Delta E}{2\hbar} \right) dE_D dE'_A \quad (2.64)$$

or

$$P(D'A \rightarrow DA') = \frac{2\pi t}{\hbar} \iint u^2(E_D, E'_A) \delta(\Delta E) dE_D dE'_A. \quad (2.65)$$

Using the notation $E = \frac{1}{2} (E'_D - E_D + E'_A - E_A)$, we have:

$$\begin{aligned} dE_D dE'_A &= \frac{\partial (E, \Delta E)}{\partial (E_D, E'_A)} dE d(\Delta E) = \begin{vmatrix} \frac{\partial E}{\partial E_D} & \frac{\partial (\Delta E)}{\partial E_A} \\ \frac{\partial E}{\partial E} & \frac{\partial (\Delta E)}{\partial (\Delta E)} \end{vmatrix} dE d(\Delta E) \\ &= \begin{vmatrix} \frac{1}{2} & -1 \\ \frac{1}{2} & -1 \end{vmatrix} dE d(\Delta E) = dE d(\Delta E). \end{aligned} \quad (2.66)$$

Writing (2.64) in terms of new variables in conjunction with (2.66), we get:

$$P(D'A \rightarrow DA') = \frac{2\pi t}{\hbar} \iint u^2(E, \Delta E) \delta(\Delta E) dE d(\Delta E), \quad (2.67)$$

or

$$P(D'A \rightarrow DA') = \frac{2\pi t}{\hbar} \int u^2(E, 0) dE \quad (2.68)$$

The above equation gives the probability for excitation transfer from excited donor molecule to unexcited acceptor molecule for the times longer than those required for very weak coupling transfer.

From (2.68), the transition rate can be calculated as:

$$\Gamma_{D \rightarrow A} = \frac{2\pi}{\hbar} \int u^2(E, 0) dE. \quad (2.69)$$

2.5 Quantum mechanical derivation of Förster energy transfer rate

To calculate the transfer rate when the coupling between the donor and acceptor dipoles is very weak, we have to specify the matrix element $u(E, 0)$ appearing in (2.69) further.

In the complete notation, $u(E, 0)$ can be written as (see the previous section):

$$u(E, 0) = u(E'_D, E_A; E_D, E'_A) = u(E'_D, E_A; E'_D - E, E_A + E). \quad (2.70)$$

Here, the excited state energies have been expressed by the original state energies and the transfer energy E . Under Born-Oppenheimer approximation, the vibronic wave-functions can be written as:

$$\Psi_{D'A}(E'_D, E_A) = \phi'_D \phi_A \chi'_D(E'_D) \chi_A(E_A), \quad (2.71a)$$

$$\Psi_{DA'}(E_D, E'_A) = \phi_D \phi'_A \chi_D(E_D - E) \chi'_A(E_A + E), \quad (2.71b)$$

where χ'_l and χ_l are the vibrational wave functions and ϕ'_l and ϕ_l are electronic wave functions of the excited and of the unexcited molecule, l , respectively. From (2.70), $u^2(E, 0)$ can be written as:

$$u^2(E, 0) = \langle \Psi_{D'A}(E'_D, E_A) | E_{int} | \Psi_{DA'}(E_D, E'_A) \rangle^2, \quad (2.72)$$

$$= \langle \phi'_D \phi_A | E_{int} | \phi_D \phi'_A \rangle^2 S_D^2(E'_D, E'_D - E) S_A^2(E_A, E_A + E), \quad (2.73)$$

$$= W^2 S_D^2(E'_D, E'_D - E) S_A^2(E_A, E_A + E), \quad (2.74)$$

where $W = \langle \phi'_D \phi_A | E_{int} | \phi_D \phi'_A \rangle$ is electronic interaction matrix element and:

$$S(E_1, E_2) = \langle \chi'(E_1) | \chi(E_2) \rangle, \quad (2.75)$$

a vibrational overlap integral. Substituting (2.36) in the expression of W , we have:

$$W^2 = \frac{\kappa^2 |m_D|^2 |m_A|^2}{\mu^4 R^6}, \quad (2.76)$$

where κ is the orientation factor of dipoles as given in (2.38), m_D, m_A are the transitional dipole moments of donor and acceptor molecules. Substituting (2.76) in (2.74) and then into (2.69) and replacing the transfer energy by the transfer frequency, $\nu = E/2\pi\hbar$, we arrive at:

$$\Gamma_{D \rightarrow A} = \frac{\kappa^2}{\mu^4 R^6 \hbar^2} \int m_D^2 S_D^2(E'_D, E'_D - E) m_A^2 S_A^2(E_A, E_A + E) d\nu. \quad (2.77)$$

This is the expression for energy transfer rate from an excited donor molecule D having energy E'_D to unexcited acceptor molecule A with energy E_A . If the molecules are in thermal equilibrium, the total energy transfer rate can be obtained by introducing suitable Boltzmann factors and subsequent integration over all energies E'_D and E_A . If $g'(E'_D)$ and $g(E_A)$ denote the continuous Boltzmann factors for excited and non-excited molecule, which are normalized on energy scale then the total transfer rate is given by:

$$\Gamma_{D \rightarrow A} = \frac{\kappa^2}{\mu^4 R^6 \hbar^2} \int \left[m_D^2 \int g(E'_D) S_D^2(E'_D, E'_D - E) dE'_D \right] \cdot \left[m_A^2 \int g(E_A) S_A^2(E_A, E_A + h\nu) dE_A \right] d\nu. \quad (2.78)$$

Recognizing E_f in (2.26) as E'_D , E_i in (2.35) as E_A and then substituting these equations in (2.78) we get:

$$\Gamma_{D \rightarrow A} = \frac{9000 \kappa^2 (\ln 10) c^4}{128 \pi^5 \mu^4 N_A \tau_f R^6} \int f_D(\nu) \epsilon_A(\nu) \frac{d\nu}{\nu^4}. \quad (2.79)$$

Now, let us define:

$$J = \int f_D(\nu) \epsilon_A(\nu) \frac{d\nu}{\nu^4}. \quad (2.80)$$

The above integral is called *spectral overlap integral* and is the measure of spectral overlap between donor emission spectrum and acceptor excitation spectrum.

Combination of (2.79) and (2.80) gives:

$$\Gamma_{D \rightarrow A} = \frac{9000 \kappa^2 (\ln 10) c^4 J}{128 \pi^5 \mu^4 N_A \tau_f R^6}. \quad (2.81)$$

In the above expression, τ_f is the fluorescence lifetime of the donor. We need to express the fluorescence lifetime of the donor in terms of experimentally measurable quantities, the quantum yield Q^D and the lifetime of the donor τ_D . The quantum yield of the donor is defined as the number of photons emitted over the number of photons absorbed by the donor. Mathematically, it can be expressed as:

$$Q^D = \frac{\Gamma^{r,D}}{\Gamma^{r,D} + \Gamma^{nr,D}}, \quad (2.82)$$

where $\Gamma^{r,D}$ and $\Gamma^{nr,D}$ are the rate constants of de-excitation through radiative and non-radiative pathways, as described in Fig. 1.2, chapter 1. The lifetime of the excited state is defined as the average time the molecule spends in the excited state prior to return to ground state. The lifetime of donor in terms of de-excitation rates is defined as:

$$\tau_D = \frac{1}{\Gamma^{r,D} + \Gamma^{nr,D}}. \quad (2.83)$$

As discussed in chapter 1, the lifetime of the donor in the absence of non-radiative process is called the *natural or intrinsic or fluorescence lifetime* and is related to Einstein

A coefficient and is defined as:

$$\tau_f = \frac{1}{\Gamma^{r,D}}. \quad (2.84)$$

Combining (2.82), (2.83) and (2.84) we get:

$$\frac{1}{\tau_f} = \frac{Q^D}{\tau_D}. \quad (2.85)$$

Substituting (2.85) into (2.81), the rate of energy transfer becomes

$$\Gamma_{D \rightarrow A} = \frac{9000\kappa^2 Q^D (\ln 10) c^4 J}{128 \pi^5 \mu^4 N_A \tau_D R^6}. \quad (2.86)$$

Again, if we define

$$R_0^6 = \frac{9000\kappa^2 Q^D (\ln 10) c^4 J}{128 \pi^5 \mu^4 N_A}, \quad (2.87)$$

then the energy transfer rate from donor to acceptor can be expressed as:

$$\Gamma_{D \rightarrow A} = \frac{1}{\tau_D} \left(\frac{R_0}{R} \right)^6, \quad (2.88)$$

where, R_0 is the Förster radius. This expression is also called *Förster energy transfer rate*.

2.6 Determination of stoichiometry and quaternary structure of interacting molecules using spectral FRET

2.6.1 Elementary theory of fluorescence resonance energy transfer

Let us consider two molecules, a donor (D) and an acceptor (A). Both molecules are fluorescent and very close to each other, i.e., within less than 10nm. Let the donor molecule be excited by excitation wavelength λ_{ex} . The excited donor molecule can be de-excited radiatively, non-radiatively or through FRET. Once, the acceptor gets excited through FRET, it emits fluorescence light. The pathways of energy transfer from donor to

acceptor are depicted in Fig. 1.2 of Chapter 1. We defined the quantum yield of the donor in the previous section in (2.82). Similarly we can define the quantum yield of acceptors in terms of photon emission following excitation as (16, 17):

$$Q^A = \frac{\Gamma^{r,A}}{\Gamma^{r,A} + \Gamma^{nr,A}}, \quad (2.89)$$

where $\Gamma^{r,A}$ and $\Gamma^{nr,A}$ are the radiative and non-radiative rate constants for de-excitations of donors and acceptors, respectively. Since FRET opens an additional de-excitation pathway of the donor, the quantum yield of donor in the presence of acceptor can be written as (16, 17):

$$Q^{DA} = \frac{\Gamma^{r,D}}{\Gamma^{r,D} + \Gamma^{nr,D} + \Gamma^{FRET}}. \quad (2.90)$$

We defined the lifetime of the donor in the previous section in (2.83). Similarly, the lifetimes of the acceptor excited state can be defined as the previous (16, 17):

$$\tau_A = (\Gamma^{r,A} + \Gamma^{nr,A})^{-1}. \quad (2.91)$$

In the presence of an acceptor, the new fluorescence lifetime of donor becomes (16, 17):

$$\tau_{DA} = (\Gamma^{r,D} + \Gamma^{nr,D} + \Gamma^{FRET})^{-1}. \quad (2.92)$$

The efficiency of energy transfer (or FRET efficiency) is defined as the fraction of photons dissipated by the excited donor through FRET and is denoted by E . Mathematically, it can be expressed as:

$$E = \frac{\Gamma^{FRET}}{\Gamma^{r,D} + \Gamma^{nr,D} + \Gamma^{FRET}}. \quad (2.93)$$

Combinations of (2.83), (2.92), and (2.93) yields:

$$E = 1 - \frac{\tau_{DA}}{\tau_D}, \quad (2.94)$$

which relates the FRET efficiency to the fluorescence lifetimes of the donor in the presence and absence of acceptor. This provides a convenient means for measuring the FRET efficiency from fluorescence life-time measurements (11, 18, 19). Recognizing $\Gamma_{D \rightarrow A}$ as Γ^{FRET} and using (2.83), (2.88) can be written as:

$$\Gamma^{FRET} = (\Gamma^{r,D} + \Gamma^{nr,D})^{-1} \left(\frac{R_0}{R} \right)^6. \quad (2.95)$$

Using (2.95), (2.93) can be arranged as:

$$E = \frac{\left(\frac{R_0}{R} \right)^6}{1 + \left(\frac{R_0}{R} \right)^6}, \quad (2.96)$$

which connects the FRET efficiency to the distance between donor and acceptor. If the FRET efficiency is known from the lifetime measurements and R_0 is known for the given pair of fluorophores, the distance between the donor and an acceptor can be calculated.

For a system of M donors and N acceptors, (2.96) can be generalized as:

$$E = \frac{1}{M} \sum_{i=1}^M E_i = \frac{1}{M} \sum_{i=1}^M \sum_{j=1}^N \frac{\left(\frac{R_0}{R_{ij}} \right)^6}{1 + \left(\frac{R_0}{R_{ij}} \right)^6}, \quad (2.97)$$

where R_{ij} is the distance of i^{th} donor from j^{th} acceptor. The following relation between the quantum yield of donor in the presence and absence of acceptor can be obtained by combining (2.82), (2.90) and (2.93):

$$Q^{DA} = Q^D(1 - E). \quad (2.98)$$

From (2.98), it is clear that the donor emission is reduced due to FRET by a factor of $1 - E$. The reduction in donor emission due to FRET is called *donor quenching*. It can be used to quantify the interaction between donor and acceptor using measurements of donor fluorescence intensity in the presence and absence of acceptors. During this process, the quantum yield of acceptor remains unchanged.

The excitation rate of the donor is not affected by FRET. By contrast, the excitation rate of the acceptor in the presence of FRET, as is clear from Fig. 1.2, chapter 1 is changed, as described by the following equation:

$$\Gamma^{ex,AD} = \Gamma^{ex,A} + \Gamma^{ex,D}E, \quad (2.99)$$

where $\Gamma^{ex,AD}$ is the excitation rate of acceptor in the presence of donors, and $\Gamma^{ex,D} = I_0(\lambda_{ex})/(hc N_A)\varepsilon^D(\lambda_{ex})$ and $\Gamma^{ex,A} = I_0(\lambda_{ex})/(hc N_A)\varepsilon^A(\lambda_{ex})$ are the excitation rate constants of D and A , respectively in the absence of FRET. $I_0(\lambda_{ex})$, $\varepsilon^D(\lambda_{ex})$, $\varepsilon^A(\lambda_{ex})$ are the intensity of incident radiation and the absorption cross section of donor and acceptor at the excitation wavelength, h is the Planck constant, c is the speed of the light, and N_A is Avogadro's number. The increase in acceptor excitation rate due to FRET is called *acceptor sensitized emission* and can be used to detect FRET from the measurements of acceptor emission intensity.

2.6.2 Determination of FRET efficiency in terms of intensity-based measurable parameters

In principle, FRET based on fluorescence measurements can be used to determine the size of oligomers formed by proteins and the quaternary structure of the oligomers. To begin with, let us write the expressions for emission intensities of donors in the presence of acceptors $F^{DA}(\lambda_{ex})$ and acceptors in the presence of donors $F^{AD}(\lambda_{ex})$, respectively excited at wavelength λ_{ex} : (17):

$$F^{DA}(\lambda_{ex}) = F^D(\lambda_{ex}) - F_D^{FRET}, \quad (2.100a)$$

and

$$F^{AD}(\lambda_{ex}) = F^A(\lambda_{ex}) + F_A^{FRET}, \quad (2.100b)$$

where $F^D(\lambda_{ex})$ and $F^A(\lambda_{ex})$ are fluorescence emission following direct excitation by laser light of wavelength λ_{ex} , F_D^{FRET} is the loss of donor emission due to FRET, and F_A^{FRET} is the gain of acceptor emission due to stimulation through FRET. We define the FRET efficiency as the extent to which the donors are quenched by acceptors as:

$$E_{app} = \frac{F_D^{FRET}}{F^D(\lambda_{ex})}. \quad (2.101)$$

The left-hand sides of (2.100) may be determined simultaneously using decomposition of measured fluorescence spectra (20, 21) and by eliminating the acceptor bleed-through (22). A spectral decomposition method provides two quantities, k^{DA} and k^{AD} , which are equal to the maximum emission intensity for donors in the presence of acceptors, and for acceptors in the presence of donors, respectively (20). These quantities may be used to determine the total number of photons emitted per unit of time by integrating the fluorescence spectra, $I^{DA}(\lambda_{ex}) = k^{DA}i^D(\lambda_{em})$ and $I^{AD}(\lambda_{ex}) = k^{AD}i^A(\lambda_{em})$, over all emission wavelengths; that is:

$$\begin{aligned}
 F^{DA}(\lambda_{ex}) &= k^{DA} \int i^D(\lambda_{em}) d\lambda_{em} \\
 &= k^{DA} w^D,
 \end{aligned}
 \tag{2.102a}$$

and

$$\begin{aligned}
 F^{AD}(\lambda_{ex}) &= k^{AD} \int i^A(\lambda_{em}) d\lambda_{em} \\
 &= k^{AD} w^A,
 \end{aligned}
 \tag{2.102b}$$

where $i^D(\lambda_{ex})$ and $i^A(\lambda_{ex})$ are the emission intensities of the pure donor and pure acceptor spectra normalized to their maximum values, and w^A and w^D are the integrals of the elementary spectra of the acceptor and donor, respectively. F_D^{FRET} and F_A^{FRET} are related as (23):

$$F_D^{FRET} = \frac{Q_D}{Q_A} F_A^{FRET}.
 \tag{2.103}$$

By choosing the FRET pairs such that the acceptor molecules are only excited through FRET (i.e., $F^A(\lambda_{ex}) \approx 0$), then (2.101) together with (2.100), (2.102) and (2.103) gives:

$$E_{app} = \frac{1}{1 + \frac{Q^A k^{DA} w^D}{Q^D k^{AD} w^A}}.
 \tag{2.104}$$

Equation (2.104), together with the parameters k^{DA} and k^{AD} and the spectral integrals of the individual fluorescent species determined separately, is used to evaluate the apparent FRET efficiency, E_{app} , from the fluorescence spectra of each pixel in an image.

2.6.3 Prediction of E_{app} values for different oligomer geometries

Within an oligomeric complex of size larger than two, different configurations of the complex are possible depending upon the number of donors and acceptors and their positions within the complex. The different configurations of the oligomeric complex are expected to show distinct E_{app} values. In the case of simple geometries, it is possible to express the apparent FRET efficiencies of different configurations of an oligomeric complex in terms of pairwise FRET efficiency, E_p , which is equal to the FRET efficiency between a single donor and a single acceptor in a dimeric complex. To illustrate this point, let us begin by assuming a configuration of a circular-shaped octameric complex of the type shown in Fig. 2.8. The apparent FRET efficiency of this complex is given by (17) :

$$E_{app} = \frac{1}{7} \sum_{i=1}^7 E_{ij}, \quad (2.105)$$

or

$$E_{app} = \frac{1}{7} \left(2 \frac{\Gamma^{FRET}/(\Gamma^r + \Gamma^{nr})}{1 + \Gamma^{FRET}/(\Gamma^r + \Gamma^{nr})} + 2 \frac{\Gamma_1^{FRET}/(\Gamma^r + \Gamma^{nr})}{1 + \Gamma_1^{FRET}/(\Gamma^r + \Gamma^{nr})} + 2 \frac{\Gamma_2^{FRET}/(\Gamma^r + \Gamma^{nr})}{1 + \Gamma_2^{FRET}/(\Gamma^r + \Gamma^{nr})} + \frac{\Gamma_3^{FRET}/(\Gamma^r + \Gamma^{nr})}{1 + \Gamma_3^{FRET}/(\Gamma^r + \Gamma^{nr})} \right). \quad (2.106)$$

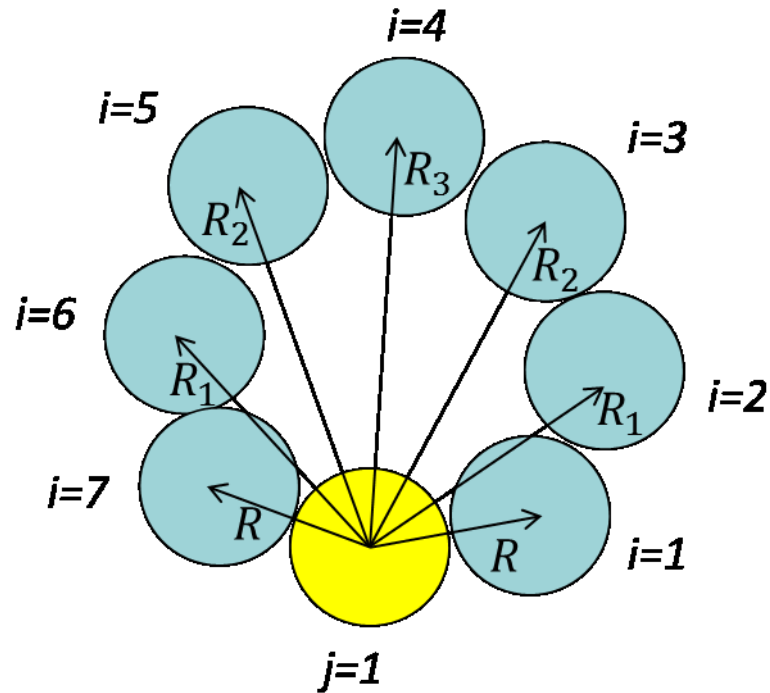


Figure 2.8: Configuration of a circular octamer representing seven donors (turquoise color) and one acceptor (yellow). R , R , R_2 , R_3 and R_4 represent the distances from the donors to the acceptor. i and j represent the donors and acceptor respectively.

The factor two in front of the first, second and third fractions account for the fact that FRET efficiencies for donors one and seven, two and six, three and five with one acceptor are identical, assuming circular symmetry of the complex, i.e., that either static or dynamic averaging of the orientation factor applies. From (2.95), the rate of energy transfer through FRET for donors adjacent to acceptor $\Gamma^{FRET} = (\Gamma^{r,D} + \Gamma^{nr,D})^{-1} \left(\frac{R_0}{R}\right)^6$, is much larger than that of those donors which are far from acceptor $\Gamma_i^{FRET} = (\Gamma^{r,D} + \Gamma^{nr,D})^{-1} \left(\frac{R_0}{R_i}\right)^6$ for $i = 1, \dots, 3$. Therefore, neglecting the second, third, and fourth term to the first approximation, (2.106) becomes:

$$E_{app} = \frac{2}{7} \frac{\Gamma^{FRET}/(\Gamma^r + \Gamma^{nr})}{1 + \Gamma^{FRET}/(\Gamma^r + \Gamma^{nr})} = \frac{2}{7} E_p \quad (2.107)$$

where we have used the notation $E_p = [\Gamma^{FRET}/(\Gamma^r + \Gamma^{nr})]/[1 + \Gamma^{FRET}/(\Gamma^r + \Gamma^{nr})]$. The symbol E_p denotes the pair-wise FRET efficiency, which is equal to the FRET efficiency between a single donor and a single acceptor in a dimeric complex. The circular shaped octamer can assume several configurations depending upon the number of donors and acceptors and their relative positions within the complex. The configuration shown in Fig. 2.8 is one of the different possible configurations. The expressions for E_{app} for other configurations of circular shaped octamer can be derived following the similar reasonings as for the configuration shown in Fig. 2.6.

The apparent FRET efficiencies, in terms of pairwise FRET efficiencies for different configurations of a few simple geometries, are summarized in Fig. 2.9. The FRET efficiency distributions obtained from the experiments are simulated against different models, a few of them summarized in Fig. 2.9, to obtain the best fit. Based on the model that fits the data best, the quaternary structure and stoichiometry of proteins associating to form oligomers are determined. In chapter 6, we have extended this method based on distribution of FRET efficiencies to determine the quaternary structure of dynamic complexes and used the model described in Fig. 2.9 to determine quaternary structure of Wzm-Wzt transporter in living cells.



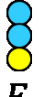
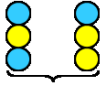
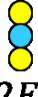















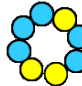





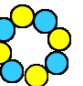
 E_p	 $\frac{2E_p}{1 + E_p}$	 $\frac{E_p}{2}$	 E_p	 $\frac{2E_p}{1 + E_p}$			
 $\frac{2}{3}E_p$	 E_p	 $\frac{2E_p}{1 + E_p}$	 $\frac{2}{3}E_p$	 E_p	 $\frac{1E_p^2 + 3E_p}{2}$	 $\frac{2E_p}{1 + E_p}$	 $\frac{3E_p}{1 + 2E_p}$
 $\frac{2}{7}E_p$	 $\frac{1}{3}E_p$	 $\frac{2}{5}E_p$	 $\frac{1}{2}E_p$	 $\frac{E_p}{3} \frac{2 + E_p}{1 + E_p}$	 $\frac{2E_p}{5} \frac{2 + E_p}{1 + E_p}$	 $\frac{2}{3}E_p$	
 $\frac{4}{5}E_p$	 $\frac{E_p}{2} \frac{2 + E_p}{1 + E_p}$	 $\frac{2E_p}{5} \frac{3 + E_p}{1 + E_p}$	 E_p	 $\frac{2E_p}{5} \frac{3 + 2E_p}{1 + E_p}$	 $\frac{2E_p}{3} \frac{2 + E_p}{1 + E_p}$	 $\frac{2E_p}{1 + E_p}$	

Figure 2.9: The apparent FRET efficiency expressions for different configurations of an octamer. Relationships between apparent FRET efficiencies associated with individual configurations and that between a single donor and a single acceptor within a dimer (E_p) for different geometries is given. Note that only FRET-productive configurations (i.e., complexes containing at least one donor and at least one acceptor) are shown. This figure is adapted from the reference (24).

References

1. Clegg, R. M. (1996) Fluorescence resonance energy transfer. *Fluorescence Imaging Spectroscopy and Microscopy*, Chemical Analysis, eds Wang X. F. and Herman B. (John Wiley & Sons, Inc), Vol 137.

2. Perrin, J. (1927) Fluorescence et induction moléculaire par résonance. *C. R. Hebd. Seances Acad. Sci.* **184**:1097-1100.
3. Cairo, G. (1922) Über Entstehung wahrer Lichtabsorption und scheinbare Koppelung von Quantensprungen. *Z. Phys.* **10**:185-199.
4. Pringsheim, P. (1928) *Luminescence and phosphorescence im lichte der neueren atomtheorie* (Interscience, Berlin).
5. Perrin, F. (1933) Interaction entre atomes normal et activite. Transferts d'activation. Formation d'une molécule activitee. *Ann. Institut Poincare* **3**:279-318.
6. Agranovich, V. M. and Galanin, M. D. (1982) *Electronic excitation energy transfer in condensed matter* (Amsterdam: North-Holland Publishing Company).
7. Clegg, R. M. (1992) Fluorescence resonance energy transfer and nucleic acids. *Methods Enzymol* **211**:353-388.
8. Förster, T. (1946) Energiewanderung und fluoreszenz. *Naturwissenschaften* **6**:166-175.
9. Stryer, L. and Haugland, R. P. (1967) Energy transfer: a spectroscopic ruler. *Proc. Natl. Acad. Sci. USA* **58**:719-726.
10. Jackson, J. D. (1975) *Classical Electrodynamics* (John Wiley & Sons, New Jersey).
11. Lakowicz, J. R. (2006) *Principles of Fluorescence Spectroscopy* (Springer, New York, NY, USA).
12. Hilborn, R. C. (2002) Einstein coefficients, cross sections, f values, dipole moments, and all that. *Am. J. Phys.*
13. Kallman, H. and London, F. (1928) Über quantenmechanische energieübertragungen zwischen atomaren systemen. *Z. Physik. Chem.* **B2**:207-243.
14. Tregidgo, C., Levitt, J. A., and Suhling, K. (2008) Effect of refractive index on the fluorescence lifetime of green fluorescent protein. *J Biomed Opt* **13**:031218.
15. Sakurai, J. J. (*Modern Quantum Mechanics*).
16. Raicu, V. and Popescu, A. I. (2008) *Integrated Molecular and Cellular Biophysics* (Springer, London, United Kingdom).
17. Raicu, V. (2007) Efficiency of resonance energy transfer in homo-oligomeric complexes of proteins. *J. Biol. Phys.* **33**:109-127.
18. Elangovan, M., Day, R. N., and Periasamy, A. (2002) Nanosecond fluorescence resonance energy transfer-fluorescence lifetime imaging microscopy to localize the protein interactions in a single living cell. *J. Microsc.* **205**:3-14.
19. Bacskai, B. J., Skoch, J., Hickey, G. A., Allen, R., and Hyman, B. T. (2003) Fluorescence resonance energy transfer determinations using multiphoton fluorescence lifetime imaging microscopy to characterize amyloid-beta plaques. *Biomed Opt.* **8**:368-375.
20. Raicu, V., Jansma, D. B., Miller, R. J., and Friesen, J. D. (2005) Protein interaction quantified in vivo by spectrally resolved fluorescence resonance energy transfer. *Biochem. J.* **385**:265-277.
21. Zimmermann, T., Rietdorf, J., Girod, A., Georget, V., and Pepperkok, R. (2002) Spectral imaging and linear un-mixing enables improved FRET efficiency with a novel GFP₂-YFP FRET pair. *FEBS Lett.* **531**:245-249.

22. Piston, D. W. and Kremers, G. J. (2007) Fluorescent protein FRET: the good, the bad and the ugly. *Trends in Biochemical Sciences* **32**:407-414.
23. Raicu, V., *et al.* (2009) Determination of supramolecular structure and spatial distribution of protein complexes in living cells. *Nat. Photonics* **3**:107-113.
24. Raicu, V. (2010) FRET-based determination of protein complex structure at nanometer length scale in living cells. *Nanoscopy and Multidimensional Optical Fluorescence Microscopy*, ed Diaspro A. (CRC Press, Boca Raton).

Chapter 3. Pixel versus average FRET: Numerical simulations

As described in earlier chapters, energy can be transferred from an excited donor to an acceptor non-radiatively through FRET, provided the acceptor is in close vicinity of the excited donor. When both molecules are fluorescent, the term "fluorescence resonance energy transfer" is used, although the energy is not actually transferred by fluorescence (1). If fluorescent probes are attached to known sites of two macromolecules of interest or of the same macromolecule, FRET efficiency measurements allow one to evaluate inter and intra-molecular distances or changes thereof. FRET can be detected using both fluorescence lifetime imaging (FLIM) (2-10) and fluorescence intensity measurements (7, 8, 11-18).

Provided that the usual distance and orientation conditions are fulfilled (see the theoretical section below), FRET may occur both between monomers within functional complexes (which may be either long- or short-lived) and non-interacting molecules expressed in high concentrations inside biological cells. In the latter case, the donor- and acceptor- tagged proteins need not associate with each other in order to exchange excitation energy; only their concentration needs to be high enough so that the average distance between them is of the order of the Förster distance. This undesired energy transfer, known as "stochastic FRET," may generate background noise in FRET studies aimed at identifying functional interactions. For example, it has been claimed that stochastic FRET has contaminated the results of relevant biological interactions in several studies of bioluminescence resonance energy transfer (BRET) of G-protein

coupled receptor oligomerization (19). This problem, which is generally assumed to be relevant also to FRET measurements, has been investigated theoretically by several investigators, either analytically or numerically (20-25).

Early FRET-based investigations of protein-protein interactions employed wide-field microscopes or spectrofluorometers to measure average fluorescent emission from individual cells, cell populations, or solutions of fluorescent molecules. The data in such experiments have been normally analyzed by plotting the *average* FRET efficiency of individual cells, synthetic vesicles, or even entire cell populations against the acceptors and donors concentrations or their ratios, and interpreting the results in light of models for functional and/or stochastic FRET (1, 13, 26, 27). While this approach has been successful in detecting global properties of molecular interactions, when applied to spatial distributions of molecular complexes in cells or cellular regions of interest, it poses two kinds of difficulties: (a) the average-based approach makes the explicit or implicit assumption that the distribution of molecules inside the cell is homogeneous, although, for instance, cytoplasmic proteins may be excluded from regions occupied by organelles or other macromolecular complexes, while membrane proteins may be sequestered within cytoskeletal cages or lipid microdomains (also known as 'rafts'). Such heterogeneity may lead to significant changes in the average FRET efficiency, which may not be distinguished from changes in the distance between monomers within a protein complex, and (b) the process of averaging of a distribution of FRET efficiency values washes out the rich information otherwise contained in a distribution of FRET efficiencies. This includes relative contributions of random and functional FRET, as well

as contributions by different pathways for energy transfer that may be present in protein complexes containing more than one donor and one acceptor.

The comparatively recent advent of laser-scanning microscopes, such as confocal and two-photon microscopes (1, 28, 29), provided opportunities for measuring fluorescence emission from thin optical sections of cells, thereby avoiding the averaging of fluorescence data along the z -axis. However, quantitative interpretation of FRET data obtained with scanning microscopes is often done in terms of cellular averages of FRET efficiencies; in many cases when pixel-level data are obtained, the analysis remains mostly qualitative, e.g., in the form of the so-called ratiometric FRET, instead of FRET efficiency (13, 30-32). This situation is perhaps reminiscent of several decades of evolution of the FRET theory within the framework created by the classical technology. In addition, unresolved technological challenges in laser-scanning microscopy for a while have prevented investigators from obtaining all the information necessary to estimate the FRET efficiency at pixel level in a time shorter than that of molecular diffusion (24).

Laser-scanning microscopes for lifetime or intensity measurements allow one to detect the signal from very small focal volumes of the sample. Under physiological expression levels of the proteins of interest, the small focal volumes contain only a few (ideally, only one) molecules or molecular complexes and therefore the information contained in each image pixel is mostly single-molecule or single-molecular-complex-level. To take full advantage of the opportunities introduced by laser-scanning microscopes, theoretical models and methods of data analysis need to be further

developed. Analytical calculations of energy transfer between multiple donors and acceptors are rather complex and require numerous simplifying assumptions. Förster (25) derived an expression for FRET efficiency for very low concentrations of excited donors distributed at random in mixtures with acceptors. Similar calculations for FRET efficiency were done by Eisinger (24) and Wolber and Hudson (23) for FRET efficiency in two dimensions. Analytical expressions have also been derived for oligomeric complexes containing arbitrary numbers of monomers (33). Many practical situations are still more conveniently tackled using numeric approaches.

Numerical Monte Carlo Simulations (MCS) have been used to calculate the FRET efficiency between chromophores constrained in various geometries. Snyder and Freire (22) examined the quenching of donor chromophores distributed in two dimensions. Demidov (34) used MCS to calculate energy transfer using the mean of randomly generated decay rates. Berney and Danuser (21) included competition between donors for the same acceptors to examine the transfer between fluorescent probes distributed on a surface. Corry et al. (20) used MCS to calculate FRET efficiency for an ensemble of linked pairs of acceptors and donors and pentameric structures. Frazier et al. (35) used FRET to investigate the domain formation in sphingomyelin/cholesterol/1-Palmitoyl-2-oleoylphosphatidylcholine (POPC) mixtures and used MCS to interpret their experimental results. Towles et al. (36) applied MCS to study the effect of membrane microheterogeneity and domain size on FRET. Kiskowski and Kenworthy (37) examined resonance energy transfer for disk-shaped membrane domains, relevant to FRET studies of lipid rafts.

In this chapter, we used MCS to compare FRET efficiency results between homogeneous and inhomogeneous spatial distributions of molecules. In all the cases investigated, the results of average FRET efficiencies for an entire image area were compared to the distributions of FRET efficiencies for that area, as if the data were obtained from wide-field and scanning optical microscopes, respectively. The main goals of this study are (a) to understand the effect of molecular crowding on functional interactions at concentrations commensurate with those encountered in experiments, and (b) to establish a procedure for FRET data simulations that can be used for information extraction from distributions of FRET efficiencies obtained experimentally. These results should be relevant to both intensity-based and FLIM-based investigations, as our simulations rely only on the Forster radius and intermolecular distances, while making no assumption regarding the manner in which the pixel-level FRET efficiencies are obtained experimentally.

3.1 Theoretical background

The problem of determining the efficiency of non-radiative energy transfer for systems of donors and acceptors distributed at random in two or three dimensions has been dealt with by several investigators (20, 21, 23-25, 38). Drawing upon those studies, in this section, we will outline a general method, used in this work, for numerical simulations of FRET efficiency for distributions of donors and acceptors on Euclidian as well as fractal lattices (see below). Fractal lattices are represented here by a well-known fractal object called *Sierpinski's carpet* (31, 39). The main assumptions made are as follows: (i) The

distribution of molecular species (i.e., dimers, donors, and acceptors) is random and uniform in the available space; however, for fractal lattices the distributions are non-uniform (relative to the Euclidian space), due to the inhomogeneous character of the lattice itself. (ii) The rate of donor excitation by light is very low, so that no more than one donor is excited at any single time (i.e., during the lifetime of the donor's excited state) in each focal spot. This ensures that excited donors do not compete for acceptors with other donors in their neighborhood. (iii) The orientation factor, which enters the Förster radius, R_0 (1), is independent of time on the timescale of the fluorescence lifetime. The third approximation implies that the time-scale for rotational diffusion of the donors and acceptors is either much shorter (i.e., dynamic averaging) or much longer (i.e., static averaging) than the lifetime of the donor's excited state.

Under the above approximations, the rate of de-excitation of a donor surrounded by N acceptors located at arbitrary distances R_j (where $j = 1, 2, \dots, N$) is given by (24, 25, 33):

$$k \equiv \tau_{DA}^{-1} = \tau_D^{-1} \left[1 + \sum_{j=1}^N \left(\frac{R_0}{R_j} \right)^6 \right], \quad (3.1)$$

where τ_{DA} and τ_D are the lifetime of the excited donor in the presence and absence of acceptors, respectively, and R_0 is the Förster radius, which depends on a number of physical parameters, such as the relative orientation of the transition dipoles of the donor and the acceptor (1). If the probability density, $P(t)$ of the donor being excited at $t = 0$ is

$P(0) = 1$, then the probability density for the donor to still be excited at a time t must satisfy the differential equation:

$$-\frac{dP(t)}{dt} = kP(t) = \tau_D^{-1} \left[1 + \sum_{j=1}^N \left(\frac{R_0}{R_j} \right)^6 \right] P(t). \quad (3.2)$$

Integration of Eq. 3.2 gives:

$$P(t) = e^{-t/\tau_D} \prod_{j=1}^N \exp \left[- \left(\frac{t}{\tau_D} \right) \left(\frac{R_0}{R_j} \right)^6 \right]. \quad (3.3)$$

In the absence of resonance energy transfer, the sum in Eq. 3.2 becomes zero, and the survival probability density for the excited state is $P_0(t) = e^{-t/\tau_D}$.

If $P(t-t')dt'$ denotes the probability that a donor excited at t' is still excited at time t (with $P(0) = 1$), then the relative quantum yield measured in a fluorescence experiment is given by:

$$\frac{Q^{DA}}{Q^D} = \frac{\int_{-\infty}^t P(t-t')dt'}{\int_{-\infty}^t P_0(t-t')dt'} = \frac{\int_0^{\infty} P(t')dt'}{\int_0^{\infty} P_0(t')dt'}, \quad (3.4)$$

where $P_0(t-t')$ is the probability density function analogous to $P(t-t')$ when no FRET occurs, while Q^D and Q^{DA} are the donor quantum yields in the absence and presence of the acceptor (i.e., of FRET), respectively.

Substituting (3. 3) into (3.4) and using $P_0(t') = e^{-t'/\tau_D}$, we get:

$$\frac{Q^{DA}}{Q^D} = \frac{1}{1 + \sum_{j=1}^N \left(\frac{R_0}{R_j} \right)^6}. \quad (3.5)$$

Since the FRET efficiency, E , is related to the two quantum yields by $E = 1 - Q^{DA}/Q^D$ (31, 33), Eq. 3.5 becomes:

$$E = \frac{\sum_{j=1}^N \left(\frac{R_0}{R_j} \right)^6}{1 + \sum_{j=1}^N \left(\frac{R_0}{R_j} \right)^6}. \quad (3.6)$$

In the case of M donors and N acceptors distributed in a small excitation area (equal to the focal spot area in a confocal or two-photon microscope), the FRET efficiency is obtained as the average over all FRET efficiencies, E_i , defined by Eq. 3.6, namely:

$$E = \frac{1}{M} \sum_{i=1}^M E_i = \frac{1}{M} \sum_{i=1}^M \frac{\sum_{j=1}^N \left(\frac{R_0}{R_{ij}} \right)^6}{1 + \sum_{j=1}^N \left(\frac{R_0}{R_{ij}} \right)^6}. \quad (3.7)$$

This equation applies to homogeneous as well as inhomogeneous distributions of molecules on Euclidian as well as fractal lattices.

3.2 Methods

We generated random distributions of molecules on two different planar surfaces: (i) a planar Euclidian surface (i.e., a square), which allows for donors and acceptors to be distributed uniformly, and (ii) a well-characterized fractal lattice called *Sierpinski's carpet* (31, 39), which has a fractional dimension and therefore confines the monomers and dimers to certain allowed areas (see Fig. 3.1). All simulations were performed using the software package Mathematica 6.0 (Wolfram Research Inc., IL, USA). The electronic file comprising our simulation algorithm may be provided upon request to those interested, and it essentially follows the steps described below.

First, a lattice of area $25 \mu\text{m}^2$ was defined, which is comparable to the area of a small-to medium-size biological cell (such as yeast, erythrocyte, etc). Herein, this is called the '*total excitation area.*' To populate the two-dimensional lattices with donors, acceptors, and/or dimers, random pairs of coordinates were generated by the program; these coordinates defined the positions of each molecule. In the case of dimeric complexes, two pairs of coordinates were generated. The coordinates corresponding to the position of the donor were generated first, and then the associated acceptor was constrained to have any random coordinates within a circle of 6 nm radius centered on the donor coordinates. Since a Förster distance of 5 nm was assumed for all calculations (which is typical for several combinations of green fluorescent protein variants, which are often used in experiments), this radius corresponds to a FRET efficiency $E_d \sim 0.25$. To create a fractal distribution of molecules, such as the one corresponding to stage $n = 1$ in Fig. 3.1, additional steps were required to constrain the coordinates of all monomers or

dimers to fall within the allowed areas of the Sierpinski carpet (Fig. 3.1), by using the following procedure:

1. The coordinates of a monomer or a dimer were generated as described above.
2. As it is well known, the Sierpinski carpet is generated by dividing each side of the large square by a factor of 3, removing the middle square, and then repeating the process n times for each remaining square. The values of the monomer or dimer coordinates were therefore expanded by a factor of 3, which is the scaling factor of the Sierpinski carpet. Thus, if L is the length of the carpet, the minimum possible value that the expanded x - (or y -) co-ordinate could take was zero, while the maximum value was $3L$.
3. Next, the expanded x - (or y -) coordinate was divided by the length of the carpet, L , to obtain the reduced coordinate, ξ . A function, $Floor[\xi]$, was used to find the greatest integer that was less than or equal to ξ , where ξ is a real number. For example, for $\xi = 2.4$, $Floor[\xi] = 2$.
4. If, for a particular molecule (or dimer) $\xi \in (1,2)$, then $Floor[\xi] = 1$, and that molecule was not considered any further in the simulations (because it fell in the excluded square of the first stage of the Sierpinski carpet); otherwise, the molecule was retained for subsequent determinations of FRET efficiency.
5. Steps 1 through 4 were repeated until the desired number of monomers and dimers were placed on Sierpinski's carpet.

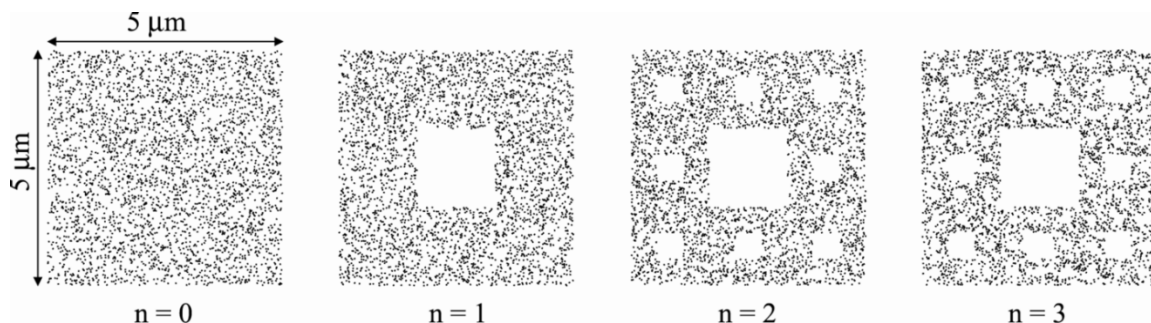


Figure 3.1: Different stages in the generation of a fractal distribution of molecules embedded in an Euclidian square. The stage represented by $n = 0$ is identical to the Euclidian square surface, while cases for $n \geq 1$ represent different stages in the construction of the fractal structure. The model represents the Sierpinski carpet, which has a fractal dimension 1.893. For $n \rightarrow \infty$, the surface area tends to zero (31, 39).

To generate distributions of monomers and/or dimers for the n -th stage of the Sierpinski's carpet, we used the same procedure described above (by steps 1 through 5), except that each procedure was applied to a sub-carpet of length $\frac{L}{3^n}$ instead of L .

In order to determine the distribution of FRET efficiencies, the excitation area occupied by monomers and/or dimers was divided into smaller areas of $0.25 \times 0.25 \mu\text{m}^2$, each of which being roughly equal to the area of a diffraction-limited *focal spot* of a focused light beam in a laser-scanning microscope. Depending on the total number of donors, M , and acceptors, N , distributed in each lattice, it was possible to have zero, one, or more of each type of molecule (i.e., donors, acceptors, and dimers) in every focal spot. Therefore, an average FRET efficiency was computed for each focal spot using Eq. 3.7. When dimers were present, one term of the sum in Eq.3.7 accounted for the fixed distance between a donor and an acceptor within the dimer. In general, there exists a low but finite probability that the donor and the acceptor of the same dimer fall in separate but

adjacent focal spots. To avoid such situations, a simple subroutine checked whether the coordinates of the donor and acceptor of each dimer fell in the same focal spot, and only those dimers for which the condition was fulfilled were kept in the computer memory.

After choosing appropriate bin ranges for FRET efficiency values, the average FRET efficiency value for each focal spot was placed in an appropriate bin, and histograms were prepared using the accumulated bin counts, in order to generate the statistical distribution of FRET efficiencies for the total excitation area. Such distributions are expected to be obtained from measurements with laser-scanning microscopes. The average FRET efficiency, E_{ave} , for an entire excitation area (as it would be obtained from wide-field microscopy) was also computed.

3.3 Results and discussion

While the simplified classical picture of donors surrounded by uniform distributions of acceptors (23, 38) has been a useful first approximation to solutions of interacting molecules, more elaborate models are often required for biological cells (20, 21, 35-37), which are characterized by an inhomogeneous distribution of material. For instance, cytoplasmic proteins may be excluded from regions occupied by other molecular complexes (such as the ribosomes) or by membrane-bound cellular organelles (e.g., the nucleus, or the mitochondria), while membrane proteins may be sequestered within cytoskeletal cages or lipid microdomains or ER-internal membrane. Therefore, depending on their degree of inhomogeneity, most biological systems present two types of molecular distributions, or combinations thereof: (a) donors and acceptors confined to

disconnected oligomers or larger assemblies (i.e., micro-domains); (b) bicontinuous, percolative (31, 40) distributions of donors and acceptors.

In the study described here, we used two-dimensional simulations to determine the FRET efficiency for molecules distributed on *excitation areas* of size comparable to that of biological cells, both for Euclidan and for (incomplete) fractal structures obtained for a finite number of steps in the construction of Sierpinski carpet (39) (see Fig. 3.1 above). The donors and acceptors were distributed at random on the fractal lattices, the only restriction being that they occupied an 'allowed' area of the structure. The average FRET efficiency per donor was calculated using Eq. 3.7 for each *focal spot* (of area $0.25 \times 0.25 \mu\text{m}^2$) comprising the *total excitation area*, as described in the Methods section.

The first case investigated was that of a random distribution of *non-interacting* molecules tagged with donors and acceptors. In spite of the lack of physical interaction between the tagged molecules, a type of energy transfer, known as *stochastic FRET*, may still occur between the donor and acceptor tags (23). As seen in Fig. 2, for both types of lattices investigated, most FRET efficiencies assumed values close to zero, with just a small fraction of excitation areas showing non-vanishing FRET efficiencies. This was true for any proportion of donors and acceptors investigated, even though the total concentration considered (4800 molecules per $25 \mu\text{m}^2$) corresponded to as many as 332,160 molecules dispersed in a relatively small cell (with a volume of $\sim 125 \mu\text{m}^3$).

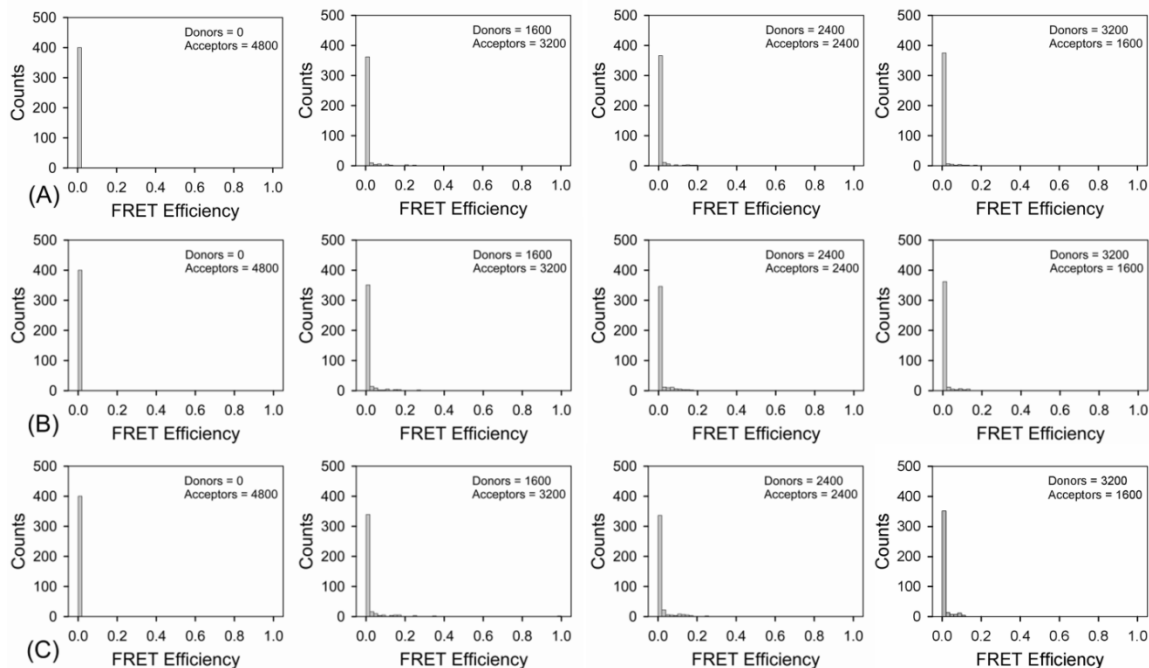


Figure 3.2: Histograms showing the distribution of FRET efficiencies for donors and acceptors randomly scattered on lattices of the type shown in Fig. 3.1. (A) Euclidian (i.e., uniform) distribution of molecules; (B) Fractal distribution with $n = 5$; (C) Fractal distribution with $n = 7$. The total number of 4800 donors and acceptors per whole excitation area ($25 \mu\text{m}^2$) corresponds to 12 molecules per focal spot of area $0.25 \times 0.25 \mu\text{m}^2$.

The distributions of FRET efficiencies shown in Fig. 3.2 were characterized by very small average values (see Fig. 3.3); these values are typical for measurements performed using a wide-field microscope. We concluded that stochastic FRET is not a major source of signal, even when relatively large average concentrations of interacting molecules are present. Furthermore, local increases in concentration, caused by the large exclusion areas of the fractal lattices, failed to enhance the FRET efficiency to a significant extent. This weak effect stems from the fact that FRET is a non-linear process, in which the efficiency of energy transfer dies out rather rapidly with the distance between donors and acceptors (as R^{-6}). We have only obtained large values of FRET

efficiencies for concentrations of donors and acceptors much larger than physiological expression levels of most proteins in the cell. The number of proteins are of the order of 2000 molecules in the mammalian cell (41).

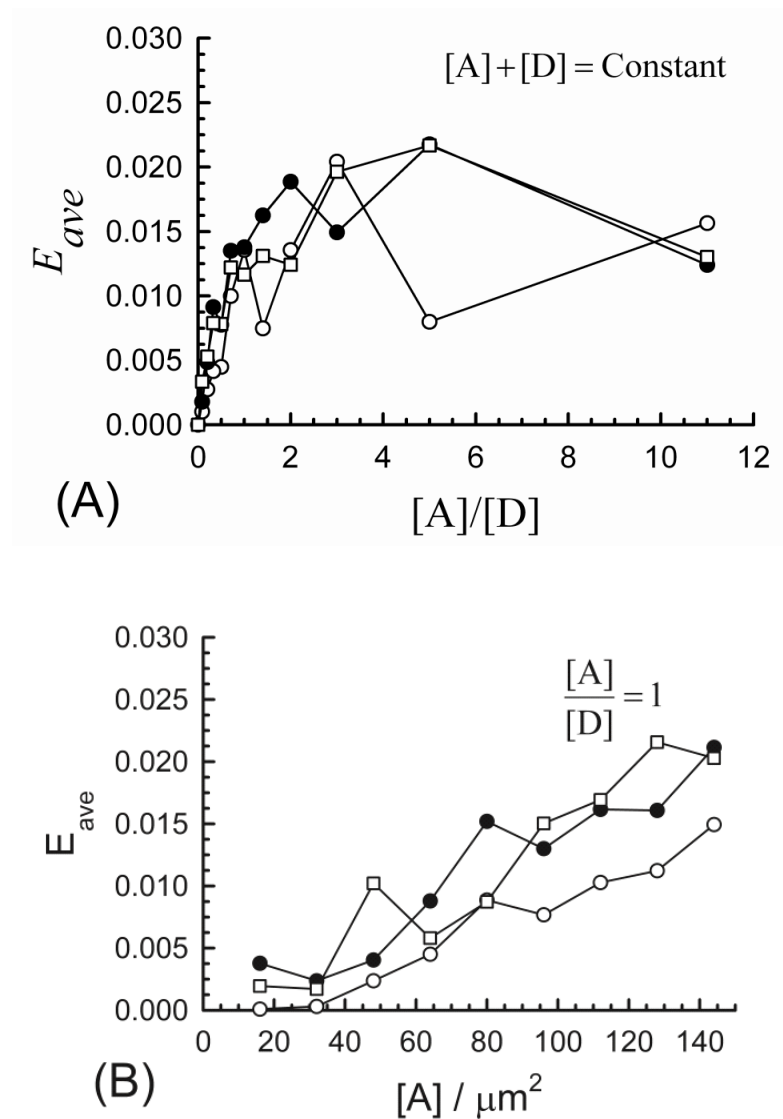


Figure 3.3: Dependence of the average FRET efficiency for distributions of monomeric donors and acceptors on (A) the ratio of acceptor to donor concentrations, $[A]/[D]$ (for $[A]+[D]=\text{constant}$), and (B) the concentration of acceptors, $[A]$ (for $[A]/[D] = \text{constant}$), for Euclidian and fractal distributions of molecules. The significance of the symbols is: *open circles*, $n = 0$; *filled circles*, $n = 5$; *open squares*, $n = 7$.

Next, we investigated whether stochastic FRET may contribute significantly to the FRET efficiency of distributions of functional hetero-dimers. Herein, we define "hetero-dimers" as both long-lived (or constitutive) and transient associations of molecules tagged with donor and acceptor fluorophores. We placed hetero-dimers at various concentrations on Euclidian as well as fractal lattices, and calculated the FRET efficiency for all donors present in each focal spot of the excitation beam. Eq. 3.7 was again used for this purpose, in which one term of the sum over summation variable j accounted each time for the fixed distance between a donor and an acceptor within the dimer (see *Methods*).

As can be seen in Fig. 3.4, the main bar in each of the histograms (corresponding to a value $E_d \sim 0.25$ for the FRET efficiency) was due to the presence of the dimers themselves, with some broadening of the distribution towards larger values occurring due to an occasional exchange of energy between donors and acceptors belonging to different dimers. This broadening effect reflected the stochastic FRET component, which was only marginally stronger for the inhomogeneous distribution corresponding to the Sierpinski carpet, compared to the Euclidian lattice. In addition to these features, most histograms also presented sizeable bars corresponding to cases when no FRET occurred. It is worth noting here that, while instances with zero-FRET efficiency were rare for Euclidian distributions, such occurrences were always observed in fractal distributions, even for relatively high dimer concentrations. This is because there are always regions within the Sierpinski carpet from which dimers are excluded.

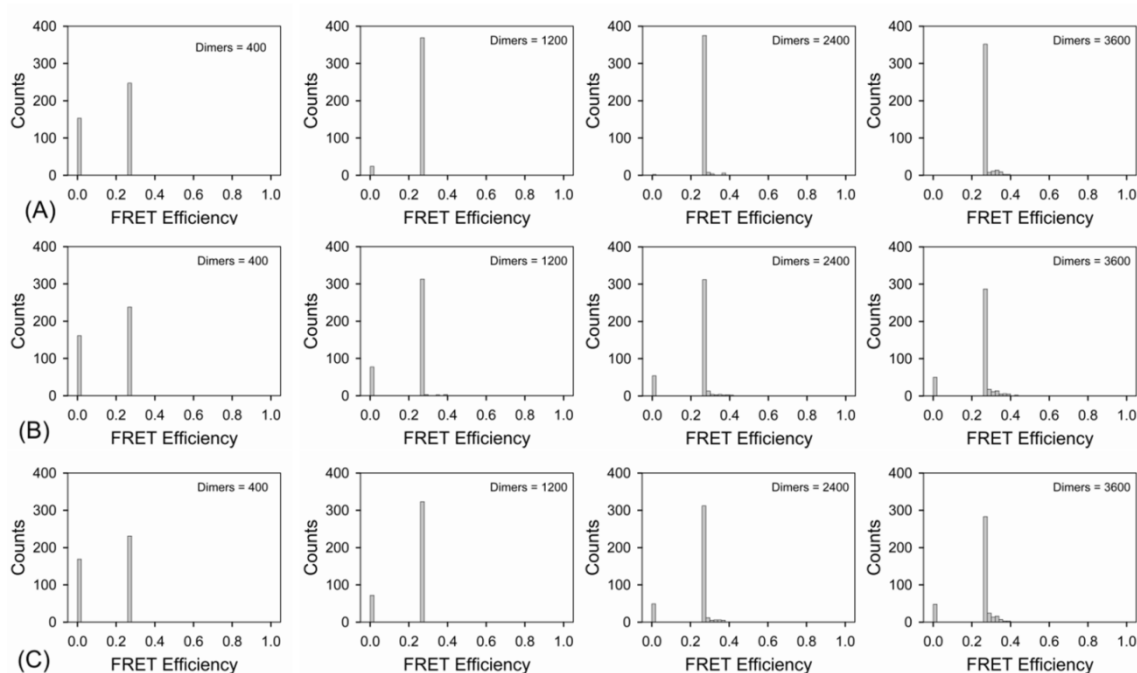


Figure 3.4: Histograms showing the distribution of FRET efficiencies for dimers distributed at random on lattices of the type shown in Fig. 3.1: (A) Euclidian (i.e., uniform) distribution of dimers; (B) Fractal distribution with $n = 5$; (C) Fractal distribution with $n = 7$. The first concentration in each row (i.e., 400 dimers per whole excitation area) corresponds to 1 dimer per focal spot, while the last concentration represents 9 dimers per focal spot.

The presence of bare spots in the fractal lattice leads to significant differences between the average efficiencies of fractal and Euclidian distributions, as seen in Fig. 3.5. This finding pertains to the experimental situation where an average cellular FRET efficiency is calculated for cells containing protein complexes that do not spread uniformly throughout the cell (such as membrane proteins), which leads to an underestimation of the efficiency. In addition, it appears from Fig. 3.5 that the average efficiency does depend on the total number of hetero-dimers (which is the same with that of acceptors, for $[A]/[D] = 1$), even though each dimer is expected to contribute a

constant FRET efficiency portion to the average value. This is because, at low concentrations of dimers (which are actually similar to protein expression levels of practical interest), the presence of excitation spots with no dimers at all decreases the average efficiency; an increase in concentration leads to a decrease in the number of bare spots, hence, the observed increase in the average FRET efficiency.

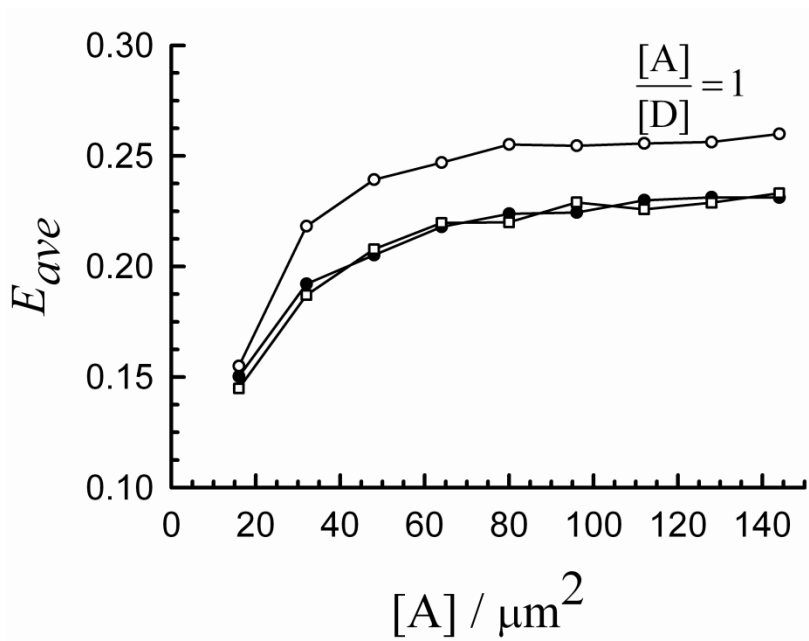


Figure 3.5: Dependence of the average FRET efficiency for distributions of dimers on the concentration of acceptors, $[A]$ (for $[A]/[D]=1$), for Euclidian and fractal surfaces. The significance of the symbols is: *open circles*, $n = 0$; *filled circles*, $n = 5$; *open squares*, $n = 7$.

We next investigated the behaviour of hetero-dimers in the presence of various concentrations of free donors and acceptors. Such mixtures may be relevant to several

biological situations, such as, for instance, the case where there exist populations of free donors and acceptors, some of which may interact to form short-lived dimers. Another example is when donor- and acceptor-tagged proteins only exist as dimeric complexes, but either the donor or the acceptor tag takes a longer time to become mature and hence fluorescent. This may be described as either a mixture of dimers and donors, or dimers and acceptors, depending on which tag takes longer to become mature. Typical results from these simulations are shown in Fig. 3.6 for Euclidian as well as fractal distributions (as defined in Fig. 3.1). As seen, while the FRET efficiency value corresponding to dimers ($E_d \sim 0.25$) appeared in all histograms, the distribution of values was broader than expected for purely dimeric populations. This can be accounted for by the following two mechanisms: (i) The slight broadening of the distribution of efficiencies towards larger values was due to the stochastic FRET between dimers as well as between donors in the dimers and monomeric acceptors. (ii) A more pronounced broadening of the distribution of FRET efficiency values towards values lower than the dimer FRET efficiency value, E_d , was accompanied by a decrease in the number of instances when the E_d value was detected. The occurrence of FRET efficiencies lower than E_d was caused by the fact that free donors, present in a focal spot alongside with dimers, contributed a value less than E_d (even zero) to the sum in Eq. 3.7, but increased the total number of donors, M , in that spot. This reduction in FRET efficiency represents a type of 'stochastic' FRET whose importance has been less appreciated before, and which is not due to a real interaction between donors and acceptors but to the increase in M caused by the mere presence of free donors in the excitation spot. Also, while the broadening of the distributions of FRET efficiencies towards higher values is somewhat more prominent for fractal lattices

compared to Euclidian ones (compare Figs. 3.6B and 3.6C to Fig. 3.6A), a more obvious difference is the presence of bars of sizeable height at zero FRET efficiency for fractal distributions, even for very high concentrations of dimers. The latter effect leads to systematically lower values of the average fret efficiency for fractal lattices (see Fig. 3.7).

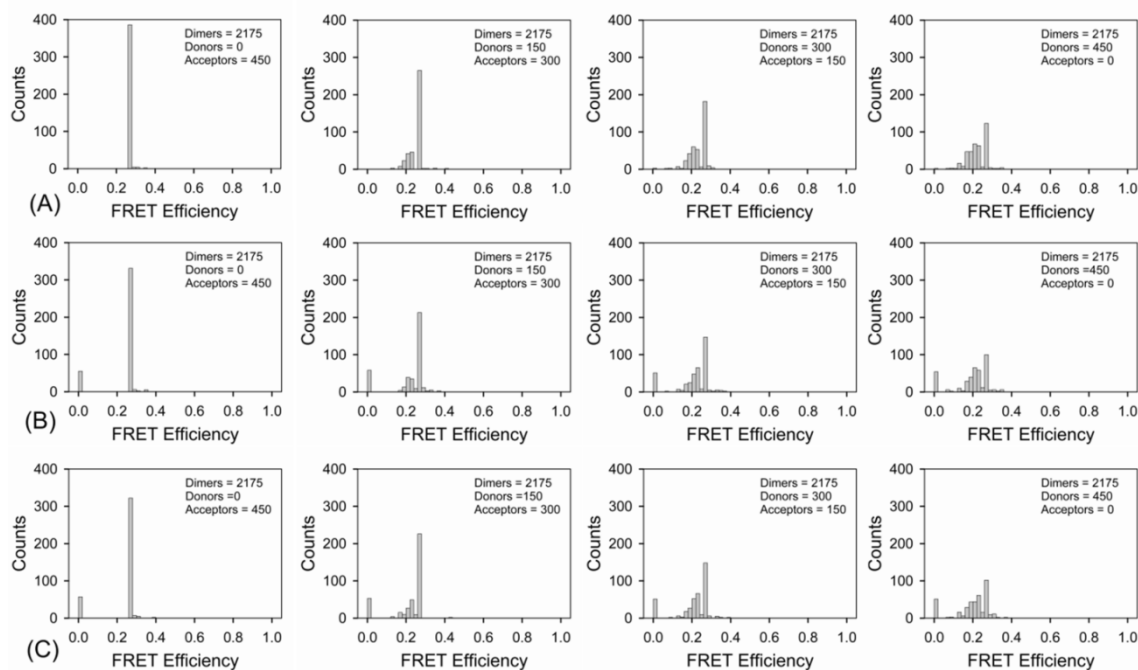


Figure 3.6: Histograms showing the distribution of FRET efficiencies for mixtures of dimers, donors, and acceptors distributed at random on lattices of the type shown in Fig. 3.1: (A) Euclidian (i.e., uniform) distribution of dimers; (B) Fractal distribution with $n = 5$; (C) Fractal distribution with $n = 7$.

Experimental observation of distributions of FRET efficiencies similar to those shown in Fig. 3.6 has been reported in a recent study (16) on an artificial dimeric construct formed by two green fluorescent protein variants (42) linked by two amino acids, whereby the acceptor (yellow fluorescent protein) is known to take a somewhat

longer time to become mature and fluoresce. While in the histogram representation of FRET efficiencies one is still able to distinguish between stochastic and functional FRET for mixtures of dimers and free monomers, the average cellular efficiency hardly provides any usable information (see Fig. 3.7). This difficulty is caused by the dependence of the average FRET efficiency on the ratio of donor to acceptor concentrations, which needs to be determined from separate measurements. An additional difficulty is caused by the fact that the average efficiency depends on whether the spatial distribution of molecules is homogeneous or inhomogeneous. This becomes apparent when comparing the results obtained for the fractal case to those obtained for Euclidian lattices (see Fig. 3.7).

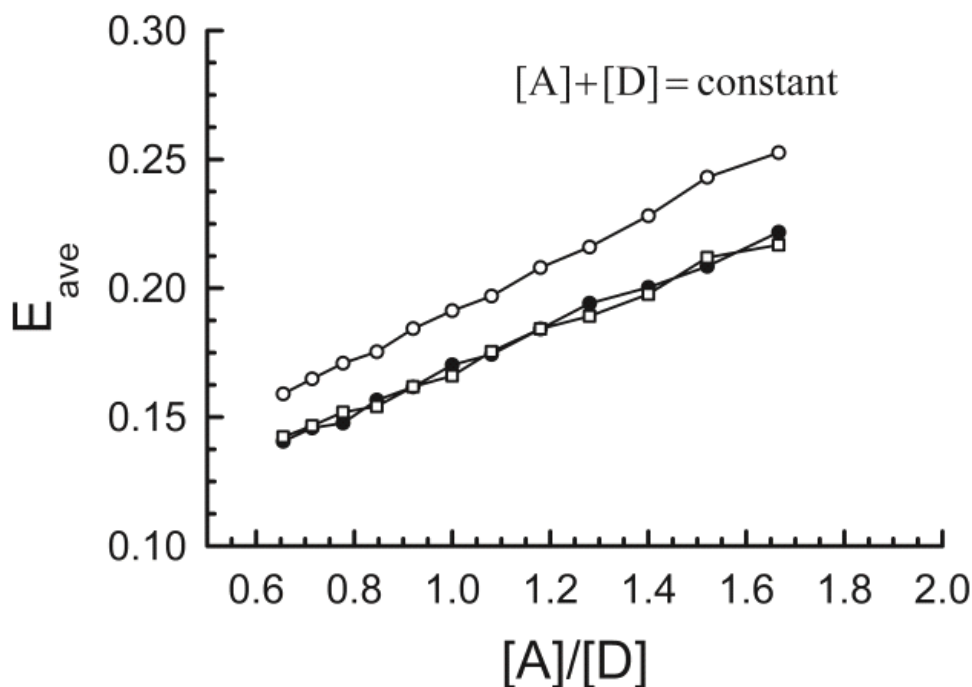


Figure 3.7: Dependence of the average FRET efficiency for distributions of dimers on the ratio of total acceptor to total donor concentrations, $[A]/[D]$ (for $[A]+[D]=\text{constant}$) for the three molecular distributions shown in Fig. 3.1. The significance of the symbols is: *open circles*, $n = 0$; *filled circles*, $n = 5$; *open squares*, $n = 7$.

We also note that the discriminating power of the distribution-based analysis decreased gradually with the ratio of free donors to total donor concentrations, as manifested by a reduction in the height of the bar corresponding to $E_d = 0.25$ in Fig. 3.6. This reduction may cause difficulties in separating between stochastic and functional FRET by mere visual inspection of the histogram when free donors represent more than 20% of the total donor population (data not shown). However, even in that unfavorable case it may still be possible to separate functional (i.e., dimeric) FRET from the stochastic FRET background by performing detailed analyses of the histograms. Notwithstanding possible complications caused by the point-spread function of the microscope (43), this kind of analysis could be done by recognizing that the FRET efficiencies in the histograms corresponding to values less than E_d represent various combinations of dimers and free donors, and therefore contain information about E_d , which could be extracted by fitting the simulated curves to experimental distributions.

3.4 Conclusion

The experimental approach based on average FRET efficiencies has been widely used in FRET studies, perhaps because early studies employing wide-field microscopes and spectrofluorometers have shaped our understanding of FRET. Our numerical simulations described above indicated that the inherent inhomogeneity of any biological cell, together with the presence of a form of stochastic FRET (not involving true interactions between donor- and acceptor-tagged molecules), which has not been recognized before, may

dramatically diminish the practical utility of the average-based approach. By contrast, a distribution-based (or pixel-level) approach afforded by laser-scanning microscopes should allow one to fully quantify the information regarding the distribution of FRET efficiencies. Admittedly, this first modeling attempt to investigate an important problem in FRET, as described above, required some simplifications regarding the size of the oligomers as well as the ideality of the point-spread function of the optical instrument (43), which was considered to map a *point*-object onto a *point*-image. However, a careful evaluation of the physical situation indicates that, while future studies will likely incorporate useful refinements, the main conclusions of this study should remain valid for any oligomer size (such as trimers and tetramers) and for more realistic point-spread functions. We believe that this analysis will offer a basis for extraction of structural and stoichiometric information from whole distributions of FRET efficiencies by using simulation-based fitting of experimental FRET data.

References

1. Lakowicz, J. R. (2006) *Principles of Fluorescence Spectroscopy* (Springer, New York, NY, USA).
2. Maurel, D., *et al.* (2008) Cell-surface protein-protein interaction analysis with time-resolved FRET and snap-tag technologies: application to GPCR oligomerization. *Nat. Methods* **5**:561-567.
3. Spriet, C., *et al.* (2008) Enhanced FRET contrast in lifetime imaging. *Cytometry A* **73**:745-753.
4. Wallrabe, H. and Periasamy, A. (2005) Imaging protein molecules using FRET and FLIM microscopy. *Curr Opin Biotechnol* **16**:19-27.
5. Chen, Y. and Periasamy, A. (2004) Characterization of two-photon excitation fluorescence lifetime imaging microscopy for protein localization. *Microsc. Res. Tech.* **63**:72-80.

6. Elangovan, M., Day, R. N., and Periasamy, A. (2002) Nanosecond fluorescence resonance energy transfer-fluorescence lifetime imaging microscopy to localize the protein interactions in a single living cell. *J. Microsc.* **205**:3-14.
7. Parsons, M., Vojnovic, B., and Ameer-Beg, S. (2004) Imaging protein-protein interactions in cell motility using fluorescence resonance energy transfer (FRET). *Biochem. Soc. Trans.* **32**:431-433.
8. Hink, M. A., Bisselin, T., and Visser, A. J. (2002) Imaging protein-protein interaction in living cells. *Plant Mol. Biol.* **50**:871-883.
9. Lakowicz, J. R., *et al.* (1990) Conformational Distributions of Melittin in Water-Methanol Mixtures from Frequency-Domain Measurements of Non-radiative Energy-Transfer. *Biophysical Chemistry* **36**:99-115.
10. Royer, C. A. and Scarlata, S. F. (2008) Fluorescence Approaches to Quantifying Biomolecular Interactions. *Fluorescence Spectroscopy* **450**:79-106.
11. Liu, S., Abbondanzieri, E. A., Rausch, J. W., Le Grice, S. F. J., and Zhuang, X. (2008) Slide into Action: Dynamic Shuttling of HIV Reverse Transcriptase on Nucleic Acid Substrates. *science* **322**:1092-1097.
12. Chen, Y., Mauldin, J. P., Day, R. N., and Periasamy, A. (2007) Characterization of spectral FRET imaging microscopy for monitoring nuclear protein interactions. *J. Microsc.* **228**:139-152.
13. Raicu, V., Jansma, D. B., Miller, R. J., and Friesen, J. D. (2005) Protein interaction quantified in vivo by spectrally resolved fluorescence resonance energy transfer. *Biochem. J.* **385**:265-277.
14. Milligan, G., Ramsay, D., Pascal, G., and Carrillo, J. J. (2003) GPCR dimerisation. *Life. Sci.* **74**:181-188.
15. Angers, S., Salahpour, A., and Bouvier, M. (2002) Dimerization: an emerging concept for G protein-coupled receptor ontogeny and function. *Annu. Rev. Pharmacol. Toxicol.* **42**:409-435.
16. Raicu, V., *et al.* (2009) Determination of supramolecular structure and spatial distribution of protein complexes in living cells. *Nat. Photonics* **3**:107-113.
17. Ha, T., *et al.* (1996) Probing the interaction between two single molecules: fluorescence resonance energy transfer between a single donor and a single acceptor. *Proc. Natl. Acad. Sci. USA* **93**:6264-6268.
18. Caorsi, V., *et al.* (2007) FRET measurements on fuzzy fluorescent nanostructures. *Microsc. Res. Tech.* **70**:452-458.
19. James, J. R., Oliveira, M. I., Carmo, A. M., Iaboni, A., and Davis, S. J. (2006) A rigorous experimental framework for detecting protein oligomerization using bioluminescence resonance energy transfer. *Nat. Methods* **3**:1001-1006.
20. Corry, B., Jayatilaka, D., and Rigby, P. (2005) A flexible approach to the calculation of resonance energy transfer efficiency between multiple donors and acceptors in complex geometries. *Biophys. J.* **89**:3822-3836.
21. Berney, C. and Danuser, G. (2003) FRET or no FRET: a quantitative comparison. *Biophys. J.* **84**:3992-4010.
22. Snyder, B. and Freire, E. (1982) Fluorescence energy transfer in two dimensions : a numeric solution for random and nonrandom distributions. *Biophys. J.* **40**:137-148.

23. Wolber, P. K. and Hudson, B. S. (1979) An analytic solution to the Förster Energy Transfer problem in two dimensions. *Biophys. J.* **28**:197-210.
24. Eisenthal, K. B. and Siegel, S. (1964) Influence of resonance transfer on luminescence decay. *J.Chem.Phys.* **41**:652-655.
25. Förster, T. (1949) Experimentelle und theoretische Untersuchung des zwischenmolekularen Übergangs von Elektronenanregungsenergie. *Z. Naturforsch., A: Astrophys. Phys. Phys. Chem.* **4**:321-327.
26. You, M., Li, E., Wimley, W. C., and Hristova, K. (2005) Förster resonance energy transfer in liposomes: Measurements of transmembrane helix dimerization in the native bilayer environment. *Analytical Biochemistry* **340**:154-164.
27. Kenworthy, A. K. and Edidin, M. (1998) Distribution of a glycosylphosphatidylinositol-anchored protein at the apical surface of MDCK cells examined at a resolution of <100 Å using imaging fluorescence resonance energy transfer. *J. Cell Biol.* **142**:69-84.
28. Periasamy, A. and Diaspro, A. (2003) Multiphoton microscopy. *J Biomed Opt* **8**:327-328.
29. Zipfel, W. R., Williams, R. M., and Webb, W. W. (2003) Non-linear Magic: Multiphoton Microscopy in the Biosciences. *Nat. Biotechnol.* **21**:1369 - 1377.
30. Hoffmann, C., *et al.* (2005) A FLAsH-based FRET approach to determine G protein - coupled receptor activation in living cells. *Nature Methods* **2**:171-176.
31. Raicu, V. and Popescu, A. I. (2008) *Integrated Molecular and Cellular Biophysics* (Springer, London, United Kingdom).
32. Nakanishi-Matsui, M., *et al.* (2000) PAR3 is a cofactor for PAR4 activation by thrombin. *Nature* **404**:609-613.
33. Raicu, V. (2007) Efficiency of resonance energy transfer in homo-oligomeric complexes of proteins. *J. Biol. Phys.* **33**:109-127.
34. Demidov, A. A. (1999) Use of Monte Carlo method in the problem of energy migration in molecular complexes in resonance energy transfer. D. L. Andrews and A. A. Demidov, Editors. Wiley, New York.:435-465.
35. Frazier, M. L., Wright, J. R., Pokorny, A., and Almeida, P. F. F. (2007) Investigation of domain formation in sphingomyelin/cholesterol/POPC mixtures by fluorescence resonance energy transfer and Monte Carlo simulations. *Biophys J* **92**:2422-2433.
36. Towles, K. B., Brown, A. C., Wrenn, S. P., and Dan, N. (2007) Effect of membrane microheterogeneity and domain size on fluorescence resonance energy transfer. *Biophys J* **93**:655-667.
37. Kiskowski, M. A. and Kenworthy, A. K. (2007) In silico characterization of resonance energy transfer for disk-shaped membrane domains. *Biophys J* **92**:3040-3051.
38. Dewey, T. G. and Hammes, G. G. (1980) Calculation on fluorescence resonance energy transfer on surfaces. *Biophys. J.* **32**:1023-1035.
39. Mandelbrot, B. B. (1982) *The Fractal Geometry of Nature* (Freedman, San Francisco).
40. Sahimi, M. (1994) *Applications of Percolation Theory* (Taylor & Francis, London).

41. Duncan, R. and McConkey, E. H. (1982) How many proteins are there in a typical mammalian cell? *Clin Chem* **28**:749-755.
42. Zimmermann, T., Rietdorf, J., Girod, A., Georget, V., and Pepperkok, R. (2002) Spectral imaging and linear un-mixing enables improved FRET efficiency with a novel GFP₂-YFP FRET pair. *FEBS Lett.* **531**:245-249.
43. Wells, K. S., Sandison, D. R., Strickler, J., and Webb, W. W. (1990) Quantitative Fluorescence Imaging with Laser Scanning Confocal Microscopy. *Handbook of Biological Confocal Microscopy*, ed Pawley J. B. (Plenum Press, New York and London).

Chapter 4. Linear and non-linear optical microscopy

Due to the advent of technologies for isolation, characterization, and mutation of naturally occurring fluorescent proteins (such as GFP and its variants) that can be tagged to the protein of interest, together with recent fluorescent imaging techniques (1), it is feasible to visualize, track and quantify molecular interactions with spatial and temporal resolution. Traditionally, fluorescence wide field microscopes are used for live cell imaging. However, the images obtained from these microscopes lack clarity because of light coming from points outside the focal plane. The invention of the confocal microscope in 1950 was a milestone in imaging technology. Laser scanning confocal microscopes (2) are capable of acquiring images of thin optical sections of cells and tissues (3). The three dimensional images can be reconstructed by acquiring the multiple thin section images.

Another breakthrough in imaging technology was the discovery of the two-photon laser scanning microscope (TPM) (4, 5) in 1990 by Denk and co-workers (4). This microscope exploits the ability of fluorescent molecules to absorb two photons simultaneously having their energy equal to the energy of a single photon. For multi-photon process to occur experimentally, a beam of the femtosecond pulsed laser is focused tightly through a high numerical aperture objective to confine the photons spatially and temporally. The intensity of the photons is high enough only in the small volume around the focal spot of the objective of the two-photon microscope for the two-photon excitation to occur, therefore, image sectioning is achieved without the pin-hole.

Pin-hole is a hole that helps in focusing light in the focal plane of the objective of the microscope or detection of light in detector coming from the focal plane.

In this chapter, we introduce the concept of one-photon and two-photon excitation. Next, we describe the working principle of laser scanning confocal microscopy. In addition, we present the two-photon microscope, which produces spectrally resolved images after a full scan of the fluorescent sample. We also describe the procedure for constructing spectral images from the images that correspond to different line scans. Though interest in multicolor imaging to study the molecular interactions in living cells is growing, the technical problems associated with the accurate and precise measurements of fluorescence are hampering the full realization of the potential. One of the requirements for FRET to occur is the spectral overlap of donor emission spectrum, and acceptor absorption spectrum which makes it difficult to accurately measure fluorescence signals to quantify FRET. Spectral imaging is a new technique where the spectrum of fluorescence emanating from each voxel of the sample is collected at each pixel of the image instead of acquiring data through two channels. This recorded fluorescence emission spectrum contains both the donor and acceptor fluorescence. Using spectrally resolved two-photon microscopy in conjunction with the judicious choice of FRET pairs and spectral unmixing, discussed later in this chapter, the technical problems encountered in FRET imaging, as described in chapter1, can be eliminated. The apparent FRET efficiency that relies on the fluorescence of donors in the presence of acceptors and the fluorescence of acceptors in the presence of donors, which

are determined through spectral unmixing, can be calculated at each pixel of the image using the formula for FRET efficiency derived in chapter 2.

4.1 One-photon vs. two-photon absorption

When a photon of wavelength λ is incident on an atom or molecule characterized by the ground state $|i\rangle$ with energy E_i and the excited state $|f\rangle$ with energy E_f such that:

$$E_f - E_i = hc/\lambda, \quad (4.1)$$

where h is the Plank constant and c is the speed of light, then the atom absorbs the energy of the photon to reach the excited state from the ground state. The absorption of energy by the atom or molecule from a single photon to reach the excited state from ground state is called one-photon absorption (OPA). Alternatively, the atom can reach to the excited state by simultaneously absorbing two photons having wavelengths λ_1 and λ_2 instead of absorbing a single photon of wavelength λ such that:

$$E_f - E_i = hc/\lambda = hc/\lambda_1 + hc/\lambda_2, \quad (4.2)$$

or

$$1/\lambda = 1/\lambda_1 + 1/\lambda_2. \quad (4.3)$$

The simultaneous absorption of two photons by the atom or molecule to reach the excited state from ground state at the place of a single photon with same energy is called two-photon absorption (TPA). The one-photon absorption and two-photon absorption processes are depicted in Fig. 4.1. The transition probabilities from ground state $|i\rangle$ to excited state $|f\rangle$ for one-photon excitation P_{OPE} , and two-photon excitation, P_{TPE} , are given by (6):

$$P_{OPE} \sim |\langle f | \vec{E}_\gamma \cdot \vec{r} | i \rangle|^2, \quad (4.4)$$

and

$$P_{TPE} \sim \left| \sum_m \frac{\langle f | \vec{E}_\gamma \cdot \vec{r} | m \rangle \langle m | \vec{E}_\gamma \cdot \vec{r} | f \rangle}{\epsilon_\gamma - \epsilon_m} \right|^2. \quad (4.5)$$

The term, $\vec{E}_\gamma \cdot \vec{r}$, appearing in (4.4) and (4.5) is the electric dipole interaction energy, where, \vec{E}_γ , is the electric field vector of the photon and \vec{r} is the position operator. ϵ_γ is the energy of the photon characterized by electric field \vec{E}_γ , m represents all intermediate states, and ϵ_m is the energy difference between the state m and the ground state. The parity transformation flips the sign of the position operator. When a physical operator changes it's after parity transformation, that physical operator is said to have odd parity. If the physical operator is invariant under parity transformation, that operator is said to have even parity. The parity of the transition dipole, $\langle f | \vec{E}_\gamma \cdot \vec{r} | i \rangle$, in one-photon excitation is odd. Thus, the absorption of one-photon changes the parity of the state. On the other hand, the parity of the transition dipole in two-photon excitation, $\langle f | \vec{E}_\gamma \cdot \vec{r} | m \rangle \langle m | \vec{E}_\gamma \cdot \vec{r} | f \rangle$, is even. Hence, in two-photon excitation only those transitions are allowed for which the parity of the states are conserved. Since intensity, I , is related to the electric field vector of the photon as:

$$I \propto \vec{E}_\gamma^2, \quad (4.6)$$

hence from (4.4) and (4.5), the transition probabilities for one-photon and two-photon absorption vary as a linear function of intensity of the photon and square of the intensity of the photon, respectively. Because of this, one-photon absorption is called a linear process and the two-photon absorption is called a non-linear process.

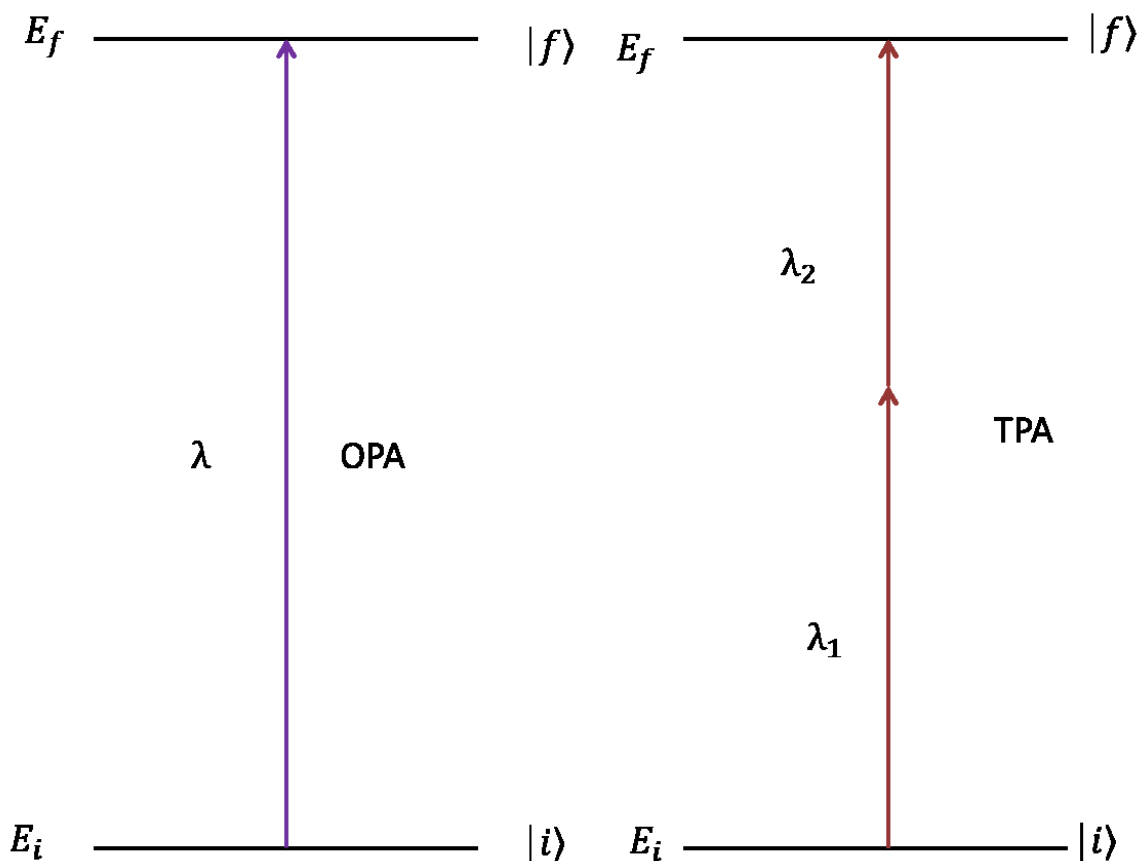


Figure 4.1: Energy level diagrams for one-photon absorption (OPA) and two-photon absorption (TPA). The energies corresponding to the ground state $|i\rangle$ and the excited state $|f\rangle$ are E_i and E_f respectively. The wavelength of the photon corresponding to one-photon absorption is λ and the wavelengths of photons corresponding to two-photon absorptions are λ_1 and λ_2 .

The two-photon excitation (TPE) was first predicted by Göppert-Mayer in 1931 in her doctoral dissertation and was first observed by Wolfgang Kaiser in 1961 in $\text{CaF}_2:\text{Eu}^{2+}$ crystal using laser excitation (7). The probability of one-photon absorption and two-photon absorption in (4.4) and (4.5) comes from the first order and second order solutions

of the time-dependent Schrödinger equation. Therefore, the probability of two-photon absorption is extremely low and will only occur where the density of photons is very high. Because of this reason, in two-photon microscopes, the fluorescence mainly comes from the focal spot and the fluorescence from the out of focus is eliminated which enables this microscope to image the thin section of the cell without pinholes.

For one-photon absorption, the loss of intensity as a function of distance is obtained by integrating (2.27) (see Fig. 2.3, Chapter 2) and is given by

$$I = I_0 e^{-\sigma C x}. \quad (4.7)$$

where σ is the one-photon absorption cross-section and C is the concentration of the medium subjected to one-photon absorption.

In the case of two-photon absorption, the loss of intensity per unit length is given by:

$$\frac{dI}{dx} = -\beta C I^2, \quad (4.8)$$

where β is the two-photon absorption cross section. Integration of (4.8) subject to the same boundary condition yields:

$$I = \frac{I_0}{1 + \beta C x I_0}. \quad (4.9)$$

The one-photon absorption cross section is measured in cm^2 while the two-photon absorption cross-section is measured in Göppert-Mayer (GM). 1GM is $10^{-50} \text{ cm}^4 \text{ sec/photon}$.

4.2 Laser scanning confocal microscope

In this microscope, the coherent light passes through the source pin-hole, which is situated at the conjugate plane with the scanning point in the sample. This light is reflected by the dichromatic mirror and is focused by the objective of the microscope on the focal plane. The laser beams are scanned across the specimen to get the image of the sample on the same focal plane. The emitted fluorescent light back propagates through the objective, and after passing through the dichromatic mirror, is focused on the detector pin-hole. Since this microscopy uses the single photon to excite the sample and the absorption cross section is large, a significant amount of emission also comes from the points above and below of the focal plane of the sample and an extended Airy disc is formed on the detector. However, because of the detector pinhole, the light emanating from out of focus planes is blocked by the detector pinhole. Thus the image of a section that is on the focal plane of the microscope is obtained. The schematic of laser scanning confocal microscope is shown in Fig 4.2.

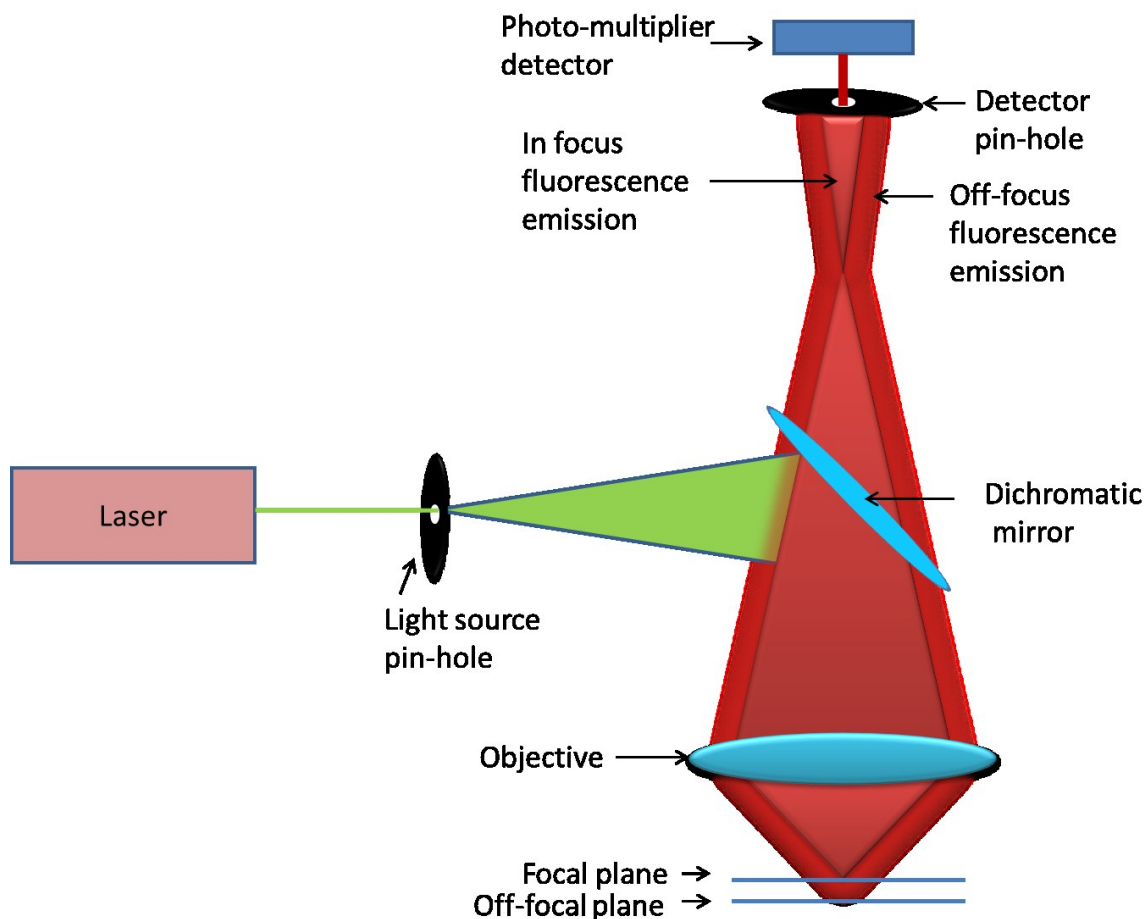


Figure 4.2: Schematic representation of laser scanning confocal microscope. The optical pathway and the components are indicated.

To study spectral FRET, many commercial laser scanning confocal microscopes are equipped with various detection schemes. This microscope has many advantages over the wide field microscopes. These are:

(i) It can produce thin optical sections ($0.5\mu\text{m}$ to $1.5\mu\text{m}$) of fluorescent samples that have thickness up to $50\mu\text{m}$ or more.

(ii) Since the image information is restricted to well-defined planes, the contrast of the images obtained from confocal microscope is better than that obtained from wide field microscope where the image information is blurred due to superposition of signals arising from off-focus planes of the sample. Hence, the signal-to-noise ratio in the confocal microscope is large compared to the wide field microscope (8).

(iii) The magnification of this microscope can be adjusted without changing the objective by varying the area scanned by the laser (9).

However, there are a few disadvantages associated with this microscope. These are:

(i) Since the excitation wavelength is very close to the emission wavelength (for example, the excitation wavelength for eGFP is 488nm and emission wavelength of it is 508nm), it is difficult to filter out the excitation signal from the emission signal which makes the signal-to-noise ratio low.

(ii) Due to exposure of the whole sample to excitation light, even if the signal is read from a thin optical section and due to slow reading of multiple wavelengths (in case of FRET imaging) at each point, there is photo-bleaching of fluorescent molecules in the entire sample.

4.3 Spectrally resolved two-photon microscope

The schematic of the homemade spectrally resolved two-photon microscope is shown in Fig. 4.3. A solid state laser (VerdiTM, Coherent Inc., CA, U.S.A., 532nm) (1) pumps the mode-locked Ti: Sapphire laser (KM Labs, CO, U.S.A.) (2). The mode-locked laser generates sub-ten femtosecond pulses of near infrared light, in the wavelength range 780nm to 860nm with FWHM=120nm. The light beam is controlled by a set of fixed mirrors (3&6) as well as two computer controlled scanning mirrors (Nutfield Technology Inc., NH, U.S.A.) (4), and expanded by the telescope (5). The beam is then focused on the sample (8) by the infinitely corrected objective with high numerical aperture (Nikon Instruments Inc. NY, 100X magnification, NA= 1.43, oil immersion) (7). The beam is focused to a diffraction-limited spot on the sample by the objective. With the help of x-y scanning mirrors (4), the spot is scanned across the fluorescent sample. Here, x and y are two mutually perpendicular directions on the sample as well as corresponding directions on the detector. As the spot is scanned, the fluorescent light emanating from every single spot in the sample back propagates and is collected by the objective (7) and sent to short pass dichroic mirror (6). The short pass dichroic mirror (6) allows fluorescent light having wavelength shorter than incident light pass through the dichroic mirror while reflecting back the near-IR light which reflected back from the sample together with the back propagated fluorescent light. The back propagated light, after passing through the dichroic mirror (6), passes through the tube lens (9), and the short pass filter (10), and then the transmission grating (11) which disperses the light into its spectral components, and finally it falls on the 2-D detector (12). The short-pass filter (10) rejects any residual infrared component in back propagated fluorescent light which would contaminate the

visible light we are interested in. The spectral components of fluorescence emission from the scanned spot form a line on the detector (12) after being dispersed by the grating (11). The laser spot is scanned using the galvanometric scanners (Nutfield Technology Inc., NH) (4) across the sample (along x-direction) such that the emission spectrum sweeps across the detector to form a rectangle. One 2-D image is captured for each line scanned on the sample in the x-dimension which corresponds to the actual x-dimension of the sample, and the y-dimension corresponds to the spectral dimension (wavelength). To get the image of the whole sample, many line scans for different y-values of the sample are performed with the help of x-y scanning mirrors (4). The individual images obtained corresponding to each line scans for different y values are reconstructed to get the spectral images. The reconstruction algorithm is described in the next section.

In two-photon microscopy, the fluorescent emission comes from the focal spot of the microscope hence the emission is inherently confocal. Therefore, it is unnecessary to descanned the emitted signal and non-descanned (external) detectors are used. The whole spectrum corresponding to each line scan is acquired at once in this microscope set up, which allows the fast acquisition of image in a non-descanned mode using an EM-CCD camera. Another feature of this microscope is its ability to provide transmission images. To get the transmission images, a white-light photodiode is placed under the microscope slide and a narrow-band interference filter is inserted in the light path before the transmission grating, which removes the blur caused by the diffraction grating. The optical scanners and EM-CCD camera were controlled by a computer. The software for that was written in-house in C++, and incorporates the image reconstruction algorithms.

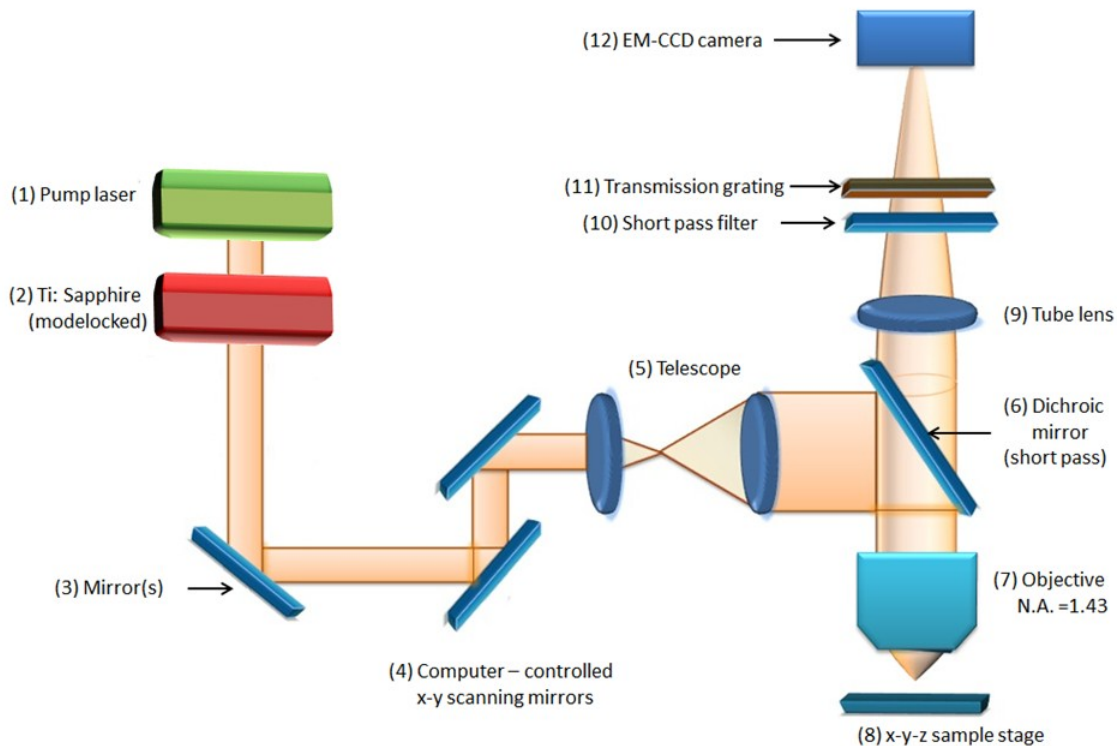


Figure 4.3: Schematic of spectrally resolved two-photon microscope. Different components of the microscope are indicated in the picture. This image is adopted from (10, 11).

There are many advantages of two-photon microscope over confocal microscopes.

These are (12) :

(i) The two-photon excitation wavelengths are twice the one-photon excitation wavelength; hence the attenuation due to scattering is reduced. Moreover, biological tissues are transparent to infrared radiation. Hence it is possible to image deep sections in biological tissues using two-photon microscopes.

(ii) The number of photons reaching the detector is larger than the number of photons in the confocal microscope; hence better signal-to-noise ratio.

(iii) Since the two-photon absorption cross section is small and absorption only occurs at the focal spot of the microscope, any photo-bleaching by the excitation light is confined to the sample layer located on the focal plane of the microscope.

(iv) The separation between excitation wavelength (infrared) and emission (visible) wavelengths in two-photon microscope is large and allows the filtering of excitation light leaking into the detection channel, thus reducing the background noise and permitting detection of signal from samples at low expression level.

(v) The absence of a confocal pinhole allows the use of non-descanned mode of detection in conjunction with CCD cameras (5), which leads to higher speed.

Since the wavelength of the two-photon is twice the wavelength in one-photon, the spatial resolution of the images obtained from two-photon microscope is poor than that obtained from one-photon microscope.

4.4 Image Reconstruction

Fluorescein solution, a uniformly fluorescing sample, was used to calibrate the line scanning procedure. In this procedure, the fluorescent spectra originating from adjacent y positions from the sample (for example say, from $y = y_0$ to $y = y_0 + \Delta y$) are such that they differ exactly one pixel along spectral dimension on the CCD camera. After performing the whole line scan of the sample consistent with the calibration procedure, the relationship between the row number and wavelength is known for the obtained images and is subsequently used for reconstruction of spectral images. To illustrate this point, let us consider the image corresponding to line scan in the sample at $y = y_0$. Let us assume that the transmission grating separates the emitted fluorescent light into twelve spectral components. The spectral images consistent with the calibration procedure and corresponding to $y = y_0, y = y_0 + \Delta y, y = y_0 + 2\Delta y$ and $y = y_0 + 3\Delta y$ are shown in Fig. 4.4. Now to reconstruct the image (let us say corresponding to wavelength λ_4) one finds row number 4 in the first image (i.e. the first y) corresponding to this wavelength. According to calibration procedure, the next row i.e. row number 5 of the second image (i.e., image corresponding to $y = y_0 + \Delta y$) corresponds to this wavelength. Similarly, the row number 6 of the third image, row number 7 of the fourth image and so on corresponds to the wavelength λ_4 .

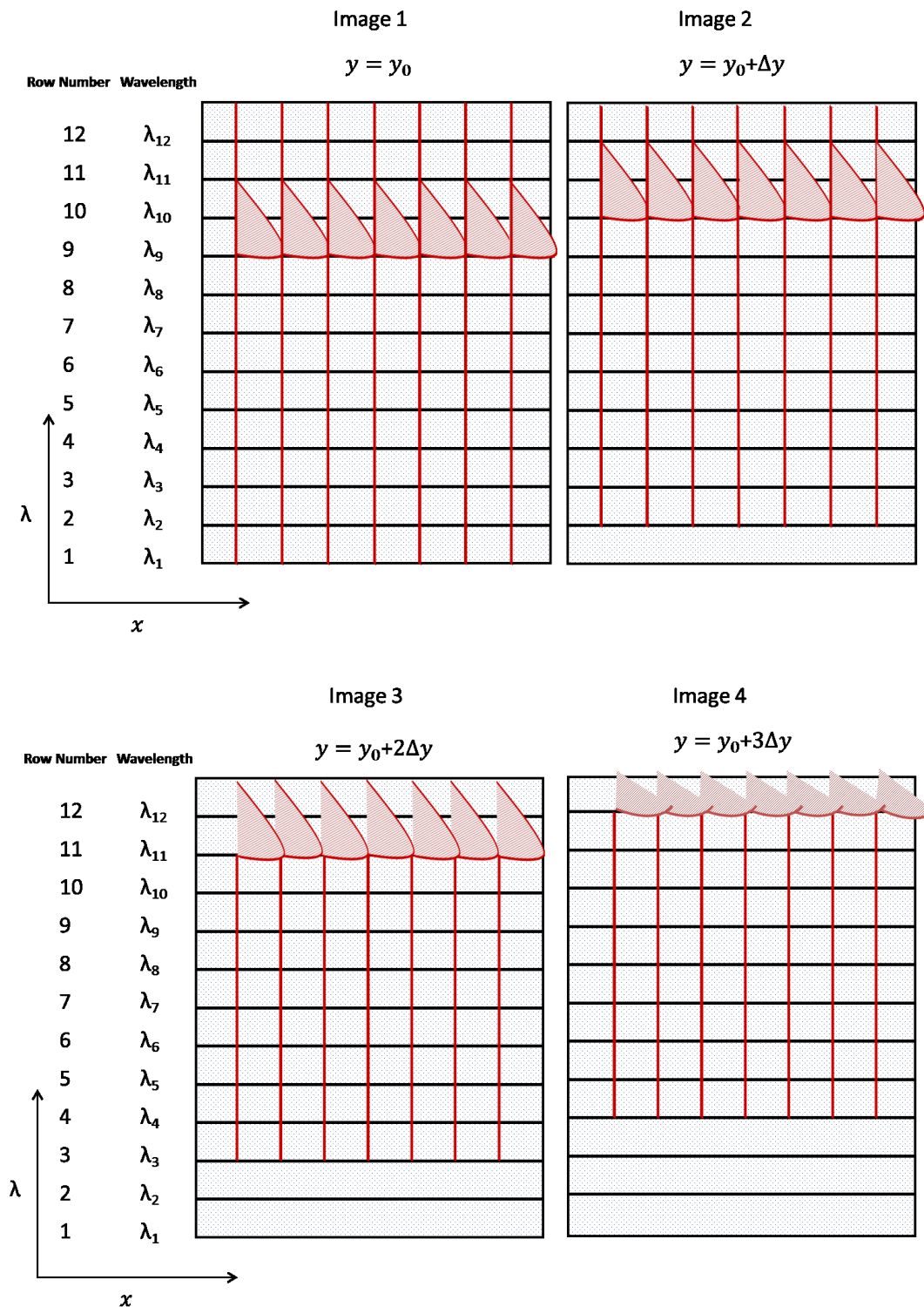


Figure 4.4: Images corresponding to different y positions within the sample. The fluorescence spectra along the spectral dimension differ exactly by one pixel between the two consecutive images that correspond to adjacent y positions within the sample. This figure is adapted from the supplementary material (11).

An image corresponding to the wavelength λ_4 is obtained by stacking the different row numbers corresponding to wavelength λ_4 in different images shown in Fig. 4.4. The reconstruction procedure of an image corresponding to wavelength λ_4 is schematically shown in Fig. 4.5. Similarly, the images corresponding to all wavelengths of emission spectra can be reconstructed.

Fluorescence Image for wavelength λ_4

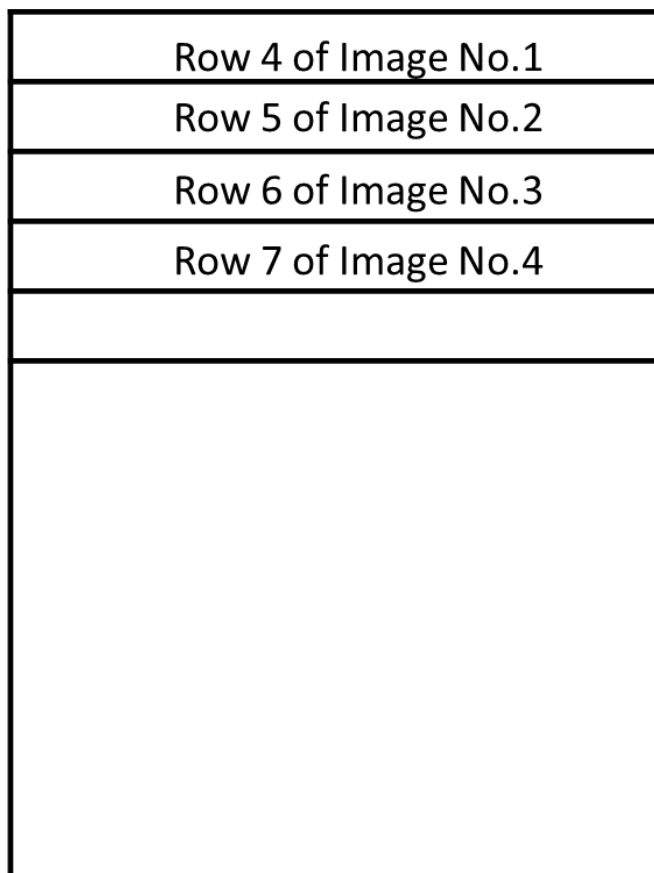


Figure 4.5: Illustration of the image reconstruction procedure corresponding to the wavelength, λ_4 from the images obtained from the different line scans corresponding to different values within the sample. This figure is adapted from supplementary material (11).

4.5 Spectral calibration of the microscope

Before collecting the data, one needs to spectrally calibrate the microscope. Spectral calibration of the microscope is done to assign the appropriate wavelength to each reconstructed image. For that standard sample is needed for which the fluorescence emission spectrum was known. The standard sample comes from the 100- μ M solution of fluorescein sodium salt (Uranine, Fischer Scientific, IL). This salt is dissolved in deionized water to make 100- μ M fluorescein solution. The full set of line scan is performed on this sample. The scanning parameter Δy is adjusted such that the fluorescent spectrum of the sample is shifted exactly one pixel upon one increment of x-y scanning mirrors position in y-direction.

The reconstructed images indexed by integer i , thus obtained, are opened by utilizing the function of the open source code software Image J (<http://rsb.info.nih.gov/ij/>) in ascending order and stacked. In this manner, the background corrected normalized fluorescent intensity of each reconstructed image as a function of i are determined. Since, the relationship between the wavelength of the emitted photons and the camera pixel position in the spectral dimension was approximately linear; therefore, the relationship between the reconstructed image number and the corresponding wavelength was also linear. Hence, the wavelength corresponding to the reconstructed image is given by:

$$\lambda_i = m(i - i_{max}) + \lambda_{max}, \quad (4.10)$$

where m is given by:

$$m = \frac{(\lambda_{max} - \lambda_{1/2})}{(i_{max} - i_{1/2})}. \quad (4.11)$$

Here, λ_i represents the i^{th} wavelength of the reconstructed image. The values of λ_{max} and $\lambda_{1/2}$ are the wavelengths corresponding to which the fluorescent intensities are maximum and half of maximum in the emission spectrum of fluorescein. i_{max} and $i_{1/2}$ represent the reconstructed image numbers corresponding to which the fluorescence intensities are maximum and half of the maximum.

4.6 Multicolor imaging

4.6.1 FRET basics

The naturally occurring fluorescent proteins that are widely used as FRET pairs come from a class of auto fluorescent proteins, called green fluorescent proteins (GFPs). For fluorophores to be considered as FRET pairs, the following conditions should be met:

(1) The emission spectrum of the donor should significantly overlap with the excitation spectrum of the acceptor. The overlap should be more than 30% to obtain efficient energy transfer.

(2) The separation between the donor excitation spectrum and acceptor excitation spectrum should be sufficiently large so that the direct excitation of acceptors due to donor excitation wavelength can be avoided as far as possible.

(3) The separation between the emission spectrum of the donor and the emission spectrum of the acceptor should be large enough to allow the measurement of fluorescence of each fluorophore independently.

GFP-based FRET imaging have been used to determine the compartmentalization and functional organization of living cells, tracing the movement of proteins inside cells, determining the stoichiometry of proteins and to determining the quaternary structure of proteins. Depending upon the biological applications, there are number of combinations that can be used as FRET pairs. Some of them are: GFP₂-YFP, GFP₂-Venus, CFP-YFP, CFP3A-SYFP2, CFP-dsRED, mTurquoise-SCFP3A, BFP-GFP, GFP or YFP-dsRED, Cy3-Cy5, Alexa488-Alexa555, Alexa488-Cy3, FITC- Rhodamine (TRITC), YFP-TRITC or Cy3.

As mentioned above, one of the important conditions for FRET to occur is the overlap of the emission spectrum of the donor with the absorption spectrum of the acceptor. The FRET signal, due to spectral overlap, is always contaminated because of the excitation of acceptor molecules by the donor excitation wavelength and by donor emission into the acceptor channel. This is called spectral bleed-through (SBT) or crosstalk signal into the acceptor channel. In principle, the SBT signal is same for one-

photon or two-photon FRET microscopy. This can be corrected during the image restoration if properly calibrated.

Crosstalk can be eliminated using spectral FRET and judicious choice of FRET pairs. In spectral FRET, the donor signal and acceptor signal are separated from the multicolor emission (i.e., combined emission of donor and acceptor) using spectral deconvolution (13, 14) which is described in the next section and choosing donor such that the excitation wavelength of donor does not excite acceptor directly and if it does, the direct excitation is negligible. The FRET pair that meets this criterion is GFP₂-YFP.

4.6.2 Spectral deconvolution

In spectral imaging, the fluorescence emission spectrum at each pixel of the image is collected. The spectrum at each pixel of this image consists of individual contributions of donor and acceptor signals. To calculate the apparent FRET efficiency at each pixel, the fluorescence of donors in the presence of acceptors and the fluorescence of acceptors in the presence of donors are needed to be separated (see determination of FRET efficiency section of chapter 2). These contributions are determined by fitting the measured spectrum at each pixel of the image to the function:

$$s_M(\lambda) = k^{DA}s_D(\lambda) + k^{AD}s_A(\lambda), \quad (4.12)$$

where $s_M(\lambda)$ is the simulated composite spectrum, $s_D(\lambda)$ is the elementary spectrum of donor and $s_A(\lambda)$ is the elementary spectrum of acceptor. k^{DA} and k^{AD} are the scaling factors for donor and acceptor respectively and represent the amount of fluorescence emitted by donors in the presence of acceptors and fluorescence of acceptors in the presence of donors respectively. The appropriate mathematical expressions for the

computation of values for k^{DA} and k^{AD} that are necessary to simulate the measured spectrum are obtained (13, 15) using least square calculations. These are:

$$k^{DA} = \frac{\sum(s_M \cdot s_D) \sum(s_A^2) - \sum(s_A \cdot s_D) \sum(s_M \cdot s_A)}{\sum(s_A^2) \sum(s_D^2) - [\sum(s_A \cdot s_D)]^2} \quad (4.13)$$

and

$$k^{AD} = \frac{\sum(s_M \cdot s_A) \sum(s_D^2) - \sum(s_A \cdot s_D) \sum(s_M \cdot s_D)}{\sum(s_A^2) \sum(s_D^2) - [\sum(s_A \cdot s_D)]^2}. \quad (4.14)$$

where $\sum(s_X \cdot s_Y)$ is the sum over the intensities corresponding to all wavelengths of the s_X and s_Y spectra in the parenthesis, with X and Y standing for the measured (M), donor (D), and acceptor (A) spectra.

References

1. Lippincott-Schwartz, J. and Patterson, G. H. (2003) Development and use of fluorescent protein markers in living cells. *Science* **300**:87-91.
2. Knebel, W. (2004) Optical Arrangement for Selection and Detection of the Spectral Region of a Light Beam and Confocal Scanning Microscope. *US Patent No 6,809,815 B2*.
3. Chen, Y. and Periasamy, A. (2004) Characterization of two-photon excitation fluorescence lifetime imaging microscopy for protein localization. *Microsc. Res. Tech.* **63**:72-80.
4. Denk, W., Strickler, J. H., and Webb, W. W. (1990) Two-photon laser scanning fluorescence microscopy. *Science* **248**:73-76.
5. Kim, K. H., Buehler, C., and So, P. T. C. (1999) High-speed, two-photon scanning microscope. *Appl. Opt.* **38**:6004-6009.
6. So, P. T., Dong, C. Y., Masters, B. R., and Berland, K. M. (2000) Two-photon excitation fluorescence microscopy. *Annu Rev Biomed Eng* **2**:399-429.
7. Kaiser, W. and Garrett, C. G. B. (1961) Two-photon excitation in CaF₂ : Eu²⁺. *Phys. Rev. Lett.* **7**:229.

8. Sandison, D. R. and Webb, W. W. (1994) Background rejection and signal-to-noise optimization in confocal and alternative fluorescence microscopes. *Appl Opt* **33**:603-615.
9. Diaspro, A. (2002) *Confocal and two-photon microscopy : Foundations, applications, and advances* (Wiley-Liss, New York).
10. Stoneman, M. R. (2010) Dielectric spectroscopy based monitoring of the cellular response to G protein coupled receptor/peptide interactions *in vivo*. PhD Dissertation (University of Wisconsin Milwaukee, 2010).
11. Raicu, V., *et al.* (2009) Determination of supramolecular structure and spatial distribution of protein complexes in living cells. *Nat. Photonics* **3**:107-113.
12. Raicu, V., *et al.* (2008) Determination of two-photon excitation and emission spectra of fluorescent molecules in single living cells. *Proc. of SPIE* **6860**:686018- 686021.
13. Raicu, V., Jansma, D. B., Miller, R. J., and Friesen, J. D. (2005) Protein interaction quantified *in vivo* by spectrally resolved fluorescence resonance energy transfer. *Biochem. J.* **385**:265-277.
14. Zimmermann, T., Rietdorf, J., Girod, A., Georget, V., and Pepperkok, R. (2002) Spectral imaging and linear un-mixing enables improved FRET efficiency with a novel GFP₂-YFP FRET pair. *FEBS Lett.* **531**:245-249.
15. Epe, B., Steinhauser, K. G., and Woolley, P. (1983) Theory of measurement of Foster-type energy transfer in macromolecules. *Proc. Natl. Acad. Sci. USA* **80**:2579-2583.

Chapter 5. Biological system of interest

The *Pseudomonas aeruginosa* is a Gram-negative bacterium. Several virulence factors contribute to the pathogeny of this opportunistic pathogen, but lipopolysaccharide (LPS) is the main factor. LPS consists of lipid A, core oligosaccharide and O polysaccharide (O-PS) (1). The outer leaflet of the outer membrane of this bacterium contains two LPSs, the A and B bands (2). A-band LPS, associated with chronic infections, differs from B-band LPS in its O-PS composition (1). The transmembrane protein, Wzm, and the nucleotide binding protein, Wzt, together form an ABC transporter, Wzm-Wzt, in this bacterium. This transporter translocates the A-band polysaccharides, synthesized in the cytoplasm, across the inner membrane and thus plays an important role in the biosynthesis of A-band LPSs. In this chapter, we present a brief overview of structure of *Pseudomonas aeruginosa*, which is also our biological system of interest. Next, we describe the general architecture and the mechanism underlying the transport of substances through an ABC transporter. The quaternary structure of the Wzm-Wzt transporter is presented in detail in chapter 6.

5.1 *Pseudomonas aeruginosa*

Pseudomonas aeruginosa is an opportunistic rod shaped bacterium found on moist natural environments such as soil and water lakes, streams, rivers, other fresh waters, fresh fruits and vegetables, and hot tubs. In addition, it is also found on healthcare/therapy environments such as respiratory therapy equipment, dialysis tubing, and respiratory devices. This bacterium does not retain crystal violet dye in the Gram

staining protocol, hence is a Gram-negative bacterium. The bacterium can grow on both aerobic and anaerobic conditions. *Pseudomonas aeruginosa* accounts for 10% of all hospital-acquired infections. *Pseudomonas aeruginosa* causes infections in immunocompromised individuals and those who are hospitalized. The infections that are commonly associated with this bacterium include urinary tract infections, ventilator-associated pneumonia, surgical site infection, ocular infections, respiratory infections, ear infections (external otitis, malignant external otitis), skin and soft tissue infections and burn sepsis. Individuals diagnosed with HIV/AIDS, cystic fibrosis, chemotherapy-related neutropenia, and diabetes are at high risk of acquiring an infection and developing complications.

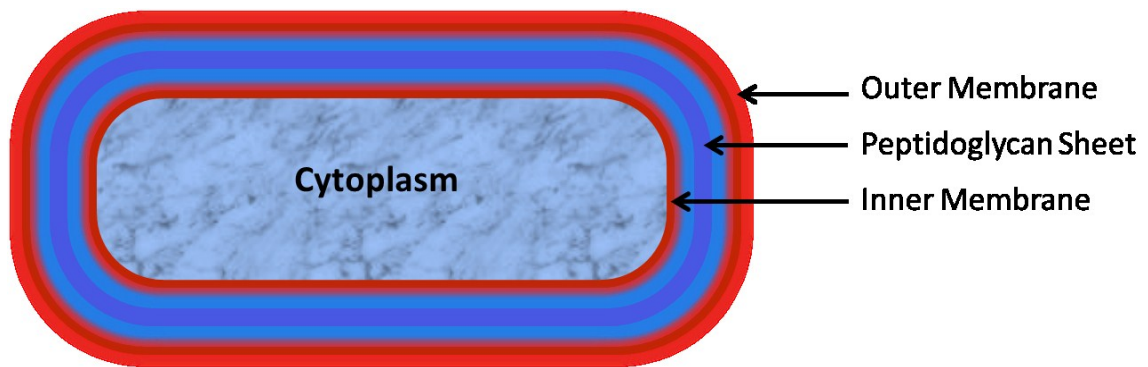


Figure 5.1: Outline of the Gram-negative bacterium. The cell membrane of this bacterium surrounding cytoplasm consists of the inner membrane, outer membrane and a peptidoglycan sheet between the inner and outer membrane.

In *Pseudomonas aeruginosa*, the cell wall is composed of the inner membrane, a single layer of peptidoglycan and the outer membrane as shown in Fig.5.1. The region between the inner membrane (cytoplasmic membrane) and the outer membrane is called the periplasm. The outer membrane of Gram-negative bacteria contains porins, which act

like pores for particular molecules. The outer leaflet of the outer membrane contains a unique component, lipopolysaccharide (LPS or endotoxin) (see Fig. 5.2), which is toxic to animals and is important for its structural integrity and survival. The pathogenicity of this Gram-negative bacterium is often associated with certain components of its outer membrane, in particular, the lipopolysaccharide (also known as LPS or endotoxin) on its outer leaflet. In humans, LPS binds the CD14/TLR4/MD2 receptor complex of leukocytes, which promotes the secretion of pro-inflammatory cytokines and immune system activation (3, 4). Cytokine production causes inflammation and can produce toxin in host.

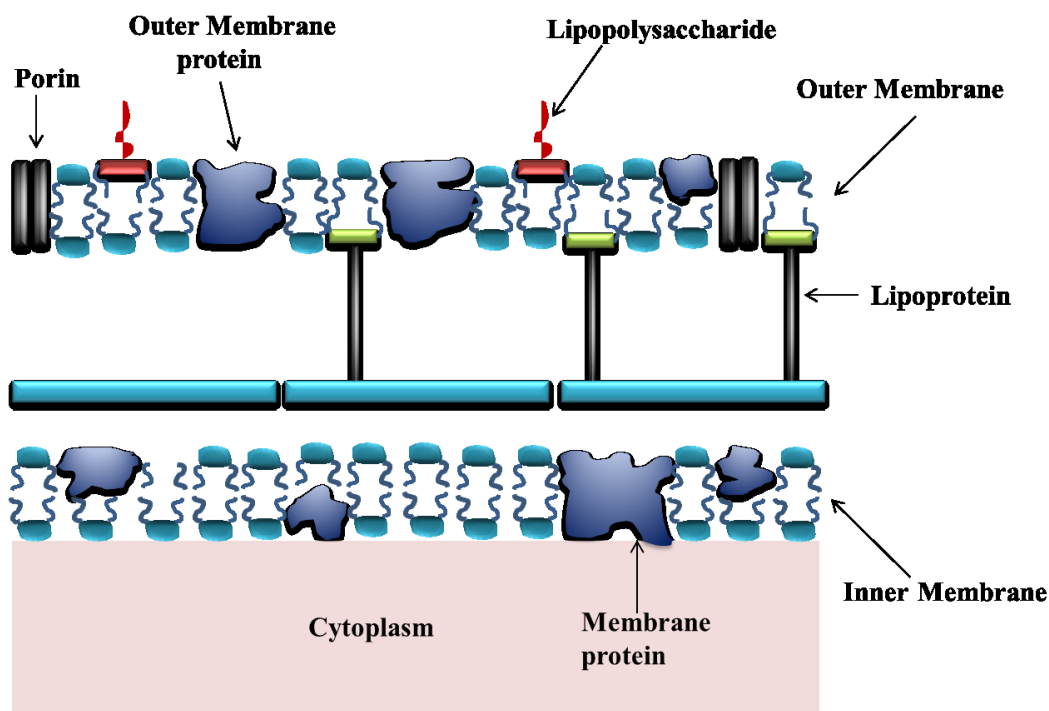


Figure 5.2: Cell membrane of the Gram-negative bacterium. The Gram-negative cell membrane consists of inner membrane and an outer membrane that is outside of the peptidoglycan layer. Lipoprotein molecules hold the peptidoglycan sheet to the outer membrane of the bacterium. This figure is adapted from (<http://textbookofbacteriology.net>).

The synthesis of polysaccharide (PS) starts on the cytoplasmic side of the inner membrane of the bacterium. These PSs are of two types: the A-band PS and B-band PS. The B-band PSs are translocated to the periplasmic face by Wzx (5). In the case of A-band PSs, they are translocated to the periplasm by Wzm and Wzt proteins that form an ABC transporter (6-8) (see Fig. 5.3). The synthesis of lipid A and core oligosaccharide portion of LPS occurs separately. The biosynthesis pathways of PSs, lipid A and core oligosaccharide merge at the periplasmic side of inner membrane to form LPSs. The LPS molecules are subsequently transported across the periplasm and finally to the outer membrane by the other proteins found in its outer membrane.

If endotoxin, LPS, enters the circulatory system, it reacts with the immune system of the body and releases inflammatory substances in the blood. Hence, the host experiences high temperature, high respiration rate, low blood pressure, loss in appetite and physical depression. This may lead to endotoxin shock, which may be fatal. The outer membrane of this bacterium protects the bacteria from several antibiotics, dyes, and detergents that would normally damage the inner membrane. Most gram-negative bacteria are naturally resistant to lysozyme and penicillin because these drugs can't penetrate to the outer membrane of these bacteria. Hence, alternative medicines such as lysozyme with EDTA and the antibiotic ampicillin have been developed to combat the protective outer membrane of pathogenic Gram-negative bacterium. Other drugs that can be used are chloramphenicol and streptomycin.

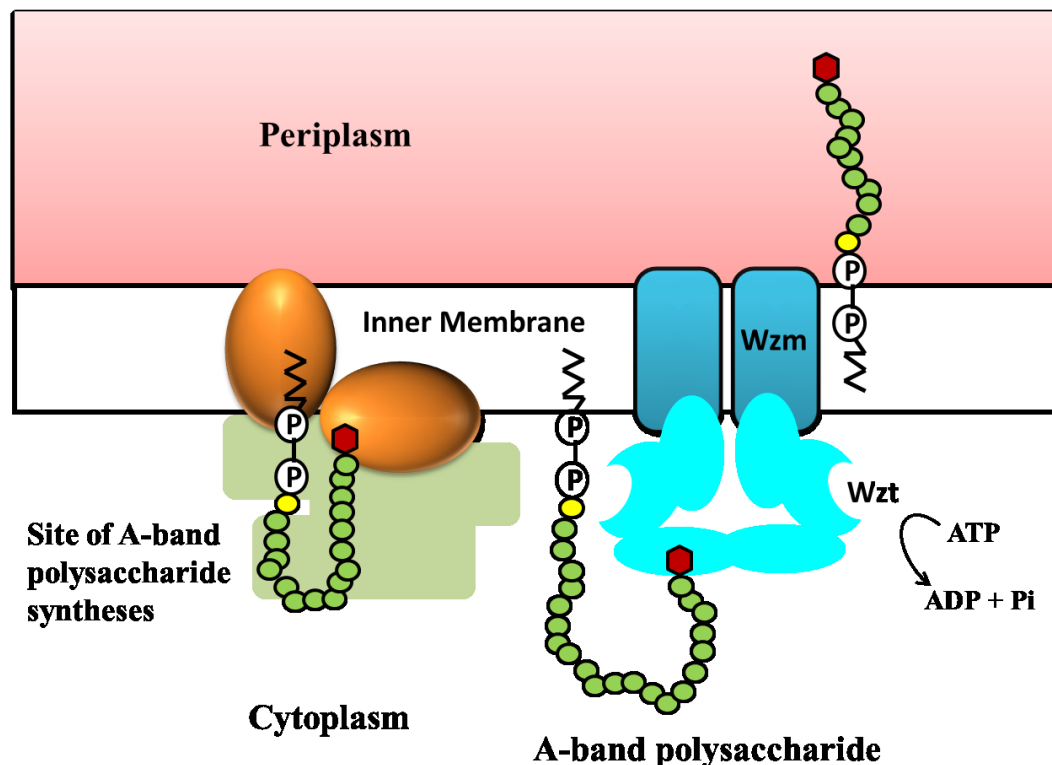


Figure 5.3: Cartoon depicting the bio-synthesis of A-band PS. The synthesized A-band PS is then translocated to the periplasm via an ABC transporter consisting of Wzm and Wzt protein. Here, Wzm and Wzt are depicted as dimers. This is just for illustration. The real squaternary structures of these proteins are determined in chapter 6. This figure is adapted from (9).

5.2 ATP-binding cassette (ABC) transporters

ATP-binding cassette (ABC) transporters are the largest and most important family of membrane transport proteins and are found across species from prokaryote to humans (10). ABC transporters consists of a highly conserved ATP-binding cassette (ABC) domain which are also called as nucleotide binding domain (NBD) and a less conserved transmembrane domain (TMD). To translocate the substrates across the cell membrane,

the cells require energy and hence ABC mediated transport is an example of active transport. ATP binds the NBD domain (approximately two hundred amino acid residues) and energy is released through the hydrolysis of ATP. These proteins use the released energy to accomplish diverse biological processes in the cell. In bacteria, TMDs and NBDs are expressed in separate polypeptides, while in many eukaryotes both domains are expressed in single polypeptide (11). Many ABC transporters are medically relevant. For example, the function of cystic fibrosis transmembrane conductance regulator (CFTR), which represents the molecular basis of cystic fibrosis is disrupted (12) due to mutation.

ABC transporters translocate a wide variety of substrates ranging from small ions to macromolecules across the cell membrane. Importers are mainly found in bacteria. Eukaryotes do not possess importers. ABC import systems are mainly involved in nutrient transport in bacteria. In contrast, the extrusion of noxious substances, the export of extracellular toxins and the targeting of membrane components are accomplished by ABC export systems. They are found in all living organisms and in general the TMD is fused to the ABC domain in a variety of combinations.

The mechanism of ABC transporter begins with the binding of the substrate with the transporter. The importers in Gram-negative bacteria, which deliver the substrate to the periplasmic side of the outer membrane, require a periplasmic binding protein (13),

whereas the exporters recruit their substrates from the cytoplasm. As soon as the substrate binds the transporter, the affinity for ATP binding on the nucleotide hydrolysis site increases. It is a prerequisite for the productive transport cycle. The two ABC cassettes then carry out highly cooperative ATP-binding and hydrolysis reactions (see Fig. 5.4). The energy released in this process causes conformational changes in the membrane spanning domain to facilitate the substrate translocation. These changes are believed to occur at the domain interface through a tailored pathway. After the substrate has crossed the membrane, the transporter returns to its original state through the association of ADP and phosphate.

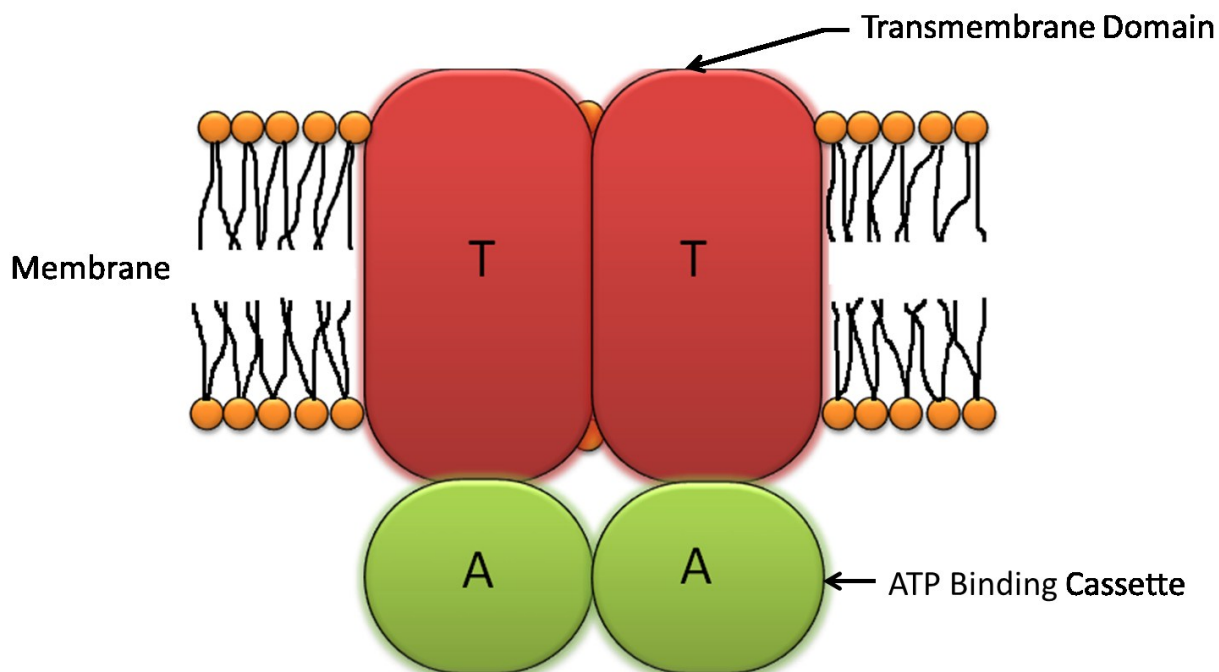


Figure 5.4: Schematic of an ABC transporter. This transporter consists of two transmembrane domain (TMD) and two ABC domain or NBD found in most of the transporters. The transporters are required to translocate the substrates across the cell membrane in many biological processes. This figure is adapted from Locher et al. (14).

The transporters MDR1 and MRP1 were investigated using electron microscopy (15) in cellular lipid environment and hence are expected to capture the physiologically relevant assembly of an ABC transporter. However, the resolution in this study was insufficient to capture the details of the domain arrangement. The crystal structure of another ABC transporter, BtuCD, which is responsible for vitamin B12 intake in *E. coli* was determined at 3.2 Å resolution by Locher et al. (14). This transporter works as a model system for other transporters and is depicted in Fig.5.3. Despite these advances in characterization of ABC transporters, there are many questions which need attention to fully understand the mechanism of the ABC transporters. These are: (i) What is the quaternary structure of ABC transporters *in vivo*? (ii) How do the ABC cassettes interact in the fully assembled ABC transporter? (iii) What does the translocation pathway of the substrate look like through an ABC transporter? (iv) What conformational changes are involved in coupling ATP hydrolysis to transport across the membrane?

Wzm and Wzt protein together constitute the ABC transporter in the Gram-negative bacterium *Pseudomonas aeruginosa*, described in the previous section. This transporter is responsible for translocation the A-band PS synthesised in the cytoplasm of this bacterium and thus is an important pathway of the biosynthesis of A-band LPS, an endotoxin. This dissertation describes a method based on FRET in conjunction with spectrally resolved two-photon microscope to determine the stoichiometry and the quaternary structure of dynamic complexes, which is used to determine the quaternary structure of Wzm-Wzt transporter in living cells and described in detail in chapter 6.

References

1. King, J. D., Kocincova, D., Westman, E. L., and Lam, J. S. (2009) Review: Lipopolysaccharide biosynthesis in *Pseudomonas aeruginosa*. *Innate Immun.* **15**:261-312.
2. Rocchetta, H. L. and Lam, J. S. (1997) Identification and functional characterization of an ABC transport system involved in polysaccharide export of A-band lipopolysaccharide in *Pseudomonas aeruginosa*. *J. Bacteriol.* **179**:4713-4724.
3. Scott, M. J. and Billiar, T. R. (2008) beta 2-Integrin-induced p38 MAPK Activation Is a Key Mediator in the CD14/TLR4/MD2-dependent Uptake of Lipopolysaccharide by Hepatocytes. *J. Biol. Chem.* **283**:29433-29446.
4. Triantafilou, M., *et al.* (2008) Chemokine receptor 4 (CXCR4) is part of the lipopolysaccharide "sensing apparatus". *Eur J Immunol* **38**:192-203.
5. Reeves, P. R., *et al.* (1996) Bacterial polysaccharide synthesis and gene nomenclature. *Trends Microbiol.* **4**:495-503.
6. Hug, I. and Feldman, M. F. (2011) Analogies and homologies in lipopolysaccharide and glycoprotein biosynthesis in bacteria. *Glycobiology* **21**:138-151.
7. Abeyrathne, P. D., Daniels, C., Poon, K. K., Matewish, M. J., and Lam, J. S. (2005) Functional characterization of WaaL, a ligase associated with linking O-antigen polysaccharide to the core of *Pseudomonas aeruginosa* lipopolysaccharide. *J. Bacteriol.* **187**:3002-3012.
8. Nagao, K., Kimura, Y., Mastuo, M., and Ueda, K. (2010) Lipid outward translocation by ABC proteins. *FEBS Lett.* **584**:2717-2723.
9. Cuthbertson, L., Kimber, M. S., and Whitfield, C. (2007) Substrate binding by a bacterial ABC transporter involved in polysaccharide export. *Proc. Natl. Acad. Sci. USA* **104**:19529-19534.
10. Oldham, M. L., Davidson, A. L., and Chen, J. (2008) Structural insights into ABC transporter mechanism. *Curr. Opin. Struct. Biol.* **18**:726-733.
11. Igarashi, Y., Aoki, K. F., Mamitsuka, H., Kuma, K., and Kanehisa, M. (2004) The evolutionary repertoires of the eukaryotic-type ABC transporters in terms of the phylogeny of ATP-binding domains in eukaryotes and prokaryotes. *Mol. Biol. Evol.* **21**:2149-2160.
12. Sheppard, D. N., *et al.* (1993) Mutations in CFTR associated with mild-disease-form Cl⁻ channels with altered pore properties. *Nature* **362**:160-164.
13. Quioco, F. A. and Ledvina, P. S. (1996) Atomic structure and specificity of bacterial periplasmic receptors for active transport and chemotaxis: variation of common themes. *Molecular Microbiology* **20**:17-25.
14. Locher, K. P., Lee, A. T., and Rees, D. C. (2002) The *E. coli* BtuCD structure: a framework for ABC transporter architecture and mechanism. *Science* **296**:1091-1098.
15. Rosenberg, M. F., *et al.* (2001) The structure of the multidrug resistance protein 1 (MRP1/ABCC1) - Crystallization and single-particle analysis. *J. Biol. Chem.* **276**:16076-16082.

Chapter 6. Quaternary structure of the Wzm-Wzt ABC transporter

ATP-binding cassette (ABC) transporters form a superfamily of membrane transport proteins that is common to all living organisms (1). As described in chapter 5, ABC transporters translocate molecules across the cell membrane by utilizing energy released through the hydrolysis of ATP. In general, it is assumed that the core of an ABC transporter consists of two transmembrane domains (TMDs) and two or more nucleotide-binding domains (NBDs) (2-4). TMDs form the translocation pathway for transporting substrate across the membrane, while the NBDs are involved in ATP binding and hydrolysis and contain the conserved ABC sequence motifs.

Pseudomonas aeruginosa coexpresses two unique forms of lipopolysaccharide (LPS) on the outer leaflet of its outer membrane, the common antigen A-band LPS and serologically variable O antigen B-band LPS (5). For both forms, polysaccharides (PSs) initially synthesized in the cytoplasm have to be translocated to the periplasm prior to reaching their final destination, the outer leaflet of the outer membrane, to form LPSs. The B-band PSs are translocated to the periplasmic face by Wzx (6). The TMD protein Wzm and the NBD protein Wzt form a bi-component ABC transporter (7-9) in this bacterium that translocates A-band PSs (5) to the periplasm. Genetic studies showed that the disruption of either the *wzt* or *wzm* gene hinders PS export across the inner membranes, resulting in accumulation of only the A-band PS in mutants' cytoplasm (10). In homology to other bacterial systems, Wzt has one NBD located at its N terminus,

while the PS binding site is thought to be located at its C terminus (11, 12). Wzm is thought to provide a passage for PS during the translocation.

As we have seen in chapter 5, *Pseudomonas aeruginosa* affects patients with cystic fibrosis and immunocompromised individuals (13, 14). The LPSs represent one of the main virulence factors which contribute to its pathogenicity (15, 16). The exact mechanism of PS export by ABC transporters is still unknown (7, 15), and the difficulty can be traced back to the difficulty of determining the spatial assembly of subunits into functional ABC transporters.

Advances in the FRET stoichiometry theory (17) together with the advent of optical micro-spectroscopy technology has led to the development of a FRET imaging method for the determination of the stoichiometry and relative disposition of the protomers (i.e., quaternary structure) within a protein complex in living cells (18). In contrast to standard average-based methods, this method relies on the analysis of distributions of apparent FRET efficiencies, E_{app} , across the image pixels of individual cells expressing proteins of interest. The most probable quaternary structure of the complex is identified from the number of peaks in the distribution of FRET efficiencies and their mutual relationships. Such peaks collectively create a unique fingerprint of a specific oligomer (quaternary) structure (19), or a “FRET spectrum” of the complex.

In our investigations of various oligomeric proteins, we have observed that although the E_{app} distributions of most cells expressing dynamic protein oligomers may

present single peaks, the FRET efficiency values corresponding to the maxima of those peaks do not take on arbitrary values, but cluster themselves about certain values, with each value corresponding to a single donor/acceptor configuration within an oligomer. Based on this observation, we used our *FRET spectrometry* method to determine the quaternary structure of the Wzm and Wzt homo-oligomers separately as well as that of their functional hetero-oligomer, the *P. aeruginosa* ABC transporter. Using CHO cells as a very competent medium for expression of an ABC transporter, in this chapter, we show that Wzt forms a rhombus-shaped homo-tetramer, which changes its shape into a square upon co-expression with Wzm. In its turn, Wzm forms a square-shaped homo-tetramer whose geometry remains unchanged upon co-expression with Wzt. Based on these observations we propose two slight variations of a hetero-octameric model of the quaternary structure of the Wzm-Wzt transporter from *P. aeruginosa*.

6.1 Experimental procedure

6.1.1 Gene cloning and plasmid constructs

To construct pcDNA3.1 (+) *gfp2-wzm*, pcDNA3.1 (+) *yfp-wzm*, pcDNA3.1 (+) *gfp2-wzt*, and pcDNA3.1 (+) *yfp-wzt*, the plasmids pcDNA3.1 (+) *gfp2-M2* and pcDNA3.1 (+) *yfp-M2* (i.e., *gfp2* or *yfp* fused to human muscarinic acetylcholine receptor gene M2, with alpha7 membrane signal peptide from nicotinic receptor) (a gift from Professor James W. Wells, University of Toronto), were used in inverse PCR reactions to remove the M2 gene (leaving the alpha7 signal peptide) by using the following two primers: 5`- AAC ATG GGC GCT ACA AGG TAA TCT AGA GGG CCC- 3` and 5`- CTT GTA CAG CTC GTC CAT GCC GAG CGT GAT CCC G- 3`. The *wzm* gene was PCR-amplified from *Pseudomonas aeruginosa* genomic DNA (*P. aeruginosa* PAO1 strain was a gift

from Professor Robert E. W. Hancock, University of British Columbia). The PCR primers are the following: 5`- /Phos/ ATG CTT CTT GGC TTG TCT CGT TCC TTG TGG GGC- 3` and 5`- ATC CGG TCT AGA CTA GAG TTC ATC CAC CAT TTC-3`. Also, the *wzt* gene was PCR-amplified from genomic DNA with the following two primers: 5`- /Phos/ ATG GGA CAG ATA CGC GTA TCC GGC CTC GGC AAG G - 3` and 5`- GGG CCC TCT AGA TCA TGG AGT GCT CTC CGC GGA AGT G -3`. Underlined sequences represent the XbaI sites. All PCR products were gel purified (Qiagen), digested with XbaI, and then gel purified and ligated to produce the desired plasmids. pcDNA3.1 (+) *gfp2-wzt*, pcDNA3.1 (+) *yfp-wzt* plasmids were used in another inverse PCR to remove the alpha7 mammalian signal peptide by using the following primers: 5`- /Phos/ AAG GGC GAG GAG CTG TTC ACC GGG GTG GTG CCC A-3` and 5`- /Phos/ GGC GGT ACC AAG CTT AAG TTT AAA CGC TAG CCA G-3`. Then, gel-purified PCR products were self-ligated to produce the desired plasmids.

To construct the untagged *wzm* gene in plasmid pcDNA3.1 (pcDNA3.1 (+)-*wzm*), pcDNA3.1 (+) *yfp-wzm* was used in an inverse PCR reaction to remove the *yfp* gene while leaving the signal peptide intact by using the following primers: 5`- /Phos/ GTA CAG CTT CCT TTG GAA CTC TCC TTG CAG GGA C-3`; and 5`- /Phos/ ATG CTT CTT GGC TTG TCT CGT TCC TTG TGG GGC-3`.

To construct the untagged *wzt* gene in plasmid pcDNA3.1 (pcDNA3.1 (+)-*wzt*), pcDNA3.1 (+) *yfp-wzt* was used in an inverse PCR reaction to remove the *yfp* gene by using the following primers: 5`- /Phos/ GGC GGT ACC AAG CTT AAG TTT AAA

CGC TAG CCA G-3'; and 5' - /Phos/ ATG GGA CAG ATA CGC GTA TCC GGC CTC GGC AAG G-3'. All engineered plasmids were checked by DNA sequencing.

6.1.2 Expression of fluorescently-tagged Wzm and Wzt in mammalian cells

The fusion proteins GFP₂-Wzm, GFP₂-Wzt, YFP-Wzm and YFP-Wzt were transiently expressed in CHO cells, singly or in combination, by transfection with pcDNA3.1 (+) *gfp2-wzm*, pcDNA3.1 (+) *yfp-wzm*, pcDNA3.1 (+) *gfp2-wzt*, or pcDNA3.1 (+) *yfp-wzt* using Lipofectamine 2000 (Invitrogen, USA), according to the manufacturer's directions and as recently described by Pisterzi *et al.* (20). Briefly, CHO-S cells were maintained in DMEM with 10% fetal bovine serum and 1% non-essential amino acids. Cells were seeded in 6-well plates at approximately 40% confluency and cultured overnight. Plasmid DNA and Lipofectamine were diluted in Opti-MEM medium (Invitrogen, USA), then added to cells. We used 2 µg DNA for a single-plasmid transfection reaction and 1 to 4 µg of each plasmid in co-transfection reactions. Cells were cultured for 36 hours. The cell growth medium was removed and 250 µl of Opti-MEM was added to each well of the 6-well plates. For imaging and FRET analysis, the cells were manually removed from the dishes using cell scrapers. Control reactions included single-plasmid transfections and mock transfections (i.e., no DNA).

6.1.3 Optical micro-spectroscopy

Spectrally resolved fluorescence images were acquired at room temperature using a two-photon microscope with spectral resolution constructed in-house (18). The excitation light was provided by an ultrashort-pulse (modelocked) Ti: Sapphire laser (KM Labs,

Boulder, CO), running at 80 MHz, and tunable from ~750 to 820 nm. The laser light was focused with an infinity-corrected Plan Apochromat objective ($\times 100$ magnification, NA=1.4, oil immersion; Nikon Instruments, Melville, NY) and raster-scanned across the sample using galvanometric scanners (Nutfield Technology, Hudson, NH). A non-descanned detection scheme was used, in which the emitted fluorescence was projected through a transmission grating onto a cooled electron-multiplying CCD (EMCCD) camera with single-photon sensitivity (Andor, iXon 897). In this manner, full spectral information was obtained from each sample voxel on a time scale much shorter than that which would correspond to molecular diffusion. This is a critical feature when using a two-photon microscope for molecular imaging in live cells.

6.1.4 Selection of FRET pairs

GFP₂ was used as a donor of energy, since it has a single-photon excitation maximum at ~400 nm (21) and hence a two-photon excitation at ~800 nm (18). This choice matches perfectly the center wavelength of our Ti: Sapphire laser which was set to ~800 nm and a full-width half maximum (FWHM) of ~30 nm. In addition, GFP₂ (by contrast to the more popular variant eGFP) has a large Stokes shift, which allows one to avoid acceptor direct excitation in a FRET experiment. YFP was used as an acceptor, since its excitation spectrum overlaps perfectly with the donor emission (22). Moreover, YFP has a two-photon excitation maximum at ~1024 nm and it therefore cannot be directly excited by the laser light used to excite GFP₂. To prevent nonspecific oligomerization caused by the slight propensity of GFP variants to oligomerize, the A206K mutation (23) was included in our fluorescent protein sequences.

6.1.5 Emission spectra

CHO cells expressing either GFP₂-tagged or YFP-tagged proteins were placed on a microscope slide and covered with a cover slip. Spectral images of the GFP₂-expressing cells were obtained by using laser light with an average power of ~25 mW at the entrance of the microscope. Emission spectra obtained from several cells expressing GFP₂ were averaged and normalized with respect to their maximum emission intensities to obtain the normalized spectrum of the GFP₂ donor (D). To obtain the emission spectrum of YFP, CHO cells expressing YFP were excited with laser light with a red-shifted spectrum (centered about 820 nm) and twice the average power, which increased the excitation rate of YFP several-fold (24); this was necessary since YFP does not absorb efficiently at 800 nm. Spectral images were obtained from cells showing high levels of YFP expression (as judged from their overall emission). Since the emission intensities of the cells expressing YFP were much lower than those expressing GFP₂, the auto - fluorescence of the cells also contributed to the spectrum of the YFP which was observed in the lower wavelengths of the spectrum. To correct for this spurious contribution, the YFP spectrum was fitted to a sum of three Gaussians: a broad Gaussian corresponding to the cellular auto-fluorescence, as determined from mock-transfected cells, and two closely-spaced Gaussians corresponding to the maximum plus a shoulder normally seen in the spectrum of YFP. We corrected the YFP spectrum by subtracting the Gaussian which fits the auto-fluorescence part of the spectrum from the measured spectrum. The corrected YFP spectra were averaged over many cells expressing YFP, and the resulting spectrum was normalized with respect to its maximum emission intensity to obtain the normalized (or elementary) acceptor (A) spectrum.

6.1.6 Image analysis and FRET efficiency determination

CHO cells were transfected to co-express GFP₂-tagged and YFP-tagged proteins to determine whether they self-associate to form oligomers. Spectral images obtained from cells co-expressing GFP₂-tagged and YFP-tagged proteins were unmixed to obtain separate donor (denoted by k^{DA}) and acceptor (k^{AD}) images, as described in detail in chapter 4 or elsewhere (18, 22). The apparent FRET efficiency (E_{app}) distribution in a given optical section of the imaged cell was determined for each image pixel using k^{DA} and k^{AD} and the equation:

$$E_{app} = \left[1 + \frac{Q^A k^{DA} w^D}{Q^D k^{AD} w^A} \right]^{-1}, \quad (6.1)$$

where w^A and w^D are the integrals of the measured elementary spectra of A and D, respectively. Q^D and Q^A are the quantum yields of D and A, respectively (18, 19), and their values ($Q^D = 0.55$ and $Q^A = 0.61$) were obtained from the literature (21, 22). All the computations were performed using the Matlab program (The MathWorks, Inc., USA). Pseudo-FRET efficiencies for pixels showing only background noise were avoided by rejecting all the gray levels not exceeding a value of 2.5% of the maximum emission intensity in the E_{app} calculations.

6.1.7 Distributions of FRET efficiencies

The number of image pixels that fell into a particular range of E_{app} values was plotted against the corresponding E_{app} values to obtain the distribution of FRET efficiencies in the cell, which is referred to here as “the E_{app} histogram.” About 90% of the cells showed single peaks and the rest showed multiple peaks in their E_{app} histograms. The use of histograms for representing the FRET data allows one to discriminate between FRET

caused by specific interactions between the protein of interest and unwanted stochastic FRET that is caused by simple molecular agglomeration, if any (25). About 5% of all the imaged cells and for which E_{app} histograms were determined were not considered in our analysis. These fall into two categories. The cells in the first category, which represents a minute fraction of the cells not considered for analysis, showed single peaks in their histogram with their peak position occurring at very large values of E_{app} compared to the rest of the cells, and were therefore considered outliers. This occurred in cells that appeared to express unusually high concentrations of Wzt tagged with YFP. We believe this was caused by direct excitation with laser light. The second category of spurious signals came from cells with emission intensities that exceeded the threshold value of 2.5% of the maximum intensity for those individual cells, but their overall intensities were barely exceeding the background noise level. Subsequent analysis of the histograms that passed all the quality checks was dependent on whether they showed single or multiple peaks, and was performed as described in the next section.

6.1.8 Estimation of the protein expression level

From the fluorescence of the donor in the presence of acceptor (k^{DA}) and the fluorescence of acceptor in the presence of donor (k^{AD}), we computed the fluorescence of the donor in the absence of acceptor using the formula $F^D = k^{DA}w^D + k^{AD}w^A Q^D / Q^A$, where all the symbols are as defined above. Then we calculated the average donor fluorescence in the absence of FRET. In order to obtain an order of magnitude estimate of the donor concentration inside the cells, we used the following expression, derived from the expression for the number of photons generated by a two-photon absorption process (24):

$$C_x = C_s \frac{F^x \sigma_s Q_s t d_s P_s^2 f_x \tau_x \lambda_x}{F^s \sigma_x Q_x t d_x P_x^2 f_s \tau_s \lambda_s}, \quad (6.2)$$

where C is the molar concentration, F is the average fluorescence intensity of the donors in the absence of energy transfer, σ is the two-photon absorption cross-section, Q is the quantum yield, td is the pixel dwell time of the scanning system, P is the average excitation light power, f is the repetition rate of the laser pulse, τ is the laser pulse duration (of the order of 10 to 100 fs), and λ_{ex} is the excitation wavelength, while the subscripts s and x stand for standard solution and for the unknown concentration (of donor-tagged molecules). The average fluorescence intensity of a fluorescent standard consisting of an aqueous solution of YFP (10 μ M concentration) was determined using a separate Zeiss Axio Observer (Zeiss, Thornwood, NY) microscope equipped with an OptiMiSTM module (Aurora Spectral Technologies, Bayside, WI) and an ultrashort-pulse laser (MaiTaiTM, Spectra Physics, Santa Clara, CA) tuned to 960 nm. The solution of YFP was prepared as described elsewhere (26). The absorption cross sections and the quantum yields were obtained from the literature (27, 28).

6.1.9 Analysis of E_{app} histograms

Of all the cells analyzed that co-expressed either GFP₂-Wzt and YFP-Wzt or GFP₂-Wzm and YFP-Wzm, a large majority (see Results section) exhibited single peaks located at various positions along the horizontal axis (i.e., E_{app}), while some showed multiple, and often overlapping peaks in their E_{app} histograms. The E_{app} distributions for cells presenting only one peak were fitted to single Gaussian functions. Some cells, which presented broad E_{app} distributions with dominant peaks, were also considered for analysis, with their dominant peaks fitted to Gaussian functions. The peak positions from

individual histograms were binned and collected in “meta-histograms” representing the total number of peak positions obtained for each E_{app} value (in intervals of 0.02). The five or three clearly distinct peaks in the meta-histograms (see for instance Figs. 6.3C and 6.4C) were simulated using five or three Gaussian functions respectively, with the location on the horizontal axis of their maxima predicted by either a rhombus-shaped tetramer model (as depicted in, e.g., Fig. 6.3D) or a square tetramer (see Fig. 6.4D). Details about the derivations of the expressions for the peak positions for these models are given elsewhere (18, 19). The fitting of the simulated curves to the experimental ones consisted of minimizing the mismatch between experimental and simulated data by adjusting a number of parameters, as described next.

(i) The exact value of the pair-wise FRET efficiency (E_p), which determines the position of all peaks in a histogram (according to expressions given in Figs. 6.3D and 6.4D), depends on the distance between individual donors and acceptors within the protein complex, relative to the magnitude of the Förster radius corresponding to the FRET pair used. E_p was therefore considered to be an adjustable parameter in the data fitting process, which determined the positions of all five Gaussians predicted by the rhombus-shaped tetramer model (Fig. 6.3D) or all three Gaussians predicted by the square-shaped tetramer model (Fig. 6.4D).

(ii) The width of each Gaussian in the meta-histograms accounts for variations from cell to cell due to pH, viscosity, or other factors that may alter the properties of the fluorescent probes and their rotational diffusion rates; the widths of the individual peaks

in the meta-histogram were therefore adjusted independently of each other in the fitting process.

(iii) Finally, the amplitudes of the peaks depend on the number of instances each donor-acceptor configuration is observed in all the cells. For a large population of cells imaged, the average D to A concentration ratio should approach unity if the transfection ratio varies randomly from cell to cell. This would allow one to control the amplitudes for each of the individual peaks in the meta-histogram. However, it is entirely likely that we systematically underestimated instances when high FRET efficiency values were present in individual E_{app} histograms, due to the fact that peaks corresponding to higher values of FRET efficiencies were usually broader and had lower amplitudes, which may have caused them to be masked by peaks corresponding to lower values of FRET efficiencies. Therefore, the peak amplitudes were used as independently adjustable parameters, and no significance was ascribed to them in the present analysis.

6.2 Results

6.2.1 Cytoplasmic Wzt and membrane-bound Wzm interact at the plasma membrane

From many bioinformatics servers, including NCBI (ncbi.nlm.nih.gov) and ExPASy (expasy.org), we found that the Wzm and Wzt proteins possess no domains or motifs that can be targeted for modification by eukaryotic cellular machinery or exhibit any signal for organelle localization. Hence, we chose Chinese hamster ovary (CHO) cells as a model system to study the interaction of Wzm and Wzt proteins. CHO cells are readily transfected to transiently express proteins of interest using standard techniques in the

absence of PS. Moreover, the significantly larger size of CHO cells compared to most bacteria makes them suitable for pixel-level FRET studies.

Before probing the quaternary structure of Wzm and Wzt, we wanted to confirm their cellular localization. We fused the fluorescent protein GFP₂ (21) to their N termini and expressed them individually in CHO cells, which were then subjected to two-photon excitation using our home-made two-photon microscope with spectral resolution (or optical micro-spectroscopy system) (18). Fluorescent images of different optical sections of the CHO cells expressing GFP₂-Wzm or GFP₂-Wzt fusion proteins were collected at ~508 nm, the wavelength at which the intensity of the GFP₂ emission spectrum is at its maximum (Fig. 6.1). The consecutive sections of these cells are 3 μm apart (i.e., close to the limit of the axial resolution of the two-photon microscope). The fluorescence in the CHO cell expressing GFP₂-Wzm originates mainly from annular regions, consistent with the localization of this protein at the level of the plasma membrane (Fig. 6.1, upper panels), while the fluorescence in the CHO cell expressing GFP₂-Wzt is distributed throughout the cytoplasm (Fig. 6.1, bottom panels). The dark pockets in some sections are probably the organelles of CHO cells that are voiding the fluorescence. From these images, we concluded that Wzm is targeted to the cellular membrane whereas Wzt localizes in the cytoplasm.

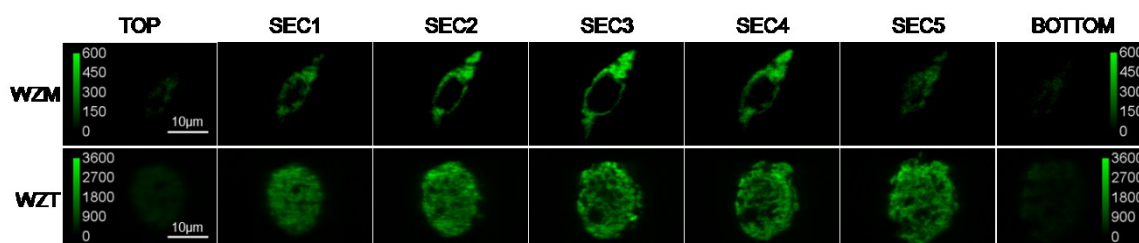


Figure 6.1: Localization of Wzm and Wzt proteins in optical sections of Chinese hamster ovary (CHO) cells as detected by a two-photon microscope with spectral resolution. The top row displays fluorescence images (at 508 nm) of seven sections from top to bottom of a CHO cell expressing Wzm protein fused to the green fluorescent protein variant GFP₂. The bottom row displays fluorescence images (at 508 nm) of sections, from top to bottom, of a CHO cell expressing Wzt protein fused to GFP₂. Consecutive sections of these cells were 3 μm apart, which is roughly within the axial resolution of the two-photon microscope. Vertical scale bar indicates fluorescence intensity, in arbitrary units.

In order to probe the mutual interaction of Wzm and Wzt, we expressed fusion proteins GFP₂-Wzm and YFP-Wzt – where YFP was the yellow variant of the green fluorescent protein GFP (29) – separately or in combination in CHO cells, and imaged them using a two-photon microscope with spectral resolution (18). The cells expressing only GFP₂-Wzm or only YFP-Wzt were imaged to obtain elementary spectra of GFP₂ and YFP, respectively. In the cells co-expressing both fusion proteins, GFP₂ (21) was directly excited by laser light and acted as a donor (D) of energy, while YFP (29) acted as an acceptor (A) in a FRET process (30-32) and was almost completely insensitive to excitation by laser light under the conditions that excite GFP₂. Spectral images obtained from cells co-expressing GFP₂-Wzm and YFP-Wzt were unmixed (see the experimental procedure section) to obtain the fluorescence of donors in presence of acceptors (k^{DA}) and the fluorescence of acceptors in presence of donors (k^{AD}). From k^{DA} and k^{AD} , the apparent FRET efficiency (E_{app}) for every image pixel was determined as described briefly in the experimental procedure section, and in more detail elsewhere (18, 22). Typical results shown in Fig. 6.2 indicate that Wzt and Wzm interact in living cells to form complexes at the plasma membrane, as evidenced by FRET occurring mostly at the plasma membrane but also in regions possibly occupied by intracellular membranes (such as the ER, Golgi,

and transport vesicles). Analysis of these data alone is insufficient to extract detailed structural information regarding the complexes. However, such data do provide critical evidence for the interaction between Wzm and Wzt at the level of the plasma membrane, which will be used below in elucidating the structure of the entire hetero-oligomer.

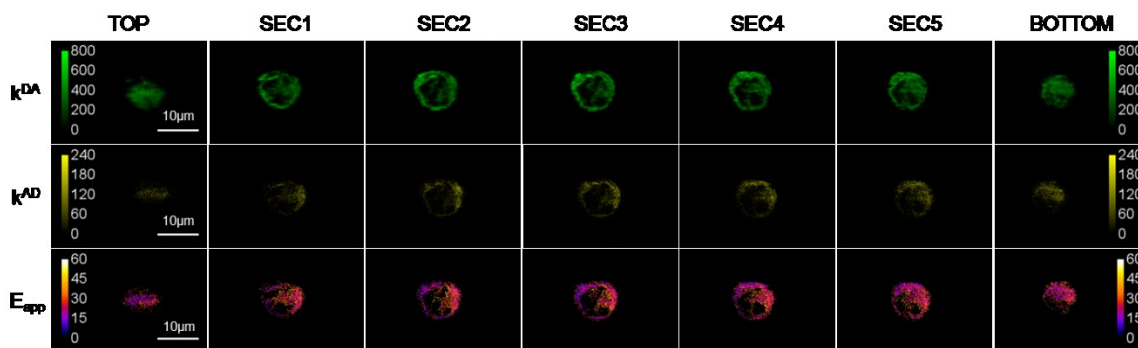


Figure 6.2: Mapping the spatial distribution of complexes of Wzm and Wzt proteins in thin ($3\mu\text{m}$) optical sections through a CHO cell co-expressing Wzm proteins tagged with GFP_2 as a donor, and Wzt proteins tagged with YFP as an acceptor. Two-dimensional spatial distribution maps of fluorescence of donors in presence of acceptors (k^{DA}) and the fluorescence of acceptors in presence of donors (k^{AD}) were obtained from spectral unmixing, while the apparent FRET efficiency (E_{app}) map was calculated from k^{DA} and k^{AD} for every pixel (see text for details).

6.2.2 The quaternary structure of Wzt in the absence of Wzm

CHO cells were transfected to express the fusion proteins $\text{GFP}_2\text{-Wzt}$ and YFP-Wzt , separately or in combination at varied plasmid ratios (i.e., $\text{GFP}_2\text{-Wzt}$ to YFP-Wzt in 3 to 1, 2 to 2 or 1 to 3 ratio), and imaged as described above. The apparent FRET efficiency (E_{app}) for every image pixel was determined and a distribution of FRET efficiencies (or the E_{app} histogram) for each cell imaged was obtained by plotting the number of pixels that fell into a particular range of E_{app} values against the corresponding E_{app} value (Fig. 6.3). Of all the cells co-expressing $\text{GFP}_2\text{-Wzt}$ and YFP-Wzt that were analyzed, roughly 90% exhibited single peaks located at various positions along the horizontal axis (i.e.,

E_{app}), while about 10% showed multiple peaks in their E_{app} histograms. The two-dimensional E_{app} maps for representative cells expressing Wzt proteins and their corresponding E_{app} distributions are shown in Fig.6.3A-B. The E_{app} distributions for cells presenting only one peak were fitted to single Gaussian functions. Some cells, which presented broad E_{app} distributions with dominant peaks, were also considered for analysis, with their dominant peaks fitted to Gaussian functions. The best-fit curves provided individual peak positions, that is, E_{app} values corresponding to the distribution maxima (Fig. 6.3B). The E_{app} distributions presenting multiple peaks were analyzed separately (see below).

Peak positions from single-peaked histograms acquired from 380 cells expressing Wzt in the absence of Wzm were binned and collected in “meta-histograms” representing the total number of peak positions obtained for each E_{app} value (in intervals of 0.02). As seen from Fig. 6.3C, the meta-histogram showed five distinct peaks, which means that the peak positions obtained for individual histograms did not vary over a continuum of E_{app} values but rather clustered around five distinct values each corresponding to a different tetrameric configuration in individual cells. The five peaks in the meta-histograms (Fig. 6.3C) were simulated using five Gaussian functions, with the location on the horizontal axis of their maxima accurately predicted by a rhombus-shaped tetramer model (18, 19) depicted in Fig. 6.3D. According to this model, the positions of all five peaks in the meta-histogram may be computed from a single E_{app} value, which is termed the “pair-wise FRET efficiency” (E_p) and, incidentally, corresponds to the second peak in the meta-histogram shown in Fig. 6.3C. (see Fig. 6.3D for mathematical expressions

corresponding to each peak position). The fitting process consisted of minimizing the mismatch between experimental and simulated data by adjusting E_p as well as the amplitudes and widths of the Gaussian functions. A detailed justification of this fitting approach is provided in the Experimental Procedures section above.

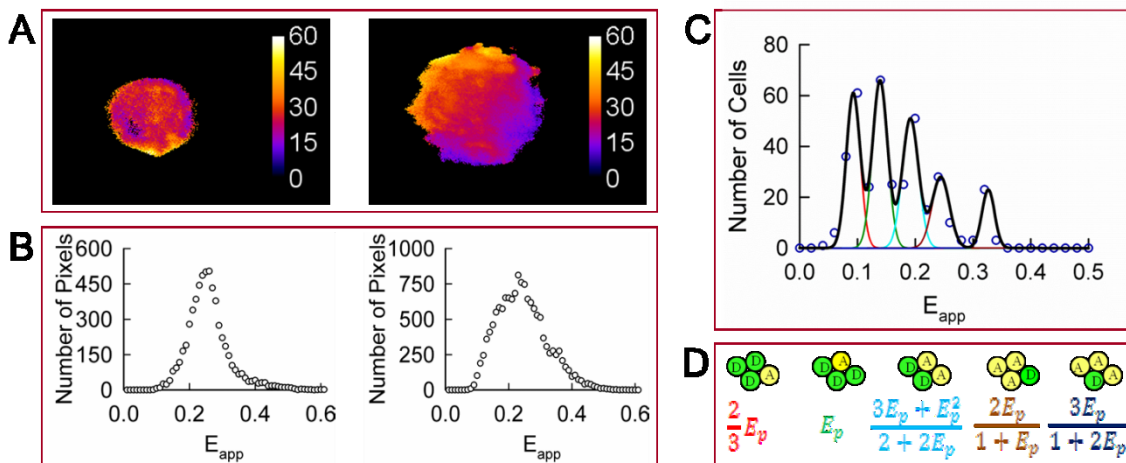


Figure 6.3: Homo-oligomerization of Wzt expressed in CHO cells in the absence of Wzm. A. Apparent FRET efficiency (E_{app}) maps of representative cells expressing Wzt. B. Distributions of FRET efficiencies (E_{app} histograms) across the pixels composing the FRET efficiency maps shown in panel A. C. The peak positions of 380 cells showing single or dominant peaks in their corresponding E_{app} histograms were binned and used to form meta-histograms (circles), and then fitted simultaneously to five correlated Gaussians shown individually (red, green, cyan, brown, and blue lines) or as a sum (black line). The five peaks in the meta-histogram correspond to different configurations of a rhombus-shaped tetramer shown in panel D. The peak positions of the five simulated Gaussians were determined from a single adjustable parameter, the pair-wise FRET efficiency (E_p) (see equations in panel D). The best fit was obtained for $E_p \pm$ S.D. equal to 0.139 ± 0.013 . D. A rhombus-shaped tetramer model used to interpret the results in panel C. E_p is the pair-wise FRET efficiency between a single donor (D) and a single acceptor (A).

6.2.3 The quaternary structure of Wzt in the presence of untagged Wzm

To investigate whether the presence of Wzm affects the stoichiometry and quaternary structure of Wzt, CHO cells were transfected to coexpress GFP₂-Wzt, YFP-Wzt and

untagged Wzm, and imaged to obtain E_{app} histograms for each cell. As in the experiments described above, the E_{app} histograms of about 90% of the cells showed single peaks, while the rest showed broader distributions. Typical results for cells expressing Wzt in the presence of untagged Wzm are presented in Fig. 6.4.

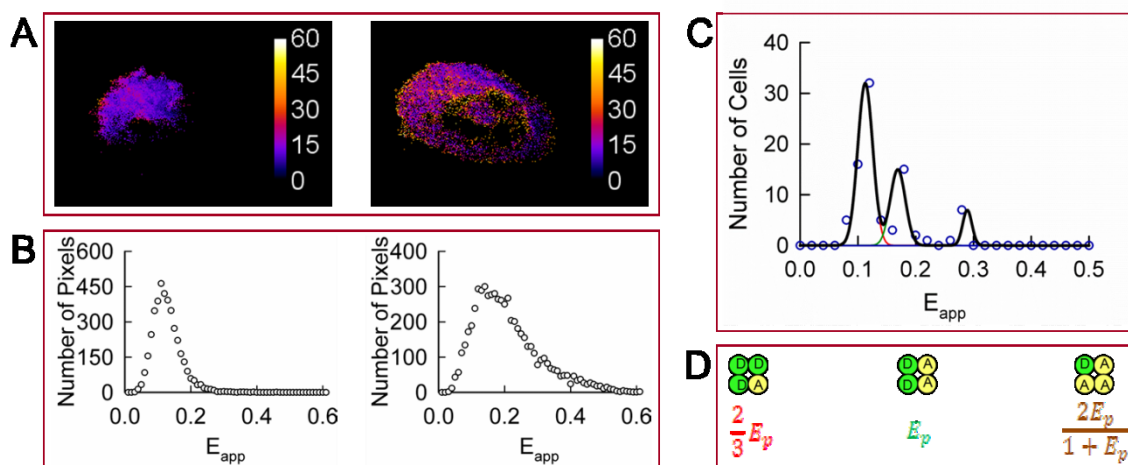


Figure 6.4: Homo-oligomerization of Wzt expressed in CHO cells in the presence of untagged Wzm. A. Apparent FRET efficiency (E_{app}) maps of representative cells expressing Wzt in the presence of Wzm. B. Distributions of FRET efficiencies (E_{app} histograms) across the pixels composing the FRET efficiency maps shown in panel A. C. Meta-histogram obtained by accumulating the peak positions of 87 cells presenting single or dominant peaks in their E_{app} distributions (circles) and theoretical best-fit to three correlated Gaussians shown individually (red, green, and brown lines) or as a sum (black line). The three peaks in the meta-histogram correspond to different configurations of a square-shaped tetramer shown in the same order in panel D. The best-fit was obtained for $E_p \pm$ S.D. equal to 0.17 ± 0.016 . D. Square-shaped tetramer model used to interpret the results in panel C. E_p is the pair-wise FRET efficiency between a single donor (D) and a single acceptor (A).

The peak positions for the singly-peaked histograms and broad histograms showing dominant peaks were collected, binned, and plotted against E_{app} . The meta-histogram thus obtained and its best-fit to a sum of three Gaussians are shown in Fig. 6.4C, while the three configurations of a square tetramer model used to simulate the

histogram are shown in Fig. 6.4D. In contrast to the model describing Wzt homooligomers in the absence of Wzm, the square-shaped tetramer correctly described this experimental meta-histogram.

6.2.4 The quaternary structure of Wzm in the absence or in the presence of untagged Wzt

To determine the quaternary structure of Wzm, CHO cells were transfected to express fusion proteins GFP₂-Wzm and YFP-Wzm in the absence or presence of untagged Wzt and were imaged to obtain pixel-level distributions of E_{app} for each individual cell. Here again, the E_{app} histograms of most cells expressing Wzm in the absence of Wzt presented single peaks, while some presented multiple peaks. Typical data for the cells expressing Wzm proteins are shown in Fig. 6.5. Tails towards high E_{app} values were seen in almost all the histograms, suggesting the presence of small and poorly defined peaks at high E_{app} values. The meta-histogram obtained by collecting and binning the peak positions of the single-peaked E_{app} histograms or the dominant peaks in broad and multi-peaked histograms and its theoretical best-fit to a sum of three Gaussians is shown in Fig. 6.5C. The peak positions of the individual Gaussians in the meta-histogram correspond to the apparent FRET efficiencies of different configurations of square-shaped tetramers as shown in Fig. 6.5D.

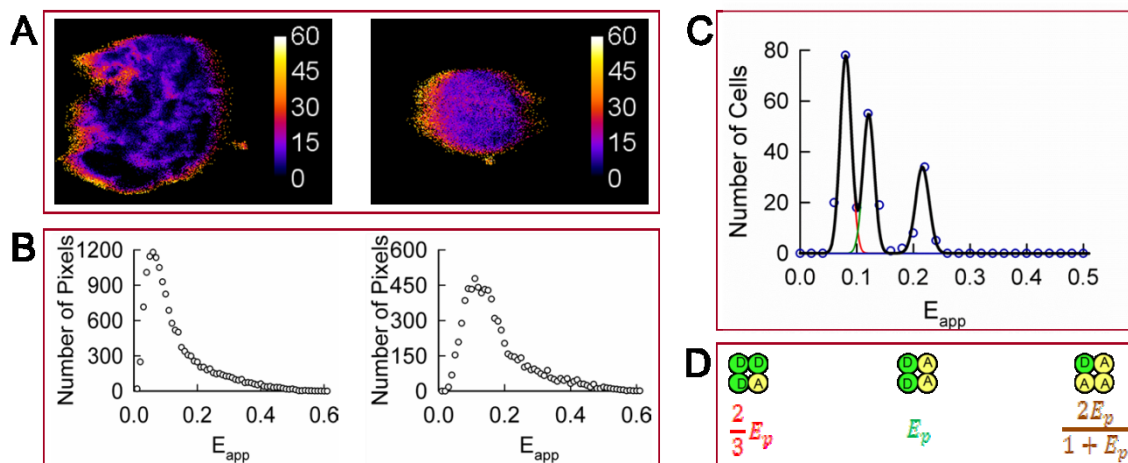


Figure 6.5: Homo-oligomerization of Wzm expressed in CHO cells in the absence of Wzt. A. Apparent FRET efficiency (E_{app}) maps of representative cells expressing Wzm. B. Distributions of FRET efficiencies (E_{app} histograms) across the pixels composing the FRET efficiency maps shown in panel A. Most histograms presented single peaks, although those with peaks at lower values also present tails at higher E_{app} values. C. Meta-histogram obtained from the peak positions of 240 cells presenting single or dominant peaks in their E_{app} distributions (circles) and their theoretical best-fit to three Gaussians shown individually (red, green and brown lines) or as a sum (black line). The three Gaussians correspond to different configurations of square-shaped tetramers shown in the same order in panel C. The best fit was obtained for $E_p \pm$ S.D. equal to 0.121 ± 0.010 . D. Square-shaped tetramer model and its corresponding expressions for FRET efficiencies used to interpret the results in panel C. E_p is the pair-wise FRET efficiency between a single donor (D) and a single acceptor (A).

Similarly, the Wzm oligomeric structure in the presence of Wzt was also investigated, and typical results are shown in Fig. 6.6. Analysis of the meta-histogram obtained from such cells revealed that Wzm forms square-shaped tetramers in the presence of untagged Wzt (Fig. 6.6C).

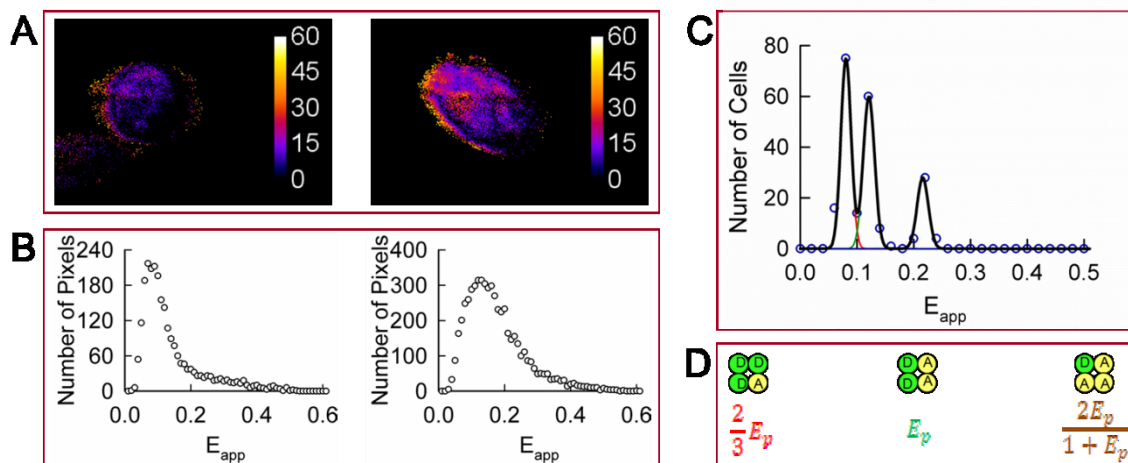


Figure 6.6: Homo-oligomerization of Wzm expressed in CHO cells in the presence of untagged Wzt. A. Apparent FRET efficiency (E_{app}) maps of representative cells expressing Wzm in the presence of Wzt. B. Distributions of FRET efficiencies (E_{app} histograms) across the pixels composing the FRET efficiency maps shown in panel A. The majority of cells presented single peaks, with minor tails at higher E_{app} values. C. Meta-histogram obtained from the peak positions of 210 cells presenting single or dominant peaks in their E_{app} distributions (circles) and theoretical best-fit to three correlated Gaussians shown individually (red, green and brown lines) or as a sum (black line). The three Gaussians correspond to different configurations of a square-shaped tetramer shown in the same order in panel D. The best-fit was obtained for $E_p \pm$ S.D. equal to 0.121 ± 0.010 . D. Square-shaped tetramer model and its corresponding expressions for FRET efficiencies used to interpret the results in panel C. E_p is the pair-wise FRET efficiency between a single donor (D) and a single acceptor (A).

6.2.5 Confirmation of the quaternary structure from analysis of cells presenting broad E_{app} distributions

Using either the rhombus-shaped tetramer or the square-shaped tetramer model, we simulated the distribution of FRET efficiencies for individual cells showing multiple peaks ($\sim 10\%$ of the total population of cells). The E_p values for individual cells were allowed to vary between E_p -S.D. and E_p +S.D. as determined from the meta-histogram analysis (Figs. 6.3C, 6.4C, 6.5C and 6.6C). The theoretical best-fits of the cells showing multiple peaks in their E_{app} distributions are shown in Fig. 6.7. The different Gaussians correspond to the different configurations of the tetramers depicted in Figs. 6.3D and

6.4D, respectively. Variations in the FRET efficiency due to the relative orientation of the donor and acceptor transition dipoles, as well as smearing of the FRET distributions due to the point spread function of the microscope, influence the width of individual Gaussians. Because of this, here again, the widths of the Gaussians were adjusted independently of each other in the process of data fitting. Following this procedure, an agreement between the quaternary structure models and the experimental results was obtained as follows: the rhombus-shaped tetramer for Wzt in the absence of Wzm (Fig.6.7A), and the square tetramer for Wzt in the presence of Wzm (Fig. 6.7B), Wzm in the absence of Wzt (Fig.6.7C), and Wzm in the presence of Wzt (Fig. 6.7D). This is similar to the results of the analysis of meta-histograms obtained from single-peaked histograms. As for the observation that the E_{app} histograms of most cells exhibited single peaks (corresponding to single combinations of donors and acceptors in the cell) while some exhibited multiple peaks (corresponding to multiple D-A combinations), an explanation will be attempted in the DISCUSSION section.

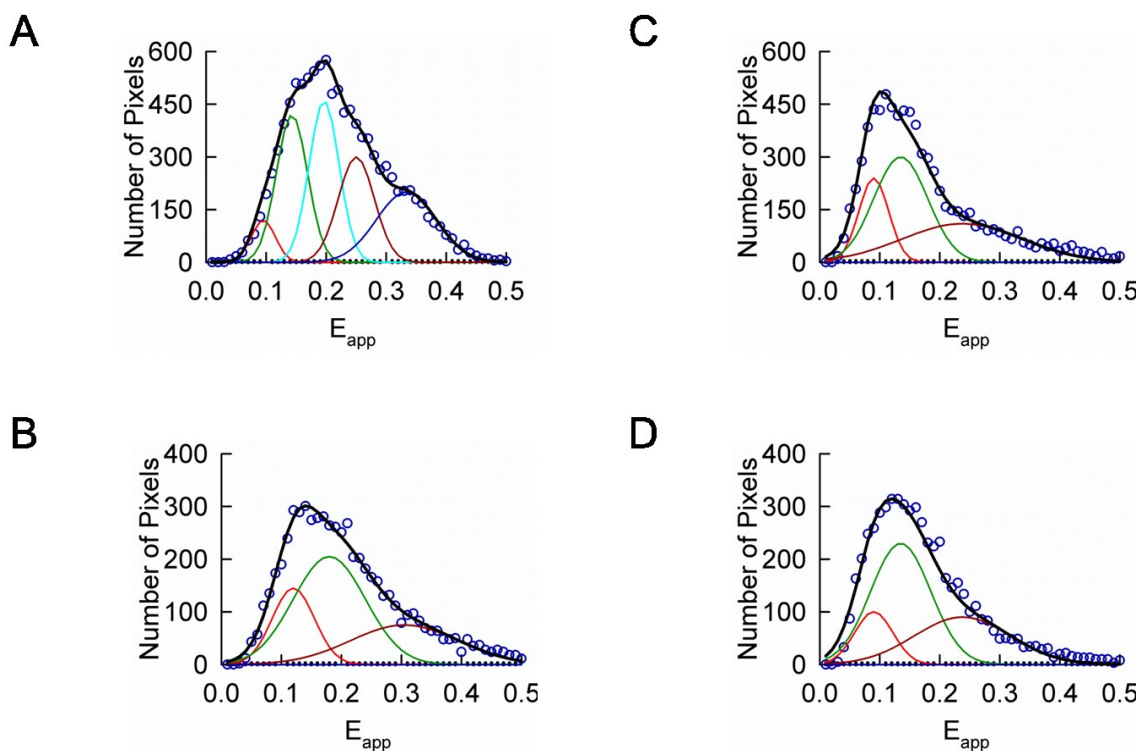


Figure 6.7: Determination of the quaternary structure of Wzt and Wzm expressed in CHO cells showing multiple peaks in their E_{app} histograms. A. E_{app} histogram of a cell expressing Wzt in the absence of untagged Wzm (circles) and theoretical best-fit (for $E_p = 0.143$) to five Gaussians shown individually (red, green, cyan, brown, and blue lines) corresponding to different configurations of the rhombus shaped tetramer shown in Fig. 6.3D or as a sum (black line). B. E_{app} histogram of a cell expressing Wzt in the presence of untagged Wzm (circles) and theoretical best-fit (for $E_p = 0.180$) to three Gaussians shown individually (red, green and brown lines) corresponding to different configurations of a square shaped tetramer shown in Fig. 6.4D or as a sum (black line). C. E_{app} histogram of a cell expressing Wzm in the absence of untagged Wzt (circles) and theoretical best-fit (for $E_p = 0.135$) to three Gaussians shown individually (red, green and brown lines) corresponding to different configurations of square shaped tetramer of Fig. 6.5D or as a sum (black line). D. E_{app} histogram of a cell expressing Wzm in the presence of untagged Wzt (circles) and theoretical best-fit (for $E_p = 0.135$) to five Gaussians shown individually (red, green and brown lines) corresponding to different configurations of square shaped tetramer of Fig. 6.6D or as a sum (black line).

6.2.6 Reliability of the pixel-level FRET method

As seen above, determinations of the quaternary structure of Wzt in the absence or presence of Wzm, and of that of Wzm in the absence or presence of Wzt were based primarily on FRET efficiency meta-histograms (obtained from the peak position of

single-peaked histograms or multi-peaked histograms exhibiting dominant peaks) and their best-fit to different theoretical models. Analysis of the smaller number of histograms presenting multiple peaks provided additional support to the quaternary structure model. Since all the results presented above relied heavily on the assumption that one peak in the meta-histogram corresponds to one oligomeric configuration, it was important to assess the validity of this assumption. To this end, we transfected CHO cells with plasmids encoding an artificial tetrameric construct consisting of three Venus molecules (a yellow variant of GFP, here serving as the FRET acceptor), and a Cerulean molecules (a cyan variant, here serving as the FRET donor); this construct is denoted herein by VCVV. The plasmids were a generous gift from Dr. Steven Vogel of NIH and were described and characterized in detail elsewhere (33). Analysis of cells expressing this construct was carried out the same way as for Wzm- and Wzt-expressing cells. As expected, the individual histograms of all cells expressing VCVV presented a single peak. By collecting and binning all those peaks, we obtained the meta-histogram shown in Fig. 6.8, which shows a clearly identifiable single peak. This is in agreement with our assumption that one tetrameric configuration corresponds to one peak in the meta-histogram, and demonstrates that our method of analysis does not introduce spurious peaks in the meta-histogram. We conclude that the multiple peaks obtained for Wzm and Wzt must indeed originate from different combinations of donors and acceptors within a rhombus- or square-shaped tetramer.

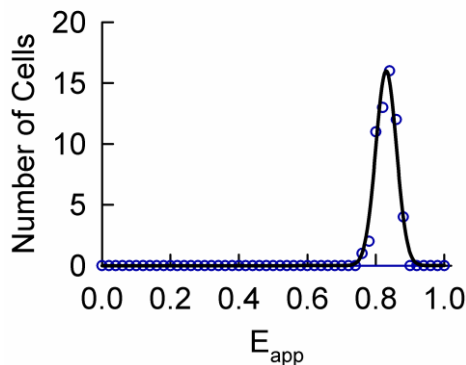


Figure 6.8: Meta-histogram obtained from peak positions of individual E_{app} histograms for CHO cells expressing an artificial tetramer (circles) consisting of three acceptors (Venus) and one donor (Cerulean) (33). The solid line represents the theoretical best-fit to a single Gaussian.

6.2.7 Order-of-magnitude estimate of the two hetero-tetramers concentration

Using a reference solution consisting of 10 μM YFP and the average fluorescence intensity of donors corrected for loss through FRET (F^D), we first estimated the molar concentrations for Wzm and Wzt separately. For, instance for the cells shown in Fig. 6.4 (for Wzt) and Fig. 6.6 (for Wzm), the molar concentrations of donor-tagged molecules were on the order of 10 nM. Then, using an approximate radius value of 10 μm for a CHO cell, we estimated the Wzm or Wzt concentrations to be on the order of a few hundred thousand molecules per cell. For all the cells imaged in this study, the numbers varied between a hundred thousand and one million molecules per CHO cell. For a *P. aeruginosa* cell, shaped as a rod of diameter of about 700 nm and length of 2 μm , this is the equivalent of a few tens to a few hundreds of molecules per cell. Given the quaternary structure of these proteins we just determined, we estimate the number of Wzt and Wzm tetramers to be on the order of a few to a few tens per cell.

6.3 Discussion

6.3.1 Why the individual histogram peaks are broader than those of meta-histograms

Visual comparison between the individual peaks in the meta-histograms shown in Fig. 6.3-6.6 and the individual peaks of the multi-peaked histograms (Fig. 6.7) revealed that the widths of the individual peaks in multi-peaked histograms were vastly wider than those of the meta-histograms. The width of each Gaussian in the meta-histograms accounts for variations from cell to cell due to pH, viscosity, or other factors that may alter the properties of the fluorescent probes and their rotational diffusion rates, while the distributions of E_{app} values accounting for the widths of the peaks in E_{app} histograms showing single peaks or individual peaks of E_{app} histograms showing multiple peaks were caused by two main factors: (a) changes in relative orientations of the individual transition dipoles of donors and acceptors undergoing rotational diffusion during the process of measurement, and (b) mixing of signals between adjacent tetramers (or possibly between tetramers and free monomers) due to image-blurring effects caused by the point spread function of the instrument. Numerical simulations suggest that the second effect should be stronger for higher concentrations of molecules (25). Both of these effects add significant blur to individual histograms, which is cleared away by the method based on generation of meta-histograms introduced in this paper. This allowed us to clearly resolve the fine structure of the E_{app} histograms – as if we were using an imaging method with super-resolution – and thus determine the structure of the Wzm and Wzt oligomers.

6.3.2 Proposed structural model for the ABC transporter

The FRET analysis described above indicates that the cytoplasmic Wzt protein forms a rhombus-shaped tetramer in the absence of the transmembrane domain Wzm, but changes its shape into a square-shaped tetramer in the presence of Wzm. By contrast, Wzm forms a square-shaped tetramer whether Wzt is present or not. In addition, we have demonstrated that the Wzm and Wzt oligomers interact with one another to form a hetero-oligomer. Based on these results, we are now ready to formulate a model for the supramolecular assembly of the *Pseudomonas aeruginosa* ABC transporter for polysaccharides, which consists of one Wzm homo-tetramer on top of one Wzt homo-tetramer, creating a hetero-dimer of homo-tetramers, or a hetero-octamer. Some ambiguity remains with regard to whether each protomer in the Wzm tetramer interacts with a single protomer in the Wzt tetramer and thus forms a head-to-head structure, or a Wzm protomer interacts with two adjacent Wzt protomers thereby forming an interlaced structure (Fig. 6.9). The two configurations differ from each other through a 45° rotation of the Wzt and Wzm tetramers relative to each other and around a common axis perpendicular to the membrane. Further biochemical work will be necessary to determine the specific interactions sites that would be needed in order to choose one configuration over the other.

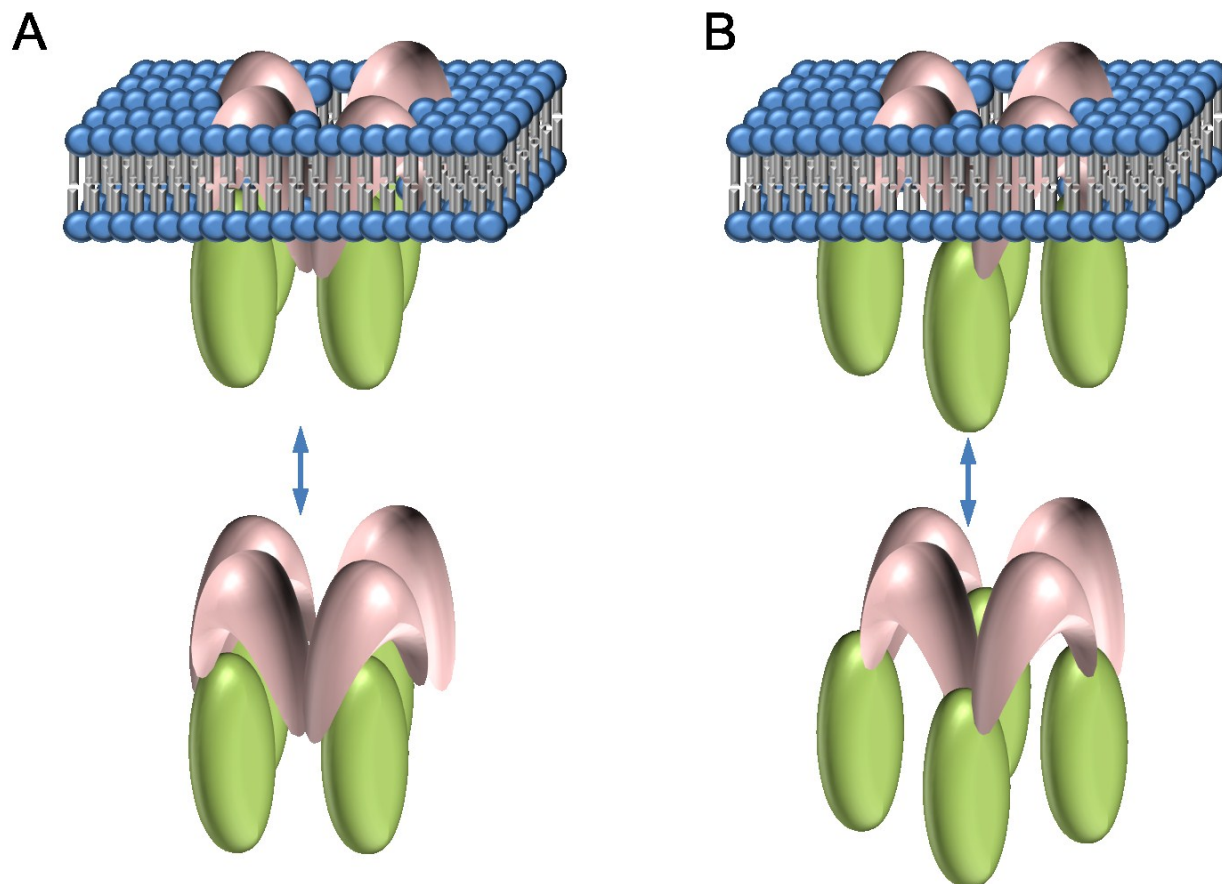


Figure 6.9: Two versions of the hetero-octameric model proposed for the quaternary structure of the Wzm-Wzt ABC transporter. A. Four units of Wzm interacting with four units of Wzt face-to-face. B. Four units of Wzm are interlaced with four units of Wzt.

6.3.3 Considerations regarding the stability of the complexes

Additional information regarding this octamer may be gleaned from the observation that, while most of the cells presented single-peaked E_{app} histograms, a small fraction presented multiple peaks. In other words, while for most cells, the proportion of donors and acceptors was on average the same in each homo-tetramer (of Wzm or Wzt), for some cells all three (for square tetramer) or five (for rhombus tetramers) peaks were

present. This difference in composition suggests that the observed structures are dynamic and that the individual monomers may associate or dissociate reversibly. The fact that the histograms of some cells presented all the peaks suggests that the association/dissociation process is slow and those cells had not expressed the protein tetramers for a length of time sufficient to allow full randomization of their composition.

6.3.4 Comparison of the present results to other studies

The discovery that Wzm and Wzt form interacting tetramers is not an unusual finding in the study of ABC transporters. Indeed, several ABC transporters have been reported to associate into either dimers or multimers. For example, the human multidrug resistant half transporter MRP1 (34), human cystic fibrosis transmembrane conductance regulator (CFTR) (35) and the yeast Pdr5p full transporter (36) have been reported to form dimers. Recently, the multidrug resistant half-transporter human breast cancer protein, ABCG2, was purified as a tetramer (37). Similarly, human ABCA1 transporter exists in intact fibroblasts as a homo-tetramer or even higher oligomerization states (38). Finally, the bi-component ABC transporter protein BtuCD involved in vitamin B₁₂ uptake in *E. coli* – consisting of the homo-dimeric transmembrane protein BtuC and a homo-dimeric nucleotide-binding protein, BtuD – appears to form a hetero-tetramer (39) and serves as a paradigm for all other bacterial ABC transporters. All these studies were done *in vitro* and most of them were limited to the determination of the size of oligomers. Unlike those approaches, the spectrally-resolved FRET used in this study allowed us to determine the stoichiometry of a bi-component bacterial ABC transporter in living cells. We determined the oligomer size of each component as well as their quaternary structure *in vivo* and,

based on these observations, proposed a quaternary structure model which is different from the model proposed for the transporter BtuCD in *E. coli*.

6.3.5 Significance of the present results

At this point, the question that remains is how would tetramerization of Wzt or Wzm be relevant to substrate or even its translocation? Unlike the ABC transporters mentioned in the previous paragraph, which mostly translocate drugs or ions, the ABC transporter formed by Wzm and Wzt translocates a relatively large substrate, the A-band PS. The A-band PS sugar chain is a homopolymer of D-Rhamnose of approximately 70 monomers (40), giving it the length of ~28 nm, assuming an extended form of the polymer with a 0.4 nm per monomer. In fact, recent atomic force microscopy (AFM) studies have shown that the A-band PS can be up to ~36 nm long (41). In light of this, higher order oligomerization of Wzm and Wzt might be required for the translocation of the PS substrate. The Wzt tetramer could provide multiple binding sites for the long or bulky PS substrate. In analogy, the biochemical studies on the homo-tetrameric human ABCA1 led to the proposal that multiple binding sites exist for its substrates (38). Wzm is supposed to form a channel to facilitate the passage of PS across the membrane. It is conceivable therefore that Wzm being a tetramer can form an accommodating channel for the translocation of the bulky PS, a scenario originally proposed by Cuthbertson et al (11). Also, the fact that the Wzt protein tetramer changes its shape upon binding to Wzm may suggest that these structural changes allow for PS or PS-Wzt orientation prior to the translocation event. One of the next steps in these studies would be to determine the binding interfaces for Wzt as well as the side chains of the Wzm that face the channel. This could be done by attempting to orient the Wzm and Wzt subunits within the general

quaternary structure and under the constraints of the relative distances between protomers set by the present study. This step would require knowledge of the tertiary structure, which could be achieved using X-ray crystallographic measurements, which are currently unavailable.

Since we described the structure of the Wzm-Wzt ABC transporter in the absence of its substrate, future studies could attempt to determine whether the presence of polysaccharide causes any changes in the structure of the ABC transporter. An understanding of such changes will provide further information for developing antibiotics targeting the biosynthesis of the A-band LPS endotoxin, a primary factor in *Pseudomonas aeruginosa* pathogenesis.

References

1. Oldham, M. L., Davidson, A. L., and Chen, J. (2008) Structural insights into ABC transporter mechanism. *Curr. Opin. Struct. Biol.* **18**:726-733.
2. Rees, D. C., Johnson, E., and Lewinson, O. (2009) ABC transporters: the power to change. *Nat. Rev. Mol. Cell Biol.* **10**:218-227.
3. Seeger, M. A. and van Veen, H. W. (2009) Molecular basis of multidrug transport by ABC transporters. *Biochim. Biophys. Acta.* **1794**:725-737.
4. Vergani, P., Lockless, S. W., Nairn, A. C., and Gadsby, D. C. (2005) CFTR channel opening by ATP-driven tight dimerization of its nucleotide-binding domains. *Nature* **433**:876-880.
5. Rocchetta, H. L., Burrows, L. L., and Lam, J. S. (1999) Genetics of O-antigen biosynthesis in *Pseudomonas aeruginosa*. *Microbiol. Mol. Biol. Rev.* **63**:523-553.
6. Reeves, P. R., *et al.* (1996) Bacterial polysaccharide synthesis and gene nomenclature. *Trends Microbiol.* **4**:495-503.
7. Hug, I. and Feldman, M. F. (2011) Analogies and homologies in lipopolysaccharide and glycoprotein biosynthesis in bacteria. *Glycobiology* **21**:138-151.
8. Abeyrathne, P. D., Daniels, C., Poon, K. K., Matewish, M. J., and Lam, J. S. (2005) Functional characterization of WaaL, a ligase associated with linking O-

- antigen polysaccharide to the core of *Pseudomonas aeruginosa* lipopolysaccharide. *J. Bacteriol.* **187**:3002-3012.
9. Nagao, K., Kimura, Y., Mastuo, M., and Ueda, K. (2010) Lipid outward translocation by ABC proteins. *FEBS Lett.* **584**:2717-2723.
 10. Rocchetta, H. L. and Lam, J. S. (1997) Identification and functional characterization of an ABC transport system involved in polysaccharide export of A-band lipopolysaccharide in *Pseudomonas aeruginosa*. *J. Bacteriol.* **179**:4713-4724.
 11. Cuthbertson, L., Kos, V., and Whitfield, C. (2010) ABC transporters involved in export of cell surface glycoconjugates. *Microbiol. Mol. Biol. Rev.* **74**:341-362.
 12. Cuthbertson, L., Kimber, M. S., and Whitfield, C. (2007) Substrate binding by a bacterial ABC transporter involved in polysaccharide export. *Proc. Natl. Acad. Sci. USA* **104**:19529-19534.
 13. Bodey, G. P., Bolivar, R., Fainstein, V., and Jadeja, L. (1983) Infections caused by *Pseudomonas aeruginosa*. *Rev. Infect. Dis.* **5**:279-313.
 14. Govan, J. R. and Deretic, V. (1996) Microbial pathogenesis in cystic fibrosis: mucoid *Pseudomonas aeruginosa* and *Burkholderia cepacia*. *Microbiol. Rev.* **60**:539-574.
 15. Hoiby, N., Ciofu, O., and Bjarnsholt, T. (2010) *Pseudomonas aeruginosa* biofilms in cystic fibrosis. *Future Microbiol.* **5**:1663-1674.
 16. Hogardt, M. and Heesemann, J. (2010) Adaptation of *Pseudomonas aeruginosa* during persistence in the cystic fibrosis lung. *Int. J. Med. Microbiol.* **300**:557-562.
 17. Raicu, V. (2007) Efficiency of resonance energy transfer in homo-oligomeric complexes of proteins. *J. Biol. Phys.* **33**:109-127.
 18. Raicu, V., *et al.* (2009) Determination of supramolecular structure and spatial distribution of protein complexes in living cells. *Nat. Photonics* **3**:107-113.
 19. Raicu, V. (2010) FRET-based determination of protein complex structure at nanometer length scale in living cells. *Nanoscopy and Multidimensional Optical Fluorescence Microscopy*, ed Diaspro A. (CRC Press, Boca Raton).
 20. Pisterzi, L. F., *et al.* (2010) Oligomeric size of the M₂ muscarinic receptor in live cells as determined by quantitative fluorescence resonance energy transfer. *J. Biol. Chem.* **285**:16723-16738.
 21. Zimmermann, T., Rietdorf, J., Girod, A., Georget, V., and Pepperkok, R. (2002) Spectral imaging and linear un-mixing enables improved FRET efficiency with a novel GFP₂-YFP FRET pair. *FEBS Lett.* **531**:245-249.
 22. Raicu, V., Jansma, D. B., Miller, R. J., and Friesen, J. D. (2005) Protein interaction quantified in vivo by spectrally resolved fluorescence resonance energy transfer. *Biochem. J.* **385**:265-277.
 23. Zacharias, D. A., Violin, J. D., Newton, A. C., and Tsien, R. Y. (2002) Partitioning of lipid-modified monomeric GFPs into membrane microdomains of live cells. *Science* **296**:913-916.
 24. Denk, W., Strickler, J. H., and Webb, W. W. (1990) Two-photon laser scanning fluorescence microscopy. *Science* **248**:73-76.
 25. Singh, D. R. and Raicu, V. (2010) Comparison between whole distribution- and average-based approaches to the determination of fluorescence resonance energy

- transfer efficiency in ensembles of proteins in living cells. *Biophys. J.* **98**:2127-2135.
26. Li, E., Placone, J., Merzlyakov, M., and Hristova, K. (2008) Quantitative measurements of protein interactions in a crowded cellular environment. *Anal. Chem.* **80**:5976-5985.
 27. Zipfel, W. R., Williams, R. M., and Webb, W. W. (2003) Non-linear Magic: Multiphoton Microscopy in the Biosciences. *Nat. Biotechnol.* **21**:1369 - 1377.
 28. Svoboda, K. and Yasuda, R. (2006) Principles of two-photon excitation microscopy and its applications to neuroscience. *Neuron* **50**:823-839.
 29. Tsien, R. Y. (1998) The green fluorescent protein. *Annu. Rev. Biochem.* **67**:509-544.
 30. Selvin, P. R. (2000) The renaissance of fluorescence resonance energy transfer. *Nat. Struct. Biol.* **7**:730-734.
 31. Raicu, V. and Popescu, A. I. (2008) *Integrated Molecular and Cellular Biophysics* (Springer, London, United Kingdom).
 32. Lakowicz, J. R. (2006) *Principles of Fluorescence Spectroscopy* (Springer, New York, NY, USA).
 33. Koushik, S. V., Blank, P. S., and Vogel, S. S. (2009) Anomalous surplus energy transfer observed with multiple FRET acceptors. *Plos One* **4**:e8031.
 34. Rosenberg, M. F., *et al.* (2001) The structure of the multidrug resistance protein 1 (MRP1/ABCC1) - Crystallization and single-particle analysis. *J. Biol. Chem.* **276**:16076-16082.
 35. Zhang, L., *et al.* (2009) Architecture of the cystic fibrosis transmembrane conductance regulator protein and structural changes associated with phosphorylation and nucleotide binding. *J. Struct. Biol.* **167**:242-251.
 36. Ferreira-Pereira, A., *et al.* (2003) Three-dimensional reconstruction of the *Saccharomyces cerevisiae* multidrug resistance protein Pdr5p. *J. Biol. Chem.* **278**:11995-11999.
 37. Dezi, M., *et al.* (2010) The multidrug resistance half-transporter ABCG2 is purified as a tetramer upon selective extraction from membranes. *Biochim. Biophys. Acta.* **1798**:2094-2101.
 38. Denis, M., *et al.* (2004) Characterization of oligomeric human ATP binding cassette transporter A1. Potential implications for determining the structure of nascent high density lipoprotein particles. *J. Biol. Chem.* **279**:41529-41536.
 39. Locher, K. P., Lee, A. T., and Rees, D. C. (2002) The *E. coli* BtuCD structure: a framework for ABC transporter architecture and mechanism. *Science* **296**:1091-1098.
 40. King, J. D., Kocincova, D., Westman, E. L., and Lam, J. S. (2009) Review: Lipopolysaccharide biosynthesis in *Pseudomonas aeruginosa*. *Innate Immun.* **15**:261-312.
 41. Ivanov, I. E., *et al.* (2011) Relating the physical properties of *Pseudomonas aeruginosa* lipopolysaccharides to virulence by atomic force microscopy. *J. Bacteriol.* **193**:1259-1266.

Chapter 7. Conclusion and directions for future research

As described in chapter 6, the cytoplasmic NBD subunit Wzt forms a rhombus-shaped tetramer which changes shape to become a square upon co-expression with transmembrane subunit Wzm. In contrast, the Wzm subunit (located at the membrane) forms a square shaped tetramer and the quaternary structure of this protein remains unchanged upon co-expression with Wzt. Moreover, both subunits interact at the membrane level. Based on these results, we proposed that the Wzm-Wzt transporter forms a heterodimer of homo-tetramers or hetero-octamers that translocates the A-band polysaccharides, synthesized on the cytoplasmic side of inner membrane, across the inner membrane in Gram-negative bacterium, *Pseudomonas aeruginosa*. In addition, the four Wzm units either interact with the four Wzt units head to head or the four units of Wzm are interlaced with the four units of Wzt. At this point, we have no way to give preference to one structure over the other. To exactly predict the quaternary structure, we needed to know the crystal structures of these proteins which are not available at this time.

LPS is found on the outer leaflet of the outer membrane of Gram-negative bacteria. In these bacteria, the polysaccharides are synthesized at the cytoplasmic surface of the inner membrane and then are translocated to the periplasm either through ABC transporters or through other transmembrane proteins. The structure proposed by us for the Wzm-Wzt transporter can be used as a model system for other transporters found in other Gram-negative bacteria that are involved in polysaccharide export.

In our experiments, about 90% of the cells expressing either Wzt or Wzm proteins showed single peaks in their E_{app} histogram and 10% of the cells showed multiple and/or broad peaks. We believe that the presence of single peaks in the histograms of cells that express such comparatively large oligomers is due to the dynamic nature of the oligomeric complexes formed by the Wzm and Wzt proteins, which allows for a rapid mixing of the donors and acceptors within complexes, which results in complexes with essentially same ratio of donors and acceptors throughout the cell. This is an ad-hoc assumption and needs to be tested in the future.

In addition, we determined the quaternary structure of these bacterial proteins in CHO cells in the absence of polysaccharides and ATP. Future studies needed to show how the presence of either ATP or polysaccharide or both affect the quaternary structure of each subunit and, hence, the transporter. For that, polysaccharides only, ATP only or both should be injected in the CHO cells co-expressing GFP₂-tagged Wzm (Wzt) and YFP-tagged Wzm (Wzt) and should be imaged to obtain meta-histograms of FRET efficiencies. The meta-histograms thus obtained in all the above mentioned situations should be tested against appropriate theoretical models to observe the structural changes, if any. Ideally, microfluidics devices in conjunction with FRET imaging should be used to observe these effects.

These biophysical studies combined with biochemical studies and with determination of crystal structure should help elucidate the specific mechanisms leading to translocation of polysaccharide across the inner membrane via this ABC transporter.

When the polysaccharides reach the periplasmic surface of the inner membrane the O antigen of PSs are ligated to the core lipids through a process that is mediated by the WaaL O antigen ligase, an integral membrane protein (1) to form LPSs. Several biochemical studies have been done on this part (1-3). However, the mechanism of LPS transport from inner membrane to the outer leaflet of the outer surface is not known (4). We believe the determination of structure of the A-band transporter is a big step towards developing antibiotics targeting the biosynthesis of A-band LPS, an endotoxin in *Pseudomonas aeruginosa*.

References

1. Abeyrathne, P. D., Daniels, C., Poon, K. K., Matewish, M. J., and Lam, J. S. (2005) Functional characterization of WaaL, a ligase associated with linking O-antigen polysaccharide to the core of *Pseudomonas aeruginosa* lipopolysaccharide. *J. Bacteriol.* **187**:3002-3012.
2. Abeyrathne, P. D. and Lam, J. S. (2007) WaaL of *Pseudomonas aeruginosa* utilizes ATP in in vitro ligation of O antigen onto lipid A-core. *Molecular Microbiology* **65**:1345-1359.
3. Burrows, L. L., Chow, D., and Lam, J. S. (1997) *Pseudomonas aeruginosa* B-band O-antigen chain length is modulated by Wzz (Ro1). *J. Bacteriol.* **179**:1482-1489.
4. Tefsen, B., Geurtsen, J., Beckers, F., Tommassen, J., and de Cock, H. (2005) Lipopolysaccharide transport to the bacterial outer membrane in spheroplasts. *J. Biol. Chem.* **280**:4504-4509.

Curriculum vitae

Deo Raj Singh

Place of birth -- Allahabad, Uttar Pradesh (India)

Education

PhD: University of Wisconsin-Milwaukee
(Milwaukee, WI - USA) December 2012

Dissertation Title: Investigation of the Quaternary Structure of an ABC Transporter in Living Cells Using Spectrally Resolved Resonance Energy Transfer

MSc: Jawaharlal Nehru University (New Delhi, India) May 1999

Major: Physics

BSc: Ewing Christian College (Allahabad, India) September 1997

Major: Physics and Mathematics

Academic Awards / Achievements

- Distinguished Dissertation Fellowship -- (Graduate School; Univ. of Wisconsin-Milwaukee) AY 2011-2012
- Distinguished Graduate Student Fellowship -- (Graduate School; Univ. of Wisconsin-Milwaukee) AY 2010-2011
- David Lichtman Memorial Scholarship -- (Physics Dept.; Univ. of Wisconsin-Milwaukee) Fall 2012
- David Lichtman Scholarship *for outstanding performance in experimental physics* -- (Physics Dept.; Univ. of Wisconsin-Milwaukee) May 2011
- Graduate Student Travel Award -- (Univ. of Wisconsin-Milwaukee) Multiple awards during 2010 - 2012
- Chancellor's Graduate Student Award (Physics Dept.; Univ. of Wisconsin-Milwaukee) Multiple awards during 2007 – 2011

- Graduate Aptitude Test of Engineers (GATE) – (Ministry of Human Resource Development, Government of India) 2005
- Council of Science and Industrial Research- Junior Research Fellowship (CSIR-JRF) – (Government of India) 1999
- Gold medal – (Ewing College; Allahabad, India) 1997

Publications

1. Deo R. Singh, Mohammad M. Mohammad, Suparna Patowary, Julie A. Oliver, Liviu Movileane, and Valerică Raicu, “Determination of the quaternary structure of a bacterial ATP-binding cassette (ABC) transporter in living cells.” *Integrative Biology* (available on-line as of December 2012).
2. Michael R. Stoneman, Suparna Patowary, Deo R. Singh, Liudmila Komarov, Linda G. Westrick, Julie A. Oliver, Valerică Raicu. “Quantifying the efficiency of various FRET constructs using OptiMiS.” *BioTechniques*, **52** (2012), 191-195.
3. Michael R. Stoneman, S. Patowary, M. T. Roesch, D. R. Singh, V. Strogolov, J. A. Oliver, V. Raicu, “Determination of the stoichiometry, structure, and distribution in living cells of protein complexes from analysis of single-molecular-complexes FRET.” In: A. Periasamy, K. König and P.T.C. So (Eds.), *Multiphoton Microscopy in the Biomedical Sciences XI*. Proceedings of SPIE, **7903** (2011), 790324.
4. Michael R. Stoneman, Deo R. Singh, and Valerică Raicu, “In vivo quantification of G protein coupled receptor interactions using spectrally resolved two-photon microscopy” *Journal of Visualized Experiments*, **47** (2011).
5. M.R. Stoneman, D.R. Singh, and V. Raicu. “In vivo stoichiometry monitoring of G protein coupled receptor oligomers using spectrally resolved two-photon microscopy.” In: A. Periasamy, P.T.C. So and K. König (Eds.), *Multiphoton Microscopy in the Biomedical Sciences X*. Proceedings of SPIE, **7569** (2010), 756913-1 – 756913-8.
6. Deo R. Singh and Valerică Raicu. “Comparison between whole-distribution- and average-based approaches to the determination of FRET efficiency in ensembles of proteins in living cells.” *Biophysical Journal*, **98** (2010), 2127-2135.

Presentations

1. Mohammad M. Mohammad, Deo R. Singh, Julie A. Oliver, Liviu Movileanu, and Valerică Raicu, “FRET-based method to decipher the stoichiometry and structural assembly of bacterial ABC transporter involved in exporting endotoxins” **Poster** to be presented by Mohammad M. Mohammad, Annual Meeting of the American Society for Cell Biology, San Francisco, CA (upcoming in late December 2012)

2. Deo R. Singh, Mohammad M. Mohammad, Julie A. Oliver, Liviu Movileanu, and Valerică Raicu, "Quaternary structure of a bacterial ABC transporter *in vivo* using spectrally resolved FRET" **Invited Talk**, *National Institute of Health*, Bethesda, MD, August 2012.
3. Deo R. Singh, Ashish K. Mishra, Tae Gyun Kim, Julie A. Oliver, Paul S. Park, and Valerică Raicu, "Quaternary structure of wild type and mutated rhodopsin at room and body temperature using spectral FRET" **Oral Presentation**, OWLS, Genoa, Italy, July 2012.
4. Ashish K. Mishra, Deo R. Singh, Tae Gyun Kim, Julie A. Oliver, Paul S. Park, and Valerică Raicu, "Investigation of rhodopsin oligomerization at room and body temperature using spectral FRET" **Poster** presented by Ashish K. Mishra, FASEB, Colorado, CO, June 2012.
5. Deo R. Singh, Mohammad M. Mohammad, Khalil Raja Howard, Julie A. Oliver, Liviu Movileanu, and Valerică Raicu, "Quaternary structure of the NBD subunit Wzt of a bacterial ABC transporter in the absence and presence of TMD subunit Wzm using pixel-level FRET" **Poster**, *Biophysical Society Annual Meeting*, San Diego, CA, February 2012.
6. Deo R. Singh, Mohammad M. Mohammad, Khalil Raja Howard, Julie A. Oliver, Liviu Movileanu, and Valerică Raicu, "Quaternary structure determination of a bi-component bacterial ABC transporter using spectral FRET" **Oral presentation**, *NSF-UWM Workshop: Open Forum for Innovation in Two-Photon Microspectroscopy*, Milwaukee, WI, November 2011.
7. Mohammad Mohammad, Deo Raj Singh, Khalil Raja Howard, Arron Sullivan, Julie A. Oliver, Valerică Raicu, and Liviu Movileanu, "Deciphering the subunit stoichiometry and structural assembly of bacterial ABC transporter" **Oral presentation** delivered by Mohammad M. Mohammad, *Biophysical Society Annual Meeting*, Baltimore, MA, March 2011.
8. Deo Raj Singh, Mohammad M. Mohammad, Khalil Raja Howard, Julie A. Oliver, Liviu Movileanu, and Valerică Raicu, "Localization, interaction and stoichiometry of the Wzm and Wzt subunits of a bacterial ABC transporter using spectrally resolved FRET, **Poster**, *FRET at 65: A celebration of Foster one day symposium*, Charlottesville, Virginia, VA, March 2010.
9. M. R. Stoneman, D. R. Singh, and V. Raicu, "In vivo stoichiometry monitoring of G protein coupled receptor oligomers using spectrally resolved two-photon microscopy." **Oral presentation** delivered by M. R. Stoneman, *Photonics West (Bios)*, San Francisco, CA, January 2010.
10. D. R. Singh, K. Michalski, and V. Raicu, Information extraction from simulations-based data fitting of distributions of FRET efficiencies from donors and acceptors in the cytoplasm of living cells, **Poster**, *Biophysical Society Annual Meeting*, San Francisco, CA, February 2010.

Research Experience

- **Research Assistant** -- Lab of Valerică Raicu, within the Dept. of Physics, University of Wisconsin – Milwaukee (Milwaukee, WI USA) Summer 2008 - Fall 2012
- **Project**, with Prof. Deepak Kumar, School of Physical Sciences, Jawaharlal Nehru University (New Delhi, India) Winter 1999

Teaching Experience

- **Teaching Assistant:** Department of Physics, University of Wisconsin – Milwaukee (Milwaukee, WI USA) Fall 2007; Spring 2008; Fall 2010
- **Lecturer:** Department of Physics, Brahmanand College, CSJM University, Kanpur (Uttar Pradesh, India) 2001 - 2006